RCA Review

A technical journal published quarterly by RCA Research and Engineering in cooperation with the subsidiaries and divisions of RCA.

Contents

December 1978 Volume 39 Number 4 ISSN 0033-6831

Yield-Area Analysis: Part II—Effects of Photomask Alignment Errors on Zero Yield Loci

C. S. Kim and W. E. Ham

RCA Laboratories, Princeton, N.J. 08540

Abstract—A relatively detailed analysis is made of the effects of mask alignment error on the resulting yield pattern of LSI circuits. It is clearly shown that alignment errors produce certain characteristic types of yield distribution. The sum of all of the common alignment errors—translational, theta, thermal and runout—can be combined to produce fatal errors even though the individual errors are within specification. Excellent agreement was found between actual production circuit yield distributions and the results of the combined analysis.

1. Introduction

This paper is the second part of a multipart series concerning the spatial distribution of yield of LSI circuits across wafers. Part I of this series[1] dealt with the basic causes of incomplete usage of the wafer area for yield and showed how zero-yield loci can be drawn that divide the wafer into regions where good circuits are and are not found. As discussed in that paper, one of the more common causes of a nonunity Area Usage Factor (AUF) is the imperfect alignment of photomask to images already on the wafer. It is the intent of this paper to describe the types of zero yield loci that result from these alignment errors, so that one can recognize potential alignment problems from the shape and location of the zero yield loci. Since photomask alignment errors are usually quasicontinuous they satisfy the definition for a parameter given in Part I.

Some analytical discussion concerning photomask registration or alignment errors has appeared in the literature recently.[2–5] The discussion in this paper is aimed specifically at the zero yield loci resulting

from alignment errors. The registration accuracy can be handled with some analytical elegance in the general case, but the results obtained apply to yield loci only if the registration errors are the limiting parametric features. The results to be discussed here can help to determine if a particular type of alignment error might be causing the zero yield loci.

The possible alignment errors are divided into two major categories, namely, operator-induced errors and errors resulting from size incompatibility. Simple translational and rotational errors fall into the category of operator-induced error, whereas run-out, thermal mismatch, and dimensional instability problems fall into the category of size incompatability. An analytical model for alignment error is derived that takes into account the sum of all these error components.

The constant-alignment-error loci obtained from this model show how alignment errors can produce AUF's less than unity. The contribution from the choice of alignment keys and varying operator sensitivity to the alignment error is briefly discussed.

As part of the final discussion, a sample case is reviewed where all the individual error components are within the limits of reasonable specification, but the resulting error from the sum of all these components has a magnitude easily large enough to cause a low AUF.

2. Photomask Alignment Error Analysis

Typically, the two different levels of images are aligned using two locations viewed simultaneously through a split view microscope. The midpoint of the line connecting the two spots usually lies close to the center of a wafer and therefore, to the center of the mounting chuck. In other words, one usually mounts a wafer concentric to the round mounting chuck and the two alignment spots are chosen at equal distance from the center of the wafer, even though such conditions are not absolutely necessary for proper alignment.

In the following discussion, the origin of the coordinate system is chosen to be the midpoint of the line connecting the two alignment spots as shown in Fig. 1. The choice is for convenience and is irrelevant to the accuracy of the model.

2.1 Simple Alignment Error

This type of misalignment can be divided into two categories, translational and rotational, for which we can write, respectively,

$$\bar{\Delta}_{\text{Trans}} = C_x\hat{x} + C_y\hat{y} \qquad [1]$$

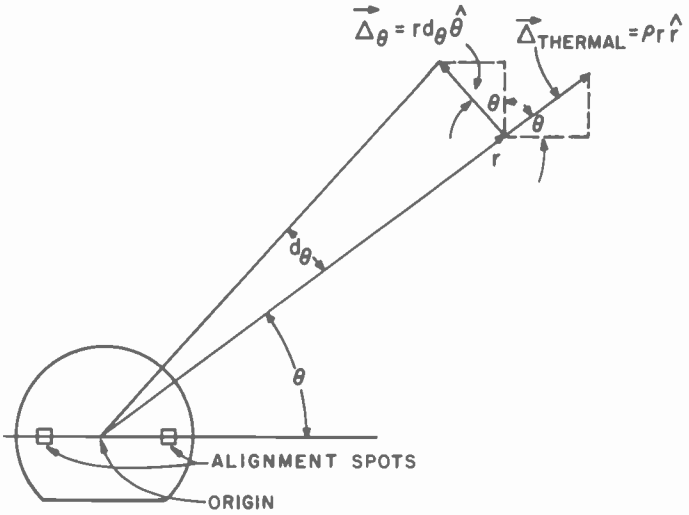

Fig. 1—Definition of the error components due to theta and thermal errors and definition of coordinate origin.

$$\begin{aligned}\overline{\Delta}_{rot} &= rd_\theta\hat{\theta} = rd_\theta(-\sin\theta\hat{x} + \cos\theta\hat{y}) \\ &= yd_\theta\hat{x} + xd_\theta\hat{y}, \end{aligned} \quad [2]$$

where C_x, C_y are the x and y components of translational error, d_θ is the rotational error in radians, and $\hat{x}$, $\hat{y}$, $\hat{r}$, $\hat{\theta}$ are the unit vectors.

A direct translational misalignment alone would generally cause loss of the entire wafer, not just a partial area of the wafer. On the other hand, a pure rotational mismatch between the mask and the wafer around the wafer center would cause loss of the outer portion of the wafer. When the rotational error alone is considered, only the point on the wafer intersecting the rotational axis would have exact alignment.

2.2 Size Incompatability

The other type of misalignment that may cause local areas of zero yield is nonidentical sizes of masks and images previously printed on wafers. This can be caused by many different phenomena, such as nonreproducible step and repeat distances between masks, different temperatures of the mask between the first and second exposures, changes in the wafer size between exposures, changes in the wafer temperature due to different optical absorption properties during exposure, and changes in the pressure applied during exposure to warped wafers due to a change in the warpage.

The alignment errors caused by the size incompatibility can generally be divided into two categories. One we shall call generically "runout." The second category is expansion. In common usage the runout refers to the irregularities in the step-and-repeat distances. These irregularities may arise from step-and-repeat machine movement errors, roundoff errors in digitizing the images, or thermal instability during the mask fabrication. In the general case, runout errors between two levels can have a nonlinear dependence on positions. For example the roundoff errors introduced by digitization would result in errors that are a periodic function of position. A recent investigation by Ham[6,8] and others[3,4] shows that the runout can be a highly nonmonotonic function of position. However, for reasons of simplicity the runout is assumed to be a simple linear function of position as given by:

$$\vec{\Delta}_{\text{runout}} = \beta_x x\hat{x} + \beta_y y\hat{y}. \qquad [3]$$

Expansion because of temperature differences between the mask and wafer or from temperature or dimensional changes occurring between the time of first level printing and second level printing would also result in a monotonic runout type of error. The distance of an arbitrary point on a wafer or mask from the origin will vary with temperature according to the linear equations;

$$r_m = r_{m_o}(1 + \alpha_m \Delta T_m) \text{ for the mask} \qquad [4]$$

$$r_w = r_{w_o}(1 + \alpha_w \Delta T_w) \text{ for the wafer} \qquad [5]$$

The α's are the linear expansion coefficients, r_{m_o} and r_{w_o} are the original radii at a reference temperature, T_{ref}, and ΔT_m and ΔT_w are the differences between T_{ref} and the mask and wafer temperature, respectively. If we assume an isothermal mask and an isothermal wafer (not necessarily the same temperature) at the first exposure and that the temperature of each at this time is its reference temperature, then ΔT_m and $\Delta T_w = 0$, and r_{m_1} and $\bar{r}_{w_1} = r_o$. This radius is arbitrary. At the second exposure at a nominal distance of r_o from the reference point (the point of exact match for that alignment) a change of $\Delta r = r_{m_2} - r_{w_2}$ will be given by;

$$\frac{\Delta r}{r_o} = \alpha_m \Delta T_m - \alpha_w \Delta T_w, \text{ if } r_{m_2} - r_{w_2} \ll r_o, \qquad [6]$$

as is usually the case. Notice that if $\Delta T_{m_2} = \Delta T_{w_2}$, then the difference in the thermal expansion coefficients between the mask and the wafers alone control the error.

The thermal expansion problem is most serious when the mask temperature and the wafer temperature vary in the opposite directions. When the mask temperature and the wafer temperature are equalized,

the errors due to ambient temperature fluctuations can be minimized by matching the expansion coefficients of the mask to that of the substrate.

Fig. 2 shows the expected thermal error for several different types of materials commonly used for masks and substrates as a function of temperature difference. It is apparent that severe yield loss *could* be occurring for practically attainable temperature differences. However it would require approximately 8°C change in ambient temperature to cause the sapphire soda-lime system to fail 1.25-μm criteria for a 7.6-cm wafer, *provided* the mask and the wafers were both at the same temperature. An ambient temperature change of this magnitude would rarely be experienced in practice. Nonetheless thermal errors add to those present from other sources and can be the critical difference between success and failure.

The error arising from the size incompatibility is similar to the rotational error in that it is proportional to the distance from the origin, but the two error vectors are orthogonal to each other. The error component caused by the thermal mismatch can be written

$$\vec{\Delta}_{\text{thermal}} = \rho r\hat{r} = \rho(r\cos\theta\hat{x} + r\sin\theta\hat{y}) = \rho x\hat{x} + \rho y\hat{y} \qquad [7]$$

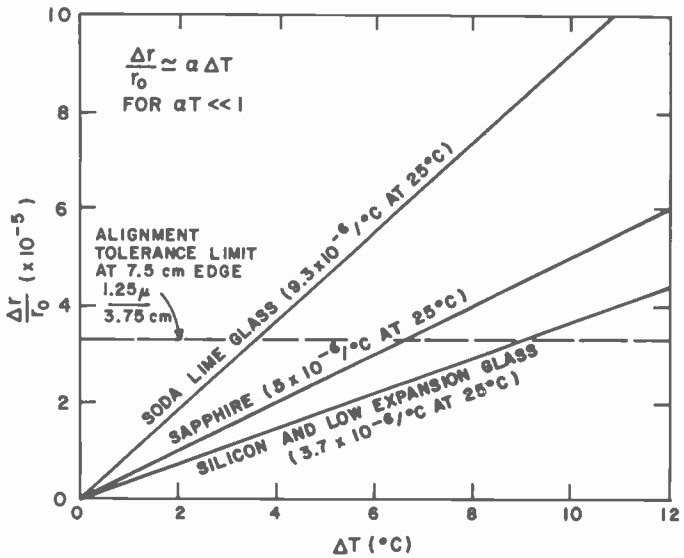

Fig. 2—Linear expansion with temperature for some materials commonly used for masks and substrates.

where $\rho = \Delta r/r_o$ is a thermal mismatch parameter as defined in Eq. [6].

2.3 Equal Error Contour (Loci)

The total alignment error is the vector sum of the four error components described by Eqs. [1], [2], [3], and [7].

$$\begin{aligned} |\Delta|^2 &= |\Delta_x|^2 + |\Delta_y|^2 \\ &= [C_x + (\beta_x + \rho)x - d_\theta y]^2 + [C_y + (\beta_y + \rho)y + d_\theta x]^2. \end{aligned} \quad [8]$$

From Eq. [8] it is clear that in a realistic situation, a unique point (x_o,y_o) always exists where both of the bracketed terms disappear. At this point the total error is zero. In other words, there exists a point where the two levels match exactly. We call this point the Point of Exact Match (PEM). The coordinates of PEM can be obtained by solving the following equations for x and y:

$$\begin{aligned} C_x + (\rho + \beta_x)x - d_\theta y &= 0 \\ C_y + (\rho + \beta_y)y + d_\theta x &= 0, \end{aligned} \quad [9]$$

from which one obtains,

$$x_o = -\frac{(\rho + \beta_y)C_x + C_y d_\theta}{(\rho + \beta_x)(\rho + \beta_y)d_\theta^2} \quad [10]$$

$$y_o = \frac{-(\rho + \beta_x)C_y + C_x d_\theta}{(\rho + \beta_x)(\rho + \beta_y) + d_\theta^2}. \quad [11]$$

When translational errors are absent (in other words, $C_x = C_y = 0$), the PEM lies at the origin of our coordinate system. The origin was assumed to coincide with the midpoint of the line connecting the two alignment spots. If all the alignment errors, other than the translational error, were ideally compromised during the alignment process, then the total error at the midpoint will indeed be zero.

In general, if the thermal, rotational, and runout terms are small compared to the translational term, one must move a considerable distance from the origin to find the PEM. In fact, the PEM may lie outside the wafer, which simply means its distance from the origin must be quite large in order to "make up" the translation error. On the other hand when the translation errors are small, appreciable alignment errors will only occur at a considerable distance from the PEM.

Rearranging Eq. [8] we get,

$$\begin{aligned} |\Delta| &= C_x^2 + C_y^2 + x^2[(\beta_x + \rho)^2 + d_\theta^2] \\ &+ x[2C_x(\beta_x + \rho) + 2C_y d_\theta] \\ &+ y^2[(\beta_y + \rho)^2 + d_\theta^2] + y[2C_y(\beta_y + \rho) + 2C_x d_\theta] \\ &+ xy[2d_\theta(\beta_y - \beta_x)] \\ &= ax^2 + bxy + cy^2 + dx + ey + f \end{aligned} \quad [12]$$

The xy cross product term can be eliminated by performing a rotational transformation of the coordinate by an angle ϕ which is given by the following expression (the detailed algebra can be found in Ref. [7]):

$$\phi = \frac{1}{2}\tan^{-1}\left[\frac{-2d_\theta}{\beta_x + \beta_y + 2\rho}\right] \quad [13]$$

When $\beta_x = \beta_y$, ϕ always equals zero even though it may not be obvious from Eq. [13].

The new X-Y coordinate obtained by rotating the x-y coordinate by ϕ given in Eq. [13] enables one to rewrite Eq. [12] as

$$A(X - X_o)^2 + C(Y - Y_o)^2 = |\Delta|^2, \quad [14]$$

where,

$$A = a\cos\phi^2 + b\sin\phi\cos\phi + c\sin\phi^2$$

$$C = a\sin\phi^2 - b\sin\phi\cos\phi + c\cos\phi^2$$

and, (X_o, Y_o) is the PEM (x_o, y_o) expressed in the new X-Y coordinates. Eq. [14] defines the loci of constant error. In general, it is an ellipse with coordinate axis rotated by ϕ and translated by (X_o, Y_o) from the original coordinate origin at the center of the wafer. Eq. [14] will also describe the boundary between yielding and nonyielding areas if the value of $|\Delta|$ would cause a particular circuit to exceed its defined parametric limits or to cease operation.

3. Discussion

3.1 Specific Case Study

Let us consider a specific example where realistic numbers are used to determine the constant error loci. We will assume the following conditions which apply to a typical manufacturing operation. The alignment keys are located 5 cm apart and have 2.5 μm clearance between two levels, as shown in Fig. 3. After the image is printed, a 0.825 μm shift in the alignment, as shown in the same figure, is assumed to be an acceptable error. Furthermore the mask and wafer are assumed to be at equal temperatures at the time of exposure, but the ambient temperatures has changed by +1°C from the previous exposure. The mask material is taken as low expansion glass and the wafer is sapphire. The mask runout is 1.25 μm over 7.5 cm distance.

With the above assumptions the following parameters can be derived:

$$d_\theta = 0.825\ \mu\text{m}/5\ \text{cm} = 1.65 \times 10^{-5}\ \text{rad}$$

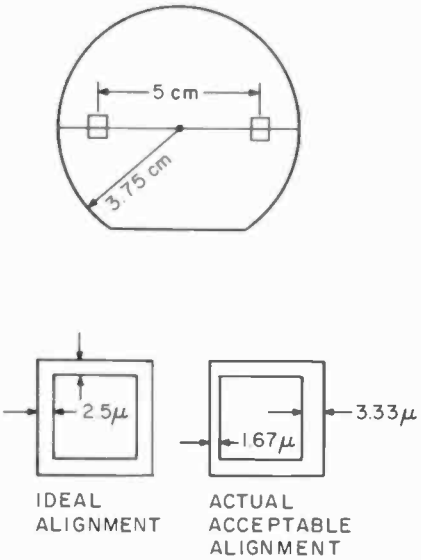

Fig. 3—Conditions used in specific case study.

$$\rho = (3.7 \times 10^{-6}/°C - 5 \times 10^{-6}/°C) \times 1°C = -1.4 \times 10^{-6}$$

$$\beta_x = \beta_y = 1.25\ \mu m/7.5\ cm = 1.67 \times 10^{-5}$$

$$C_x = C_y = 0.825\ \mu m$$

Since $\beta_x = \beta_y$, it is not necessary to rotate the axis, and $\phi = 0$. From Eq. [12] we have,

$$a = c = 5.06 \times 10^{-10},$$

and from Eqs. [10] and [11] we have,

$$x_o = -5.18\ cm$$

$$y_o = -0.195\ cm.$$

Since $A = C$ in Eq. [14], the locus is a circle centered at (x_o, y_o) whose radius depends on the error criteria $|\Delta|$. Fig. 4 shows the resulting loci for the different values of $|\Delta|$, 1.23 μm, 1.875 μm, and 2.5 μm. If a circuit is designed with 1.25-μm alignment tolerance in mind, it is perfectly clear that major portions of the wafer will not yield operating circuits. Thus the AUF will be considerably smaller than unity. In this specific case, the circuit design rules must allow for an alignment tolerance of 2.5 μm in order for the entire area of the wafer to be utilized. Excellent agreement with these results was found under actual conditions. Fig. 3 of Part 1[1] shows results from wafers processed under the conditions assumed above.

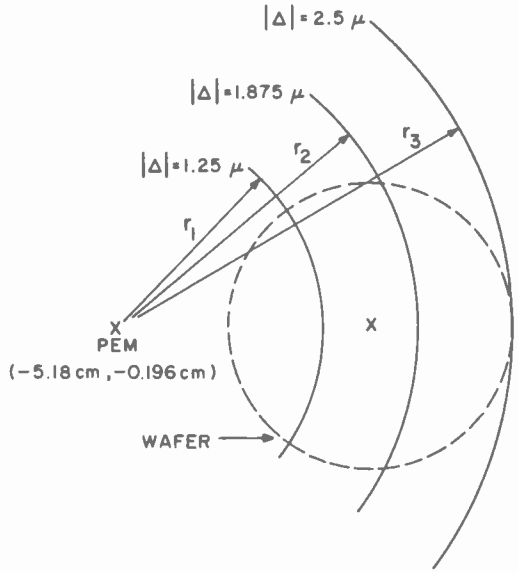

Fig. 4—The constant-alignment-error loci discussed in the specific case study.

3.2 General Discussion

Once the quality of alignment machine and the associated process is fixed, the operator skill, positioning of alignment keys, and alignment key design itself are the only causes of rotational and translational error left for improvement. Frequently, alignment keys are not optimally designed for human use. The clearance in alignment key is typically limited to 2.5 μm by the optics used. This will actually provide a practical window of perhaps a third of the clearance, i.e., 0.8 μm.

With the built-in alignment error possible from the keys, ϵ, it is easy to see that the spacing between the alignment spots on the wafer surface has a first-order effect on the rotational error actually obtained. Assuming the imperfect alignment key alone resulted in a rotational error, the error, d_θ, can be written as $2\epsilon/S$, where S is the spacing of the alignment spots. When we consider this rotational error and thermal mismatch only, the resulting constant error loci will be concentric circles with their PEM located at the center of the wafer. With ϵ known, and assuming that mask and wafer are at equal temperature but that the ambient temperature changes by ΔT, the radius around the PEM for the constant error loci becomes

$$r = \frac{|\Delta|}{\sqrt{(\alpha_m - \alpha_w)^2 \Delta T^2 + \left(\frac{2\epsilon}{S}\right)^2}}. \qquad [15]$$

This function is plotted in Fig. 5 for the specific case of $|\Delta| = 1.25\ \mu m$. We also note the relatively obvious result that with less rotational error due to wider separation of alignment spots, a wider temperature difference is tolerable. Also, the use of masks matched in thermal expansion to the wafers can nearly eliminate the thermal problems.

So far only the interaction between two levels has been considered. When more than two levels are involved, one can readily deduce that, to a first order approximation, the yielding area will have a convex contour resulting from superimposed ellipses. For example, when three alignments are involved, the yielding area might have the shape shown in Fig. 6. In this case, only the area common to all three will give nonzero yield.

It is important to note that the analysis carried out so far has assumed that only the total vector sum of the error matters, not the individual x or y components. If the entire circuit is laid out with orthogonal lines only, then the individual x and y components of the alignment errors will determine the constant error loci. One can deduce from Eq. [8] that such loci will be, in general, a set of parallelograms centered at (x_o,y_o).

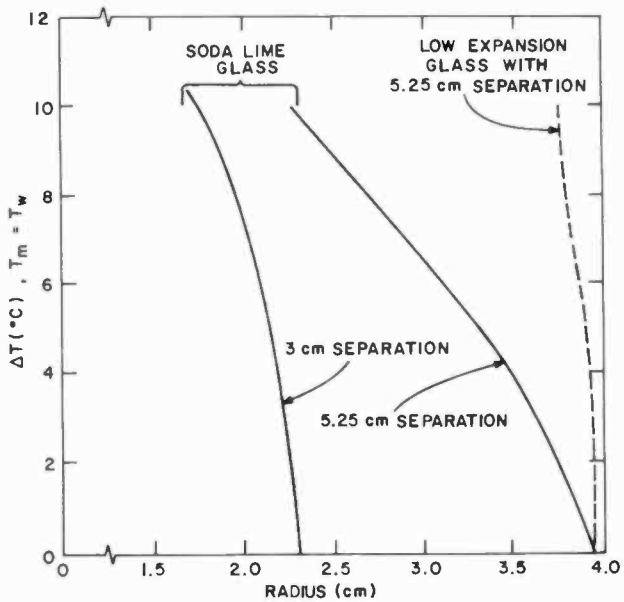

Fig. 5—Plot of Eq. [15] for different mask materials and separations of alignment spots.

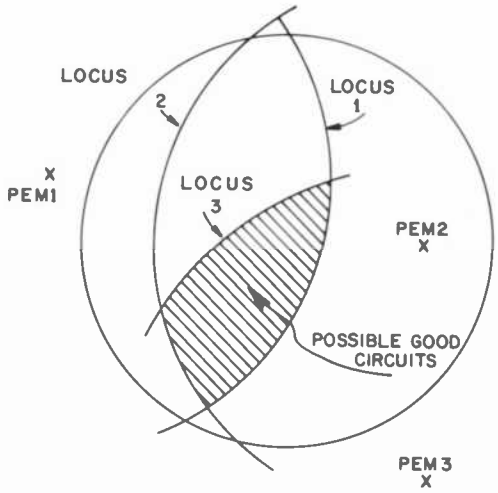

Fig. 6—Zero-yield loci resulting from the superposition of three different alignments.

4. Conclusions

The following conclusions are drawn from the analysis and discussions of alignment errors presented in this paper:

(1) The mathematical analysis presented here proves that the photomask alignment error can result in a poor wafer area usage.

(2) It is quite possible and likely that the various contributions to mask alignment error can add up to a substantial reduction in the area of the wafer used for yield, even though the specifications for the individual errors are satisfied by the circuit design.

(3) For any mask alignment that has some component of rotational, thermal, or monotonic runout error, a point of exact match (PEM) exists. This point may lie well off the wafer.

(4) Mask alignment errors, in general, could cause zero yield loci that have straight or convex edges and that are randomly oriented on the wafer.

(5) Considerable error in alignment may be experienced because of improper temperature control during photoresist exposure.

Acknowledgments

The authors would like to thank N. Turner for directing our interest in this area, and N. Goldsmith for critical reading of the manuscript. We also thank R. Rhodes and R. Van Asselt for supplying some materials data on mask materials.

Note Added in Proof

During the preparation of this manuscript, a paper appeared[9] that also discusses some of the features discussed in this paper. Although some of the results are similar, the present paper is focused on the detection of possible alignment incompat bility from the distribution of circuits while Ref. [9] deals with techniques used to determine the error components. There is no important disagreement between the results of the two papers.

References:

[1] W. E. Ham, "Yield-Area Analysis: Part I—A Diagnostic Tool for Fundamental Integrated Circuit Process Problems," *RCA Review*, **39**, p. 231, June, 1978.

[2] T. Matsutawa, H. Sunami, and N. Hashimoto, "Analysis of Superposition Errors in Wafer Fabrication," *Microelectronics and Reliability*, **16**, p. 173 (1977).

[3] D. H. Leebrick and D. W. Kisken, "An Electrical Alignment Test Device and Its Use in Investigating Processing Parameters," Paper presented at Kodak Microelectronics Seminar, Oct. 6, 7, 1977, Monterey, Ca.

[4] T. J. Russell, R. F. Leedy, and R. L. Mattis, "A Comparison of Electrical and Visual Alignment Test Structures for Evaluating Photomask Alignment in Integrated Circuit Manufacturing," Extended Abstracts, IEDM (Dec. 77), Abstract 2.1, p. 7A.

[5] W. T. Lynch, "The Reduction of LSI Chip Costs by Optimizing the Alignment Yields," Extended Abstracts, IEDM (Dec. 77), Abstract 2.2, p. 7G.

[6] W. E. Ham, "Intrachip and Spatial Parametric Integrity—An Important Part of IC Process Characterization," Extended Abstracts, IEDM (Dec. 1977), Abstract 19.6, p. 406; IEEE Cat. NO 77 CH 1275-7ED.

[7] J. F. Randolf, *Calculus and Analytic Geometry*, pp. 278–282, Wadsworth Publishing Co., Belmont, Calif. (1961).

[8] W. E. Ham, "Test Pattern Design and Analysis for SOS/LSI," Interim Report No. 1, National Bureau of Standards, Contract No. 5-35916 (June 1977).

[9] D. S. Perloff, "A Four-Point Electrical Measurement Technique for Characterizing Mask Superposition Errors on Semiconductor Wafers," *IEEE J. Sol. State Cir.*, **SC-13**, p. 436 (1978).

Near and Far-Field Analytical Approximations for the Fundamental Mode in Symmetric Waveguide DH Lasers*

Dan Botez

RCA Laboratories, Princeton, N.J. 08540

Abstract—Analytical approximations of near- and far-field parameters characterizing the TE_0 mode propagation in symmetric double-heterojunction waveguides are described. By using trigonometric function approximations, the mode phase shift at the dielectric interface is estimated within a few percent over the whole range of D (normalized waveguide thickness) variation; as a result, approximations within 1% are obtained for: the field intensity in the waveguide, the effective waveguide thickness, and the effective waveguide index. Field intensity maxima and effective thickness minima are found to occur for $D \cong 1.74$. The physical significance of the approximated parameters to device behavior is discussed. Simple approximation formulae for the radiation confinement factor, Γ_0, of the TE_0 mode (symmetric and asymmetric guide) and TM_0 mode (symmetric guide) are also given. Gaussian approximations are used for estimating near- and far-field intensity profiles over intermediate D ranges ($1.8 < D < 6$ and $1.5 < D < 6$, respectively) and for $\Delta n/n \leq 10\%$. The laser beamwidth in the transverse direction, $\theta_\perp$, is obtained with 4% maximum error by using a Gaussian approximation for $1.5 < D < 5$, and a corrected asymptotic formula for $0 < D < 1.5$. An accurate analytic approximation is also obtained for the laser transverse far-field pattern in the non-Gaussian region $0 < D < 1.5$, $\theta_\perp < 40°$.

1. Introduction

Semiconductor lasers of the double-heterojunction (DH) type have been extensively analyzed[1–3] due both to scientific interest as well as to their utility in a wide range of applications. A DH laser is usually represented as a three-layer slab dielectric waveguide (see Fig. 1) composed of an

* This research was sponsored in part by the U.S. Army Research Office, Durham, N.C., and in part by RCA Laboratories, Princeton, N.J.

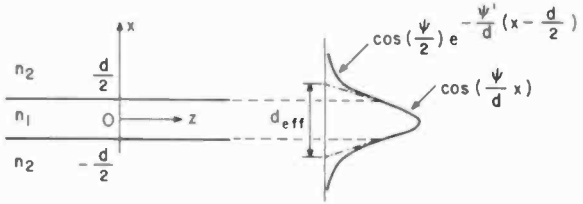

Fig. 1—Schematic representation of the fundamental transverse mode in symmetric double-heterojunction waveguides. The refractive indices of the active layer and cladding layers are n_1 and n_2, respectively, with $n_1 > n_2$. The effective guide thickness $d_{eff} = d(1 + 2/\psi')$.

active layer of refractive index n_1 and thickness d, sandwiched between passive cladding layers of refractive indices n_2 and n_3, respectively, which are less than n_1 (at the lasing wavelength). For symmetric structures (i.e., $n_2 = n_3$), the waveguide has zero cut-off thickness for the fundamental transverse mode.[4,5] In practice, the active layer thickness d is chosen such that only the fundamental mode lases.[1,2] Also the lasing mode is found in most instances to be TE polarized. Thus the symmetric DH operating in the fundamental TE_0 mode is currently the most widely used laser structure for optical communications via fibers. For this reason we chose to restrict most of our analysis to the TE_0 mode. We have reported previously[6] on beamwidth approximations for these structures. In this paper we present a complete description of the fundamental TE_0 mode (near-fields and far-fields) with the help of accurate analytical approximations. The approximations are based both on mathematical properties of certain functions as well as on physical trends in the mode behavior.

The analytical approximations that are employed, while covering wide ranges of parameter variation, have different forms over different intervals rather than a single form resulting from an asymptote combination.[7–9] For this reason we shall refer to our approximation formulae as analytical approximations over intervals (the number of intervals for a given function does not exceed two). Similar approximation methods have been used previously for Fermi energy calculations.[10]

The first part of the paper is concerned with the mode characterization in the near-field. By using approximations for the mode phase shift at the dielectric interface, ψ, various parameters directly dependent on ψ can be accurately determined (e.g., the effective waveguide index). A Gaussian approximation is obtained for near-field distributions over the range $1.8 < D < 6$ ($D \equiv (2\pi/\lambda)d\sqrt{n_1^2 - n_2^2}$ is the normalized guide thickness[4]). In the second part, a Gaussian approximation is used for describing fields in the far-field over the range $1.5 < D < 6$. The Gaussian

approximation for this interval, as well as an asymptotic approximation for the range $0 < D < 1.5$, allows a very precise (within 4%) computation of the beam angular spread in the plane perpendicular to the junction, $\theta_\perp$ (fwhp). Relatively simple expressions for the far-field intensity patterns are also presented.

2. Mode Propagation in the Waveguide

The propagation of the TE_0 mode in the symmetric waveguide of Fig. 1 is characterized by the following variation of the electric field:[4]

$$E_y(x,z) = E_0\{\cos(qx)\}e^{-j\beta z} \qquad \text{for } |x| < d/2$$

$$E_y(x,z) = E_0\{\cos(qd/2)\exp[-p(|x| - d/2)]\}e^{-j\beta z} \qquad \text{for } |x| > d/2. \quad [1]$$

Here q and p are "transverse propagation constants" in the active layer and cladding layer, respectively, β is the propagation constant along the z direction, and E_0 is the amplitude of the $E_y(x,z)$ field component. The field time dependence is omitted. After applying the proper boundary conditions one obtains the mode equation,[5]

$$\psi \tan\left(\frac{\psi}{2}\right) = \psi', \qquad [2a]$$

where $\psi = qd$ and $\psi' = pd$; ψ and ψ' are related by the condition

$$\psi^2 + \psi'^2 = \left(\frac{2\pi d}{\lambda}\right)^2 (n_1^2 - n_2^2) = D^2, \qquad [2b]$$

where D is the normalized waveguide thickness.[4] For the fundamental mode, the quantity ψ is identical to the phase shift suffered by the guided wave at the dielectric interface upon total internal reflection.[11] For this reason we shall refer to ψ as phase shift at dielectric interface. Eqs. [2a] and [2b] reduce to

$$\frac{\psi}{\cos\left(\frac{\psi}{2}\right)} = D. \qquad [2c]$$

All the information on a given structure is obtained in D, and thus Eq. [2c] unequivocally determines the phase factor ψ characteristic of the TE_0 mode propagation in the structure. In Fig. 1 we also show the electric field variation with x: the electric field follows a $\cos[(\psi/d)x]$ dependence in the active layer, and an exponential $\exp[-(\psi'/d)(|x| - d/2)]$ dependence in the cladding. The electric field amplitude E_0 is obtained by normalizing the fields to unity:

$$\int_{-\infty}^{\infty} E_y(x,z)E_y^*(x,z)dx = 1. \qquad [3a]$$

The result is

$$E_0 = \frac{1}{\sqrt{d(0.5 + 1/\psi')}} = \frac{1}{\sqrt{0.5d + 1/p}} = \sqrt{\frac{2}{d_{eff}}} \qquad [3b]$$

where d_{eff}, the effective guide width, is the sum of d and the penetration depths ($1/p$ for each cladding layer), as shown in Fig. 1. The electric field variation, as shown in Fig. 1, is an exact description of the mode in the guide. Strictly speaking, it is not identical to the laser near-field distribution, due to incident power coupling to unguided radiation modes at the laser facet.[12,13] However, this difference has been shown to be negligible in semiconductor lasers,[12,13] and thus we shall consider the field description given by Eqs. [1] as applying to the near-field distribution as well.

Another useful parameter in describing the dielectric waveguide is the effective waveguide index N.[11,14]

$$N = \frac{\beta}{k_0} = \frac{\beta}{\left(\frac{2\pi}{\lambda}\right)} = \sqrt{n_2^2 + \left(1 - \frac{\psi^2}{D^2}\right)(n_1^2 - n_2^2)}, \qquad [4a]$$

which for small index differences (i.e., $n_1 - n_2 \ll n_1$) becomes

$$N \cong n_2 + \left(1 - \frac{\psi^2}{D^2}\right)(n_1 - n_2). \qquad [4b]$$

For a laser, the presence of gain in the active layer introduces changes in the imaginary part of the dielectric constant;[15] however, for the transverse direction, we shall neglect the gain contribution to the bulk index of the active layer, since even the largest estimates for that contribution[15,16] are much smaller than $\Delta n = n_1 - n_2$ of a practical device.

3. Approximations for the Guided Mode Propagation

As seen from the previous section, ψ is the crucial parameter in determining the mode propagation in the guide. For this reason we first concentrate on finding a simple yet suitable approximation for ψ. Near the cut-off value (in this case $D = 0$) we use the property of the cosine function of being very well approximated over a relatively wide range by the first two terms of its power series expansion. For instance in approximating $\cos\theta$ by $1 - (\theta^2/2)$ over the range $0 < \theta < \pi/4$ the relative error introduced is at most 2.2%. With this approximation Eq. [2c] becomes

$$D = \frac{\psi}{\cos\left(\frac{\psi}{2}\right)} \simeq \frac{\psi}{1 - \frac{\psi^2}{8}},$$

with the solution for ψ:

$$\psi = 4\frac{\sqrt{1+(D^2/2)}-1}{D}; \qquad 0 < D < \pi. \tag{5}$$

By using Eq. [2c] it can be shown that for small errors in computing $\cos\psi/2$ [i.e. $\Delta(\cos\psi/2) = \cos\psi/2 - (1-(\psi^2/8)) \ll \cos\psi/2$] the relative error for ψ is

$$\frac{\Delta\psi}{\psi} = \frac{1}{1+(D^2/2)} \frac{\Delta\left(\cos\frac{\psi}{2}\right)}{\cos\frac{\psi}{2}} \tag{6}$$

Thus the error introduced by using $\cos\theta \simeq 1-(\theta^2/2)$ is further reduced by the term $1/\sqrt{1+(D^2/2)}$. We find that ψ can be approximated by Eq. [5] within 2% for D values up to π (the cut-off value for the first order mode). For instance, in an (AlGa)As DH guide with $\Delta n = 0.22$ and $\lambda = 0.9\ \mu$m, the case $D = \pi$ corresponds to $d = 0.36\ \mu$m. In general all regions of practical interest in cw diode lasers are within the $0 < D < \pi$ range.[1,2] Although for $D = \pi$ the first order transverse mode could be excited, the fundamental mode is the only one that is observed to lase, most probably due to the difference in mode facet reflectivity.[1] Lasing in the fundamental transverse mode was found to occur up to values of D between 5 and 7 (e.g., up to $d = 0.6$–$0.7\ \mu$m for (AlGa)As lasers with $\Delta n = 0.22$ and $\lambda = 0.9\ \mu$m[1]). For these reasons we also seek approximations for ψ in the $\pi < D < 7$ range. We start far from cut-off (i.e., $\psi = \pi$). For $\psi = \pi - \xi$, we obtain

$$D = \frac{\pi-\xi}{\cos\left(\frac{\pi}{2}-\frac{\xi}{2}\right)} = \frac{\pi-\xi}{\sin\frac{\xi}{2}} \cong \frac{\pi-\xi}{\frac{\xi}{2}} = \frac{2\psi}{\pi-\psi}. \tag{7}$$

As the D value is reduced from ∞ to π the error for the approximation $\sin(\xi/2) = \xi/2$ can be as high as 7%. However, just as in the near-cut-off case, it can be shown that the actual error in computing ψ from Eq. [2c] is less, since

$$\frac{\Delta\psi}{\psi} = \frac{2}{2+D} \frac{\Delta\left(\sin\frac{\xi}{2}\right)}{\sin\frac{\xi}{2}}. \tag{8}$$

From Eq. [7], the expression for the ψ approximation far from cut-off is

$$\psi = \frac{\pi D}{2+D}, \qquad \pi < D < \infty \tag{9}$$

with a maximum error of 2.7% at $D = \pi$. By using different methods, Reinhart et al[17] as well as Marcuse[5] have obtained virtually the same expression for the far-from-cut-off approximation. The ψ versus D plot ($0 < D < 7$) together with the two approximations, are shown in Fig. 2a. The ψ approximation formulae (i.e., Eqs. [5] and [9]) are listed in Table 1, which is a summary of the approximations used for all of the near- and far-field TE_0 mode parameters studied here, together with a previously reported[9] analytical approximation for the TE_0 radiation confinement factor, Γ_0.[17–20]

With the help of the ψ approximations several parameters describing the mode propagation can be accurately determined. Figs. 2b–2d show the variation of three such parameters: the normalized peak field intensity in the guide, E^2_{0max}, the effective waveguide thickness d_{eff}, and the effective waveguide index N. For these calculations, $Al_xGa_{1-x}As$ structures with $\Delta n = 0.1, 0.22$, and 0.34 and $n_1 = 3.6$ are considered.

The normalized field intensity in the guide can be used in calculating the peak field intensity at the facet[1,21]

$$E^2{}_{max,facet} \simeq E^2_0 \frac{\eta_0 P_0}{n_1(1-R)} 10^5 \left(\frac{\text{kV}}{\text{cm}}\right)^2$$

$$= \frac{\eta_0}{n_1(1-R)} \left(\frac{2P_0}{d_{eff}}\right) 10^5 \left(\frac{\text{kV}}{\text{cm}}\right)^2 \qquad [10]$$

where P_0 is the average power emitted per unit length expressed in mW/μm, $\eta_0 = 120\pi$ is the vacuum wave impedance, and R is the power reflection coefficient. It is interesting to notice from the last term in Eq. [10] that for the maximum field intensity at the facet, the power density per unit area is twice the average value usually considered for a laser (i.e., P_0/d_{eff}). One can use Eq. [10] to estimate laser degradation and/or catastrophic facet damage levels.[1] Fig. 2b shows that for all structures E^2_{0max} has a maximum around $D = 1.74$, which thus should be the worst place for high power laser operation (e.g., for a structure with $\Delta n = 0.22$, the case $D = 1.74$ corresponds to $d = 0.2$ μm). This maximum in field intensity also corresponds to a 60% ratio of the energy propagating in the active layer versus the total mode energy (i.e., $\Gamma_0 \cong 0.6$). The approximations shown in Fig. 2b for E^2_{0max} have a maximum error of 0.7%. Very similar accuracy is obtained in calculating d_{eff}, the effective waveguide width (Fig. 2c). As expected, the minima of the d_{eff} curves occur for $D = 1.74$. The effective width is an important parameter when energy exchange is considered[14], and also is a measure of the degree of light confinement to the active layer.

The effective index N is shown in Fig. 2d. Maximum approximation errors (i.e., at $D = \pi$) amount to only 3×10^{-3} for $\Delta n = 0.22$. In the expression for N, the factor $1 - \psi^2/D^2$ (sometimes called the normalized

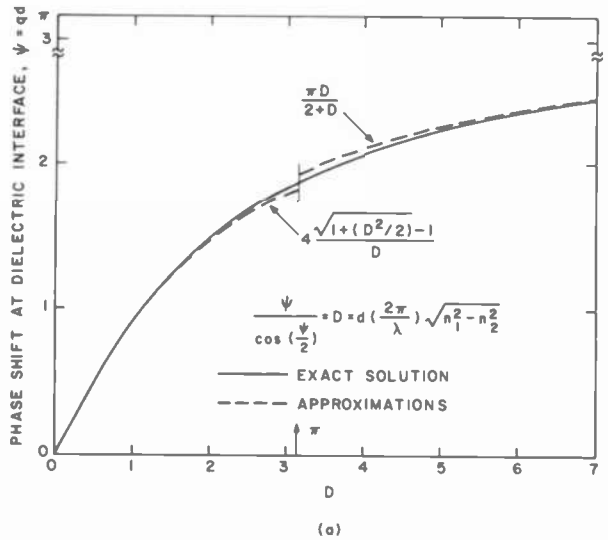

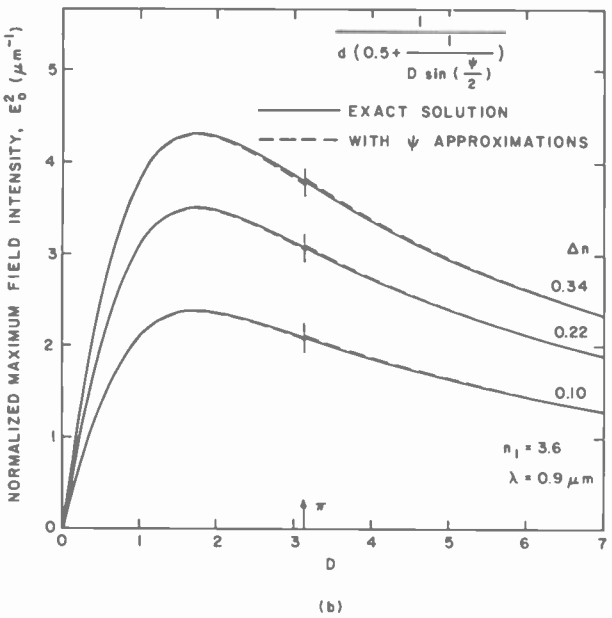

Fig. 2—The variation with respect to the normalized waveguide thickness $D \equiv (2\pi/\lambda)d\sqrt{n_1^2 - n_2^2}$ of the exact solutions (solid curves) and approximations (dashed curves) for: (a) ψ, the mode phase shift at the dielectric interface upon total internal reflection; (b) $E^2_{0(max)}$, the maximum field intensity in the guide for the case when the fields have been normalized to unity (Eq. [3a]); (continued)

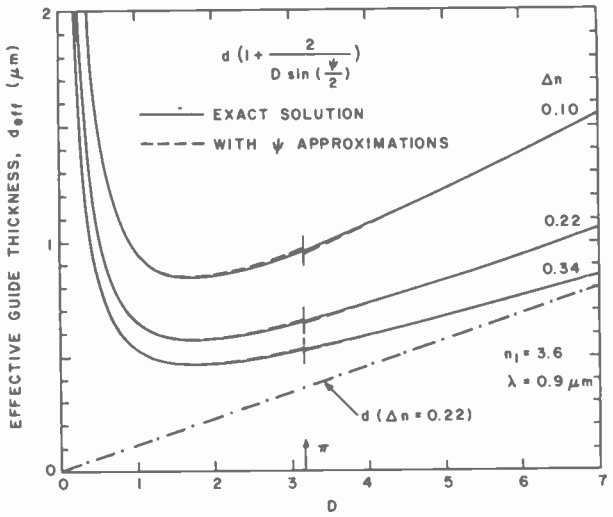

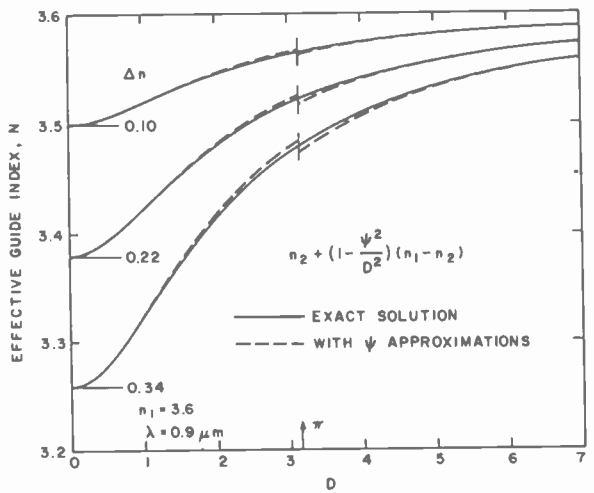

Fig. 2 (continued) (c) d_{eff}, the effective waveguide thickness (for comparison we plot d for $\Delta n = 0.22$); (d) N, the effective waveguide index. The parameters shown in (b) – (d) are plotted for $Al_{1-x}Ga_xAs$ DH structures with $n_1 = 3.6$, $\lambda = 0.9\ \mu m$, and for $\Delta n = 0.1$, 0.22, and 0.34. The extrema of the E_0^2 curves (i.e., maxima) and d_{eff} curves (i.e., minima) occur at $D = 1.74$.

guide index, b[14]) can also be written as $\sin^2(\psi/2)$, but only for the TE_0 mode (i.e., $b \cong (N - n_2)/(n_1 - n_2) = \sin^2(\psi/2)$). The formulation of b in terms of ψ only, allows a simple expression for the wavepacket longitudinal shift upon total internal reflection at the dielectric interface:[14]

$$2z_s = \frac{d\psi}{d\beta} = \frac{\lambda}{\pi \Delta n \sin\psi},$$

i.e., the Goos-Hänchen shift. Also, it can be easily shown that as $D \to 0$, b approaches asymptotically the value $D^2/4$, and consequently $(\Gamma_0/2)$,[9] rather than Γ_0.[16] The effective index is a very useful concept when considering lateral light confinement in structures of varying active layer thickness[11,22,23,42] as well as in buried lateral guides.[24,25]

The approximations presented above refer only to TE_0 modes of symmetric guides. For the TM_0 mode of symmetric guides the difference occurs in the characteristic equation [2c]. Using the expressions of Anderson[4] it can be shown that the characteristic equation is

$$\frac{\psi}{\cos\frac{\psi}{2}} = D\left(\frac{n_1}{n_2}\right)^2 \Big/ \sqrt{\left(\frac{n_2}{n_1}\right)^4 + \left(1 - \frac{n_2}{n_1}\right)^4 \cos^2\left(\frac{\psi}{2}\right)} \qquad [11]$$

Approximation formulae for ψ can be easily found by using the same methods as for the TE_0 mode. The errors thus introduced have values very similar to the ones for the TE_0 mode (i.e., <2%). Table 2 summarizes the near-field approximations for the TM_0 mode of symmetric DH structures. We include in Table 2 an approximate formula for the TM_0 mode radiation confinement factor, $\Gamma_{0(TM)}$, which was obtained in a similar manner as the $\Gamma_{0(TE)}$ analytical approximation.[9] The expression is found to agree fairly well (within 10%) with numerically calculated curves by Hakki and Paoli.[19]

For asymmetric guides ($n_3 > n_2$) an asymmetry factor $\eta = (n_1^2 - n_2^2)/(n_1^2 - n_3^2)$ is used in the characteristic mode equation [4]. Table 3 gives the characteristic equations for TE_0 and TM_0 modes and an analytical approximation for Γ_0 of asymmetric guide TE_0 modes (the same method as in Ref. [9] was used). Again explicit (approximate) solutions for ψ over the intervals $0 < D < \pi$ and $D > \pi$ could be obtained and, thus, one could approximate various near-field parameters.[5,14] However, we limit ourselves in this paper to symmetric guides ($\eta = 1$), since the approximations for the asymmetric DH case would be considerably more complex, and because few practical DH lasers are of the asymmetric type. These are treated in detail in Ref. [1].

In an article concerning light propagation in symmetric multimode guides,[7] Lotspeich uses similar mathematical approximations for ψ, but

Table 1—TE_0 Mode in Symmetric DH Structures

Parameter	Definition	Approximation	Range of $D \equiv \frac{2\pi}{\lambda} d\sqrt{n_1^2 - n_2^2}$
ψ	$\psi = D \cos\left(\frac{\psi}{2}\right)$	$4(\sqrt{1 + (D^2/2)} - 1)/D$	$0 < D < \pi$
	Characteristic equation	$\pi D/(2 + D)$	$\pi < D < \infty$
ψ'	$D \sin\left(\frac{\psi}{2}\right)$	Use formulae for ψ over same D intervals	
d_{eff}	$d\left(1 + 2/D \sin\left(\frac{\psi}{2}\right)\right)$		
$N_{(eff)}$	$n_2 + \left(1 - \frac{\psi^2}{D^2}\right)(n_1 - n_2)$		
E_0^2	$1/d\left(0.5 + 1/D \sin\left(\frac{\psi}{2}\right)\right)$		
$E_y(x)$	$E_0 \cos\left(\frac{\psi}{d}x\right), \quad \lvert x\rvert < \frac{d}{2}$ $E_0 \cos\left(\frac{\psi}{2}\right) \exp\left\{-\frac{\psi'}{d}\left(\lvert x\rvert - \frac{d}{2}\right)\right\}, \quad \lvert x\rvert > \frac{d}{2}$	$\sqrt{\frac{\sqrt{2}}{w\sqrt{\pi}}}\, e^{-x^2/w^2}$ $w = d(0.31 + 2.1/D^{3/2} + 4/D^6)$	$1.8 < D < 6$

Γ_0	$\int_{-d/2}^{+d/2} E_y^2(x)dx$	$D^2/(2+D^2)$	$0 < D < \infty$
$\theta_\perp$	$\frac{I(\theta_\perp/2)}{I(0)} = \frac{1}{2}$	$2\tan^{-1}(\lambda\, 0.59/\pi w_0)$ $w_0 = d(0.31 + 3.15/D^{3/2} + 2/D^6)$	$1.5 < D < 6$ $\frac{\Delta n}{n} < 10\%$
		$0.65\, D\sqrt{n_1^2 - n_2^2}/(1 + 0.086\kappa D^2)$ $\kappa = [2.52\sqrt{n_1^2 - n_2^2}/\tan^{-1}(0.36\sqrt{n_1^2 - n_2^2})] - 5.17$	$0 < D < 1.5$
$\frac{I(\theta)}{I(0)}$	$\frac{\cos^2\theta \left\lvert \int_{-\infty}^{+\infty} E_y(x')e^{-2\pi j x' \sin\theta/\lambda} dx \right\rvert^2}{\left\lvert \int_{-\infty}^{\infty} E_y(x')dx \right\rvert^2}$	$\exp\left[-\frac{0.69\theta^2}{(\theta_{1/2})^2}\right]$; $\theta_{1/2} = \frac{\theta_\perp}{2}$	$1.5 < D < 6$ $\frac{\Delta n}{n} < 10\%$
		$\cos^2\theta[\psi'\psi^2(2\psi' - A^2)/2(\psi^2 - A^2)(\psi'^2 + A^2)]^2$ $A = D\sin\theta/\sqrt{n_1^2 - n_2^2}$	$0 < D < 1.5$ $\theta_\perp < 40°$

ψ = product of the transverse progagation constant q and the active layer thickness d (also the TE_0 mode phase shift at the dielectric interface upon total internal reflection);

ψ' = product of the exponential decay constant p and the active layer thickness d;

d_{eff} = effective waveguide thickness; N = effective waveguide index; E_0^2 = maximum field intensity in the guide for the case when the fields are normalized to unity (Eq. [3a]); $E_y(x)$ = optical field distribution in the guide;

Γ_0 = radiation confinement factor[9]; $\theta_\perp$ = half-power beamwidth of the laser radiation pattern; $I(\theta)/I(0)$ = relative far-field distribution of the beam intensity.

Table 2—TM_0 Mode in Symmetric DH Structures (Near-Field)

Parameter	Definition; $m = n_2/n_1$	Approximation	Range of $D \equiv \frac{2\pi}{\lambda} d\sqrt{n_1^2 - n_2^2}$
ψ	$\psi = D \Big/ \sqrt{1 + m^4 \tan^2\left(\frac{\psi}{2}\right)}$ Characteristic equation	$4\sqrt{\frac{2 + (D^2/2) - 2\sqrt{1 + (D^2/2)(2m^4 - 1)}}{D^2 + 16(1 - m^4)}}$	$0 < D < \pi$
		$\pi D/(2m + D)$	$\pi < D < \infty$
ψ'	$\sqrt{D^2 - \psi^2}$	Use formulae for ψ over same D intervals	
d_{eff}	$d(1 + 2m^2D^2/[\psi'(D^2 - \psi^2(1 - m^4))])$		
H_0^2	$2/d_{eff}$		
$N_{(eff)}$	$n_2 + \left(1 - \frac{\psi^2}{D^2}\right)(n_1 - n_2)$		
Γ_0	$\int_{-d/2}^{d/2} E^2(x)dx$	$m^4D^2/(2 + m^4D^2)$	$0 < D < \infty$

Table 3—Asymmetric DH Structures

Mode	Characteristic Equation
TE_0	$\psi^2 = \sqrt{(D^2 - \psi^2)(\eta D^2 - \psi^2)} + \sqrt{\eta}\, D^2 \cos\psi$
TM_0	$\psi = \tan^{-1} \frac{n_1^2}{n_2^2} \frac{\sqrt{D^2 - \psi^2}}{\psi} + \tan^{-1} \frac{n_1^2}{n_3^2} \frac{\sqrt{\eta D^2 - \psi^2}}{\psi}$
Parameter	Approximation; $1 < \eta < \infty$
$\Gamma_{0_{TE}}$	$\frac{\Gamma_0}{1 + \Gamma_0'}; \quad \Gamma_0' = \frac{2\sqrt{\eta}}{1 + \sqrt{\eta}} D(D - \tan^{-1}\sqrt{\eta - 1}) \times \left[1 + \frac{1}{\sqrt{\eta^2\, 1 + (\eta - 1)/(D - \tan^{-1}\sqrt{\eta - 1})^2}}\right]^{-1}$

Definitions:

$$D \equiv \frac{2\pi}{\lambda} d\sqrt{n_1^2 - n_2^2};\ \eta = \frac{n_1^2 - n_2^2}{n_1^2 - n_3^2};\ n_3 > n_2$$

$$\Gamma_{0_{TE}} = \int_{-d/2}^{d/2} E_y^2(x)dx$$

only over limited ranges, since his purpose is to find ψ asymptotes. The asymptotes are then used in a linear combination with variable coefficients chosen to provide a good ψ approximation. While very accurate, the resulting ψ formula is rather complicated. We believe that our relatively simple approximations for ψ, over intervals of D, are more than adequate in precisely describing the behavior of fundamental transverse modes in symmetric guides.

4. Approximations of the Mode Near-Field Distribution

The electric field variation in the transverse direction (Eq. [1]) as well as the peak field amplitude (Eq. [3]) depend directly on ψ, the phase shift at the dielectric interface. Since, as shown in the previous section, ψ can be approximated very well over its whole range ($0 \leq \psi \leq \pi$), a precise determination of the mode field distribution in the active layer as well as in the cladding layers is readily obtainable. However, in many cases (e.g. scattering loss calculations, radiation loss calculations, etc.) the description of the near-field by a single function would greatly simplify the analysis. One such single-function field description can be obtained by using the Epstein-layer model[26], but the expressions that have to be used are very complicated. In a recent paper[27] Marcuse presents Gaussian field approximations for the fundamental modes of graded-index and step-index weakly guiding fibers ($\Delta n \ll n_1$). We also use a Gaussian approximation in trying to describe the field distribution in symmetric double-heterostructure slab waveguides. In Sections 6 and 8, the Gaussian approximation concept is extended to the transverse mode far-field pattern. Just as in the case of fibers[27] the Gaussian approximation for the fundamental mode is good only over a certain range

of D, the normalized guide thickness. For small D's the mode lies mostly outside the active layer and thus it assumes a double-exponential-like shape. At the other extreme, when the mode is mostly confined to the guide, (i.e., large D's) the field distribution will be cosine-like. We fit a Gaussian to the field distribution in the intermediate region[28] (i.e. a field shape made of both a cosine curve and exponential curves).

A Gaussian field distribution is described by the following expression:

$$E_G(x,z) = \sqrt{\frac{\sqrt{2}}{w\sqrt{\pi}}} \exp\left\{-\frac{x^2}{w^2} - i\beta z\right\}; \qquad -\infty < x < \infty, \quad [12]$$

where w is the Gaussian beam width parameter, defined as the value of x at which the field amplitude is $1/e$ of the peak amplitude. The peak amplitude was determined by normalizing the fields to unity. The Gaussian field distribution Eq. [12] is to be compared to the TE_0 mode field distribution $E_y(x,z)$ as defined by Eqs. [1] and [3].

The ideal approach for the Gaussian fit is to find the beam width parameter w such as to maximize the variational integral[27]

$$\int_{-\infty}^{\infty} E_G(x) E_y(x) dx. \qquad [13]$$

However, this requires extensive numerical calculations. We chose to first determine the asymptotic value of w/d as $d \to \infty$ and then find the rest of the function w/d (D) by trial and error. As d tends to ∞, $d_{eff} \to d$ and $\psi \to \infty$; this gives for $E_y(x)$ the form $\sqrt{2}/\sqrt{d} \cos(\pi x/d)$. Thus, we have to maximize the expression:

$$\frac{\sqrt{2}}{\sqrt{d}} \sqrt{\frac{\sqrt{2}}{w\sqrt{\pi}}} \int_{-\infty}^{\infty} \cos\left(\frac{\pi x}{d}\right) \exp\{-x^2/w^2\} dx$$
$$= \sqrt{\frac{2\sqrt{2\pi}w}{d}} \exp\left\{-\frac{\pi^2 w^2}{4d^2}\right\}. \qquad [14]$$

Assuming $w = \alpha d$, it can be shown that Eq. [14] assumes a maximum for $\alpha = 1/\pi \simeq 0.31$. Therefore $w/d = 0.31 + f(D)$, where $f(D) \to 0$ as $D \to \infty$. To find $f(D)$ we use as a trial function $f(D) = (\beta/D^{3/2}) + (\gamma/D^6)$, which is similar to the function empirically determined by Marcuse for fibers. By trial and error, and also by using the correlation between the field in the guide and a Gaussian approximation for the far-field (see Section 7), we find a best fit for

$$\frac{w}{d} = 0.31 + \frac{2.1}{D^{3/2}} + \frac{4}{D^6}, \qquad 1.8 < D < 6. \qquad [15]$$

Figs. 3a, b, c show comparisons of Gaussian field distributions versus the exact solutions for $D = 2$, 3, and 4 and $\Delta n = 0.22$ ($n_1 = 3.6$; $\lambda = 0.9$

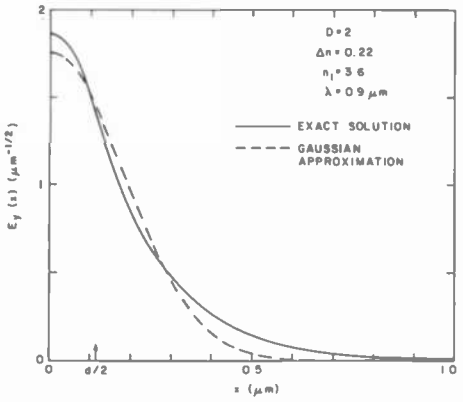

(a)

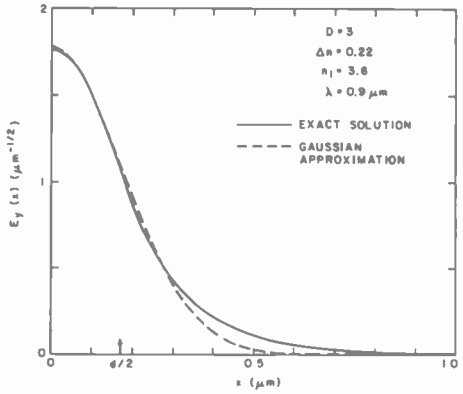

(b)

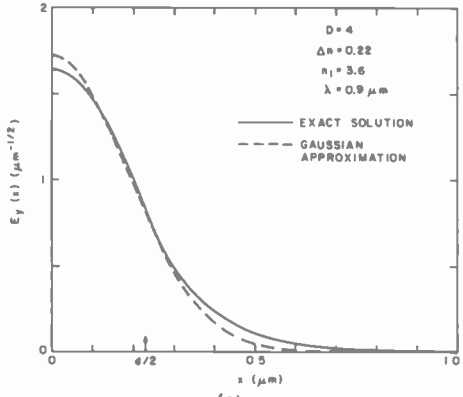

(c)

Fig. 3—Comparison of near-field distribution profiles (solid curves) $E_y(x)$ (Eqs. [1] and [3b]) versus the Gaussian approximation (dashed curves) $E_G = \sqrt{\sqrt{2}/w\sqrt{\pi}}\exp(-x^2/w^2)$ with $w = d(0.31 + 2.1/D^{3/2} + 4/D^6)$, for: (a) $D = 2$, $\Delta n = 0.22$; (b) $D = 3$, $\Delta n = 0.22$; (c) $D = 4$, $\Delta n = 0.22$. All graphs are plotted for structures with $n_1 = 3.6$ and $\lambda = 0.9$ μm.

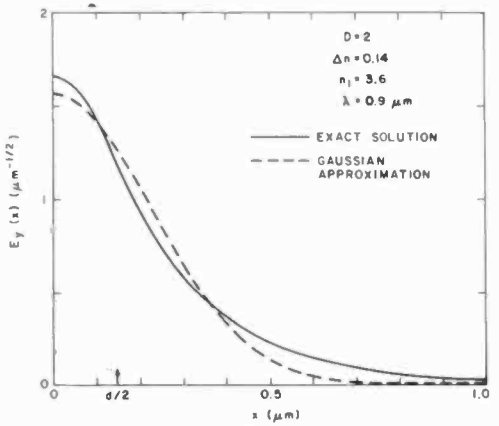

(d)

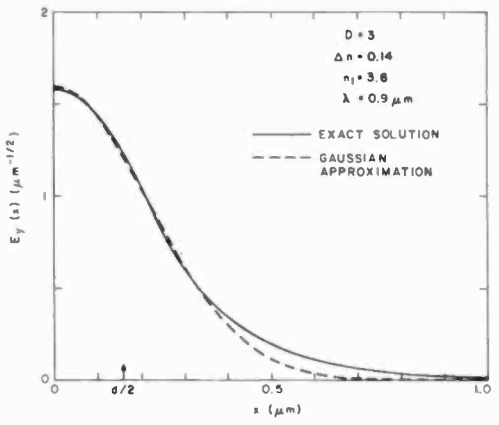

(e)

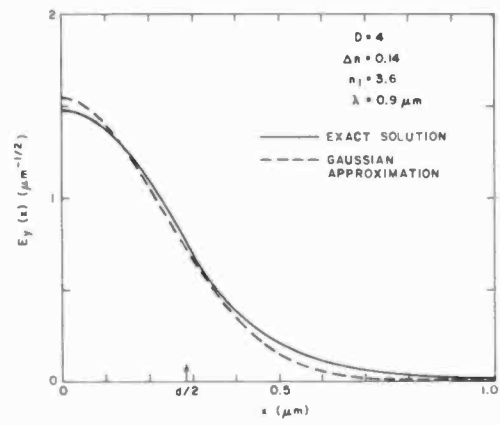

(f)

Fig. 3 (continued)—(d) $D = 2$, $\Delta n = 0.14$; (e) $D = 3$, $\Delta n = 0.14$; (f) $D = 4$, $\Delta n = 0.14$.

μm). The curves agree very well for D values around 3 and 4. Figs. 3d, e, f show similar comparisons for the case $\Delta n = 0.14$. The fit is still very good. As mentioned previously, the field distribution in the guide is almost identical to the field distribution on the facet, and thus Eqs. [12] and [15] give a Gaussian approximation for the near-field as well.

Reinhart et al[17] have shown that a Gaussian description of the near-field is useful when computing mode reflection coefficients in DH structures with $D \geq 3$. The authors claim as an upper limit for an acceptable Gaussian fit the condition $\psi < 2.4$, which corresponds to $D = 6.6$ and thus agrees with our findings. For $D < 2$ (e.g., $d < 0.25$ μm when $\Delta n = 0.22$, $n_1 = 3.6$, and $\lambda = 0.9$ μm) the Gaussian near-field approximation will be increasingly poor and thus cannot be used for predicting modal facet reflection coefficients.[29] In a recent article, Utaka et al[30] use an expression similar to Eq. [15] for a near-field Gaussian approximation, which appears to be good over the interval $\pi < D < 6$.

5. Mode Far-Field Intensity Distribution

The lasing mode far-field intensity distribution is the laser radiation pattern at large distance from the mirror facet ($r \gg \lambda$). For the transverse mode case, we are interested in the electric field distribution in the plane perpendicular to the junction as a function of θ, the angle with respect to the normal to the laser facet. When θ assumes small values (i.e., $\cos\theta \simeq 1$), the far-field angular field distribution is obtained as the Fourier transform of the near-field distribution (i.e., the aperture field)[1,18,28]

$$G'\left(\frac{\sin\theta}{\lambda}\right) = \int_{-\infty}^{\infty} E_y'(x) \exp\left[-2\pi j x \left(\frac{\sin\theta}{\lambda}\right)\right] dx, \qquad [16]$$

where $E_y'(x)$ stands for the field distribution at the laser facet. The far-field dependence on r, the distance from the observation point to the center of the near-field distribution (i.e. $[\exp\{-j(2\pi/\lambda)r\}]/r$), is omitted since we are interested only in the field variation with the angle θ at fixed r. For large angles however, an obliquity factor $g(\theta)$ must be used.[28,29,31–33] Then the correct expression for the far-field angular field distribution $E(\theta)$ is

$$E(\theta) = g(\theta)G'\left(\frac{\sin\theta}{\lambda}\right). \qquad [17]$$

In order to calculate $E(\theta)$ some simplifications are made. First one computes the Fourier transform of the field inside the guide, $G(\sin\theta/\lambda)$,[1,18,28] since, as mentioned previously, $E_y(x)$ is only slightly different from the field distribution on the facet $E_y'(x)$. Then, for the obliquity factor, the function $\cos\theta$ is used, which has been shown theoretically[31]

as well as experimentally[1,28] to be a very good approximation of $g(\theta)$. Thus the far-field intensity pattern $I(\theta)$ is given by

$$I(\theta) = |E(\theta)|^2 = \cos^2\theta \left| G\left(\frac{\sin\theta}{\lambda}\right)\right|^2. \quad [18]$$

While this expression is found to very accurately predict experimental far-field patterns,[1,28,32] its computation is difficult since $G(\sin\theta/\lambda)$ is a rather complicated expression. Furthermore, in order to find the beamwidth $\theta_\perp = 2\theta_{1/2}$ (fwhp) the transcendental equation $[I(\theta_{1/2})/I(0)] = 1/2$ has to be solved. Dumke[8] has found an approximation formula for $\theta_\perp$ for very thin active layers, by combining the asymptotes of $\theta_\perp$ as $d \to 0$ and as $d \to \infty$. However, as will be shown in the Section 7, Dumke's formula is a reasonably good approximation only over a very limited parameter range ($d < 0.1$ μm and $\Delta n < 0.22$). In the next section we use a Gaussian approximation of the far-field pattern over the range $1.5 < D < 6$ in order to find very accurate expressions for $\theta_\perp$ over wide parameters ranges ($0 < D < 6$ and $\Delta n/n \leq 10\%$). Furthermore we also can predict fairly well the far-field intensity patterns.

6. Beamwidth Gaussian Approximation ($1.5 < D < 6$)

It was shown in Section 4 that the field distribution in the waveguide can be described quite accurately by a Gaussian field distribution over the D range 1.8 to 6. Then, it should not be surprising to find a Gaussian distribution in the far-field as well. Furthermore the obliquity factor can be approximated by a Gaussian-like function[32]

$$\cos\theta \simeq \exp\left\{-\frac{\theta^2}{2}\right\} \quad [19]$$

within 2% for $0 < \theta < 40°$.

The angular beam spread for a fundamental Gaussian beam has the form[34,35]:

$$\theta_{beam} = \tan^{-1}\left(\frac{\lambda}{\pi w_0}\right), \quad [20]$$

where w_0 is the beam minimum waist and θ is the angle measured from the z axis. The parameter θ_{beam} is the angle at $1/e$ of the far-field angular field distribution. In order to obtain $\theta_{1/2}$ (the angle at 1/2 of the far-field intensity distribution), a factor of $0.59 = \sqrt{(\ln 2)/2}$ should be added in Eq. [20],

$$\theta_{1/2} = \tan^{-1}\left(\frac{\lambda 0.59}{\pi w_0}\right). \quad [21]$$

To find w_0 by starting in the near-field is not an easy task since, as

mentioned above, an obliquity factor has to be considered for the far-field distribution. For this reason we chose to find w_0 by fitting the expression $\theta_\perp = 2\theta_{1/2} = 2\tan^{-1}(\lambda 0.59/\pi w_0)$ to numerically calculated beamwidth curves by Butler and Kressel.[1] From the Gaussian fit of the near-field distribution, we know that w_0 should have the form $w_0/d = 0.31 + \beta/D^{3/2} + \gamma/D^6$. The best fit to numerical computed $\theta_\perp$ curves is found for $\beta = 3.15$ and $\gamma = 2$ over the range $1.5 < D < 6$. Thus we obtain for the beamwidth the approximation formula:

$$\theta_\perp = 2\tan^{-1}\left(\frac{\lambda 0.59}{\pi w_0}\right), \qquad [22]$$

with

$$w_0 = d[0.31 + (3.15/D^{3/2}) + (2/D^6)] \qquad \text{for } 1.5 < D < 6.$$

The actual beam minimum waist is not w_0 but w, the Gaussian parameter of the near-field profile (see Eq. [12]). The difference is due to the obliquity factor $g(\theta)$. It can be easily checked, via the far-field intensity pattern Eqs. [18] and [24], that Eq. [22] contains the contributions of both the near-field Gaussian approximation, Eq. [12], as well as the obliquity factor, $\cos\theta$. Fig. 4 shows a comparison of the Gaussian approximation ($D > 1.5$) versus numerical data by Butler and Kressel for various $\Delta n = n_1 - n_2$ values with $n_1 = 3.6$ and $\lambda = 0.9\ \mu$m. The agreement is very good (within 2%) for Δn values between 0.14 and 0.26, which also is the region of most interest in $Al_xGa_{1-x}As$ lasers ($\Delta n \simeq 0.65\ \Delta x$)[1]. It must be stressed that the numerical calculations by Butler and Kressel agree extremely well with experimental data of various workers.[18,32,36] The curve $D = \pi$ in Fig. 4 signifies the cutoff for excitation of the first order mode and also happens to be the locus of the $\theta_\perp$ curves maxima for given Δn. As mentioned previously, although the first order mode can be excited, due to modal gain considerations it does not lase until D has values somewhere between 5 and 6 (e.g., 0.6–0.7 μm for $\Delta n = 0.18$).[1,2] Thus the $\theta_\perp$ curves have to be considered up to those D values. From Fig. 4 it can be seen that for $1.5 < D < 5$ the Gaussian approximation is good within 4% for $0.06 < \Delta n < 0.34$. Yet as $D \to \infty$, Eq. [22] gives $\theta_\perp \to 1.2\ \lambda/d$ which is the expected behavior in the limit that the near-field distribution becomes a cosine function.[8] For large Δn values (e.g., $\Delta n \geq 0.42$), Eq. [22] fails to give a good approximation for $\theta_\perp$, which we expect since both the obliquity factor and the near-field distribution[27] tend to diverge from a Gaussian-like shape. Since the $\theta_\perp$ formula applies for any type of symmetric double-heterojunction (e.g., GaAs-AlGaAs, InP-InGaAsP), we conclude that the Gaussian approximation for the fundamental mode beamwidth is accurate within 4% for $1.5 < D < 5$ and for $\Delta n/n < 10\%$.

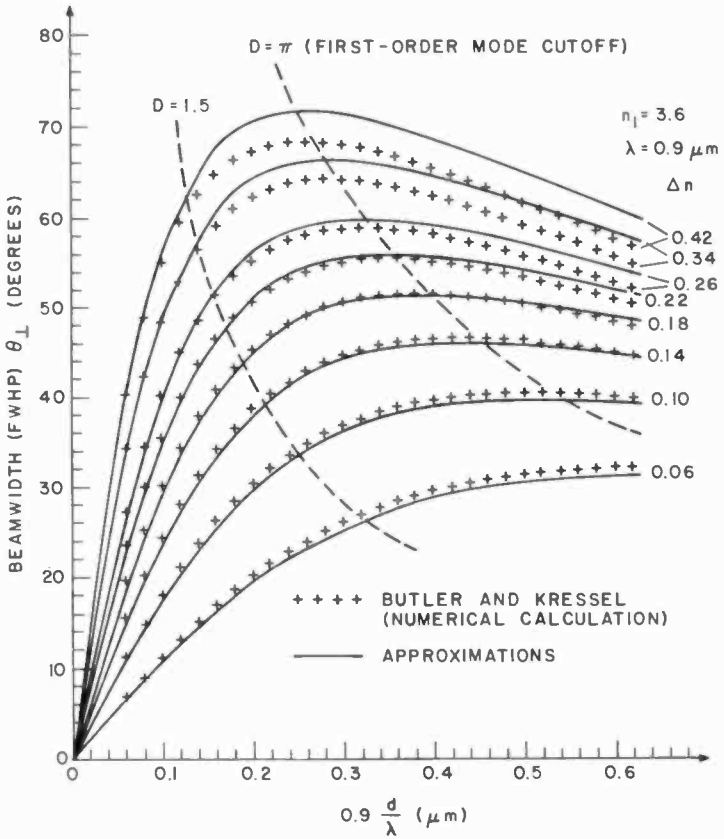

Fig. 4—The beamwidth $\theta_\perp$ (full width at half power) for the laser radiation pattern, in the plane perpendicular to the junction, as a function of a wavelength normalized active layer thickness, and for different index steps Δn (0.06 to 0.42). The crosses correspond to numerically calculated points by Butler and Kressel.[1] The solid curves are approximations: an asymptotic approximation for $0 < D < 1.5$ (see Fig. 5) and a Gaussian approximation for $1.5 < D < 6$ (i.e., $\theta_\perp = 2 \tan^{-1}[\lambda 0.59/\pi w_0]$ with $w_0 = d[0.31 + 3.15/D^{3/2} + 2/D^6]$, where $D = [2\pi/\lambda]d\sqrt{n_1^2 - n_2^2}$).

7. Beamwidth for Thin Active Layers ($0 < D < 1.5$)

For $D < 1.5$, the beamwidth Gaussian approximation Eq. [22] is no longer appropriate. The near-field patterns have double-exponential shapes[28] and become relatively wide, which in turn gives far-field angular distributions of narrow beamwidth and non-Gaussian shapes. In order to approximate the beamwidth we use Dumke's formula[8] with a correction factor κ chosen to match the Gaussian approximation at $D = 1.5$. We thus obtain

$$\theta_\perp \cong \frac{4.09(d/\lambda)(n_1^2 - n_2^2)}{1 + 3.39\kappa(d/\lambda)^2(n_1^2 - n_2^2)}$$

$$= \frac{0.65D\sqrt{n_1^2 - n_2^2}}{1 + 0.086\kappa D^2}; \qquad 0 < D < 1.5 \quad [23]$$

with

$$\kappa = \frac{2.52\sqrt{n_1^2 - n_2^2}}{\tan^{-1}(0.36\sqrt{n_1^2 - n_2^2})} - 5.17.$$

As can be seen from Fig. 4, this approximation is very good. The factor κ varies almost linearly between 1.95 and 2.9 as Δn takes values between 0.06 and 0.6 (e.g., $\kappa = 2.2$ when $\Delta n = 0.18$). For the reader's benefit, we show in Fig. 5 values of $\theta_\perp$ over the very thin active layer region $0 < 0.9\, d/\lambda < 0.2\ \mu$m, and for additional Δn values (0.5 and 0.6). We also extend the approximation Eq. [22] beyond the $D = 1.5$ limit up to $d = 0.2\ \mu$m (for $\Delta n > 0.18$). For comparison, we plot dashed curves[8] corresponding to the case $\kappa = 1$, for two Δn values, 0.22 and 0.6. It appears that Dumke's formula considerably overestimates the beamwidth for $d > 0.1\ \mu$m at $\Delta n = 0.22$ and for $d > 0.05\ \mu$m at $\Delta n = 0.6$. The previously reported[8] relatively good fit of Dumke's formula to beamwidth curves published by Casey et al[18] is thought to arise from the fact that in the latter study the obliquity factor was not considered.[32,35] The $\theta_\perp$ curves of Fig. 5 should prove useful for an estimate of Δn once $\theta_\perp$, d, and λ have been accurately determined experimentally.[1]

8. Far-Field Patterns

We showed in Section 6 that a Gaussian approximation is a very good fit when trying the estimate the laser beamwidth for $D > 1.5$ and $\Delta n/n < 10\%$. We thus expect that for the same ranges of parameter variation, the far-field intensity pattern is very much like a Gaussian curve. Therefore we assume:

$$I(\theta) = \exp\left\{-\frac{0.69\theta^2}{(\theta_{1/2})^2}\right\}; \qquad D > 1.5; \frac{\Delta n}{n} < 10\%, \quad [24]$$

where $\theta_{1/2} = \theta_\perp/2$ is given by Eq. [22] and the factor 0.69 is introduced such that when $\theta = \theta_{1/2}$, $I(\theta)$ drops to half its value at $\theta = 0$. Previously, Lewin[32] also proposed a Gaussian form for the far-field intensity pattern, but he assumed it should work only for small angles and with no restriction on D. In the same article Lewin finds very good agreement between his Gaussian approximation corrected for the obliquity factor, and an experimental far-field pattern of a structure with $D = 1.52$ ($\Delta x = 0.3$, $d = 0.18$, $\lambda = 0.89\ \mu$m). As shown in Figs. 6a and b, we also find good fit to Gaussian curves of experimentally obtained far-field patterns from structures with $D > 1.5$. Thus, Fig. 6a shows an excellent agreement between a Gaussian and the experimental[37] far-field intensity profile of a structure with $D = 3.68$ and $\Delta n = 0.08$ ($\theta_{1/2} = 19°$). For structures

with $\theta_{1/2}$ larger than $\simeq 25°$, there is some disagreement in the curve tails as shown in Fig. 6b (i.e., for a Gaussian versus experimental[33] far-field of $\theta_{1/2} = 25.5°$ obtained from a laser with $D = 2.16$). We believe that this effect is mainly due to the obliquity factor deviation from a Gaussian-like form for $\theta > 40°$. Overall though, down to approximately 25% of the peak

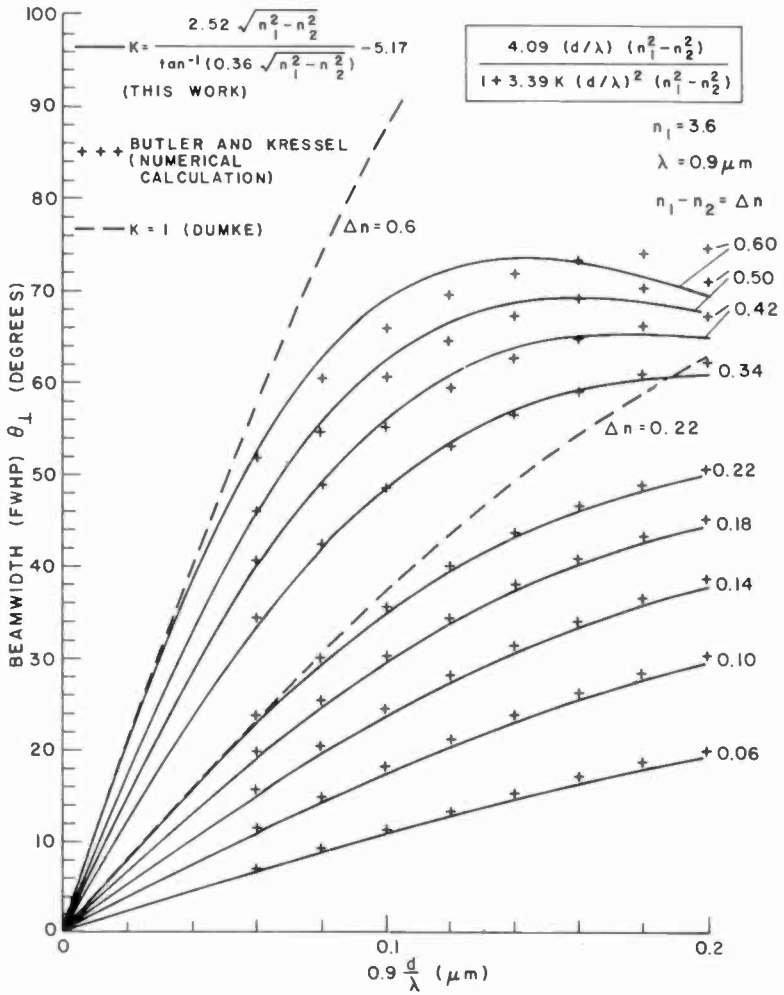

Fig. 5—Laser radiation pattern beamwidth $\theta_\perp$ for thin active layers (i.e., $0 < 0.9d/\lambda < 0.2$ μm). The crosses correspond to Butler and Kressel's numerical calculations,[1] while the solid curves correspond to the approximation formula inserted in the top right corner. The case $\kappa = 1$(Dumke's formula[8]) is represented by dashed curves for $\Delta n = 0.22$ and 0.6. All curves are computed for DH structures with $n_1 = 3.6$ and $\lambda = 0.9$ μm.

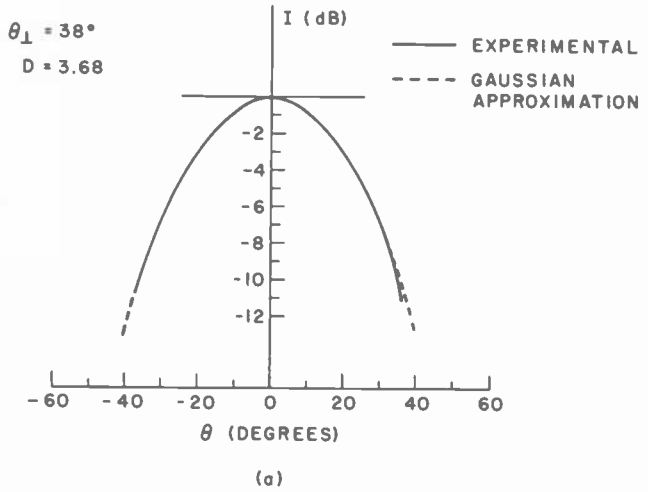

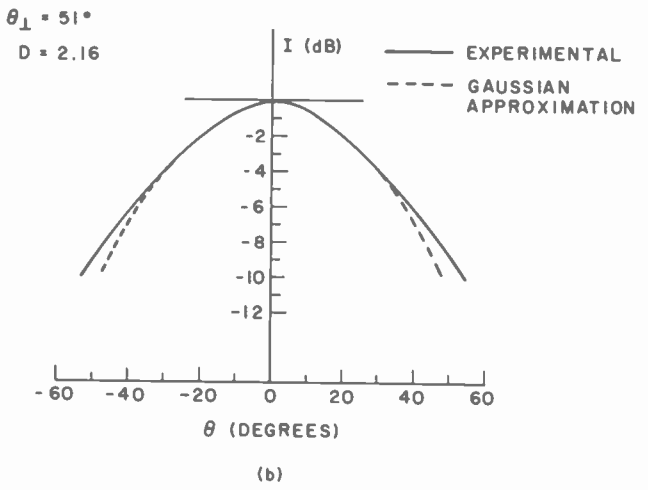

Fig. 6—Comparison of experimental (solid curves) far-field patterns (from Refs. [37] and [33], respectively) to the Gaussian approximation (dashed curves) $I(\theta)/I(0) = \exp(-0.69\,\theta^2/(\theta_{1/2})^2)$, where $\theta_{1/2} = \theta_\perp/2$ is given by Eq. [22]: (a) $d = 0.7\ \mu$m, $\Delta n = 0.08$; $D = 3.68$, $\theta_\perp = 38°$; (b) $d = 0.25\ \mu$m, $\Delta n = 0.22$; D = 2.16, $\theta_\perp = 51°$. The patterns were obtained from structures with $n_1 = 3.6$, $\lambda = 0.9\ \mu$m and TE polarized beams.

intensity, the Gaussian approximation appears to be a very good estimate of the far-field intensity profile.

Since the beamwidth Gaussian approximation does not apply for structures with $D < 1.5$, we expect that for the same D range a Gaussian curve cannot closely fit the far-field pattern. For comparison we show in Fig. 7 a Gaussian curve with $\theta_{1/2} = 11°$ superposed over the far-field distribution of a laser with $\theta_\perp = 22°$.[38] While there is fairly good agreement from the peak intensity to its half-height (−3 dB), below −3 dB the Gaussian curve severely underestimates the far-field distribution. Similar results were obtained when comparing Gaussian curves to numerically calculated far-field patterns of structures with beamwidths below 30° and $D < 1.5$.[1] One is left with the alternative of using the Fourier transform. For $\theta < 45°$ and $D < 1.5$, it can be shown that the near-field distribution Fourier transform[28] can be simplified; as a result, the relative far-field intensity distribution is

$$\frac{I(\theta)}{I(0)} = \cos^2\theta \left[\frac{\psi'\psi^2(2\psi' - A^2)}{2(\psi^2 - A^2)(\psi'^2 + A^2)}\right]^2; \; D < 1.5, \theta < 45°, \quad [25]$$

where $A = (2\pi/\lambda)\, d \sin\theta$, $\psi' = D \sin(\psi/2)$, and for ψ one can use the approximation formula obtained in Section 3 (i.e., $\psi = 4(\sqrt{1 + (D^2/2)} - 1)/D$). For various low beamwidth data we find that the condition $\theta < 45°$ is equivalent to $\theta_\perp < 40°$ if $\theta = 45°$ corresponds to a −10 dB drop in peak intensity (i.e., if $I(45°)/I(0) = 0.1$). In Fig. 7, we compare the approximation Eq. [25] to the experimental far-field with $\theta_\perp = 22°$, and find a very good agreement.

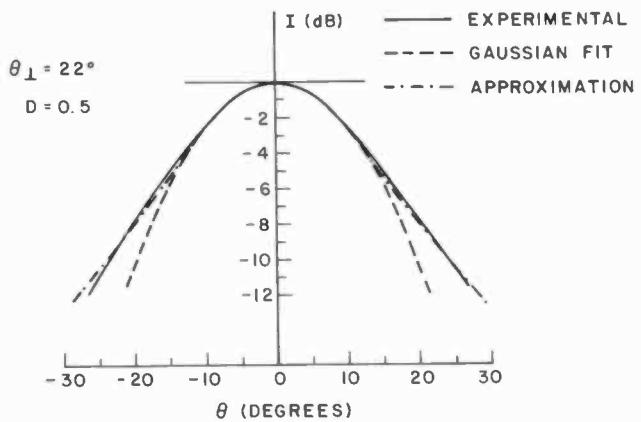

Fig. 7—Comparison of experimental (solid curves) far-field patterns of a low-beamwidth TE polarized laser ($\theta_\perp = 22°$)[38] to a Gaussian of same full-width at half-power (dashed curves), and to a Fourier transform approximation (dash-and-dot curve) for angles $\theta < 45°$ (see Eq. [25]). The structure has $D = 0.5$ and $\Delta n = 0.18$.

The far-fields (beamwidth and intensity profiles) for TM_0 modes are not treated due to the difficulty in calculations and lack of experimental data. However, from the work of Butler and Kressel[1] it turns out that, for the same DH structure, there are only slight differences between TE_0 and TM_0 mode patterns. Thus the above approximations for far-fields should be reasonable estimates for TM_0 modes as well.

For optical communications, the far-field intensity pattern determines the coupling efficiency to optical fibers when no lenses are used. It appears from our analysis that for low-numerical-aperture fibers (i.e., those of acceptance angles less than 20°), a Gaussian description of the laser beam in the plane perpendicular to the junction is fairly accurate. Then, if the laser oscillates in a fundamental lateral mode, the whole beam could be considered Gaussian. When lenses are used such that the lasing spot is imaged onto the fiber end, the degree to which the imaged field is Gaussian-like, as well as the ratio of its spot size to the fiber core radius or to the fiber spot size[27,39,40] definitely influences the coupling efficiency.

9. Conclusion

This paper contains a series of relatively simple yet very accurate analytical approximations for parameters characterizing the near- and far-field distributions of the TE_0 mode in symmetric DH lasers. For the reader's convenience we have summarized all these approximations in Table 1. As can be seen, all parameters of interest can be written as functions of only two quantities: the normalized waveguide thickness, D, and the square root of the difference in real parts of the layers' dielectric constants $\sqrt{n_1^2 - n_2^2}$. Aside from obvious simplifications in the calculation of various device parameters, the approximations should allow explicit analytical solutions for various laser optimization problems as well as physical insights into trends in device behavior. The ability to approximate near- and far-field TE_0 mode intensity patterns by a Gaussian function (over certain ranges of D and Δn) should prove useful for solving problems of scattering, radiation loss, and/or coupling to optical fibers.

The various formulae contained in the paper, together with the analytical approximations for the radiation confinement factor Γ_0[9] (i.e., $\Gamma_0 \cong D^2/(2 + D^2)$) and the mode reflection coefficient R_0[41] give a complete analytical picture for the TE_0 mode propagation inside and outside the laser. As mentioned previously, similar approximation methods can be extended to the TM_0 mode propagation in symmetric waveguides and/or fundamental mode propagation in asymmetric waveguides, by starting from their corresponding characteristic equations (Tables 2 and 3).

Acknowledgements

The author gratefully acknowledges the kind assistance of M. Ettenberg, J. K. Butler, H. Kressel and H. S. Sommers in supplying some of their calculated and experimental results. He also thanks them and C. J. Nuese for helpful discussions.

References:

[1] H. Kressel and J. K. Butler, *Semiconductor Lasers and Heterojunction LED's*, Academic Press, New York, 1977; and J. K. Butler and H. Kressel, "Design Curves for Double-Heterojunction Laser Diodes," *RCA Review*, **38**, p. 542, 1977.

[2] M. B. Panish, "Heterostructure injection lasers," *Proc. IEEE*, **64**, p. 1512, Oct. 1976.

[3] Y. Nannichi, "Recent Progress in Semiconductor Lasers," *Jpn. J. Appl. Phys.*, **16**, p. 2089, Dec. 1977.

[4] W. W. Anderson, "Mode confinement and gain in injection lasers," *IEEE J. Quantum Electron.*, **QE-1**, p. 228, Sept. 1965.

[5] D. Marcuse, *Light Transmission in Optics*, Van Nostrand Reinhold, New York, 1972.

[6] D. Botez and M. Ettenberg, "Beamwidth Approximations for the Fundamental Mode in Symmetric Double-Heterojunction Lasers," *J. Quantum Electron.*, **QE-14**, p. 827, Nov. 1978.

[7] J. F. Lotspeich, "Explicit general eigenvalue solutions for dielectric slab waveguides," *Appl. Optics*, **14**, p. 327, Feb. 1975.

[8] W. P. Dumke, "The angular beam divergence in double-heterojunction lasers with very thin active regions," *IEEE J. Quantum Electron.*, **11**, p. 400, July 1975.

[9] D. Botez, "Analytical Approximation of the Radiation Confinement Factor for the TE_0 Mode of a Double Heterojunction Laser," *IEEE J. Quantum Electron.*, **14**, p. 230, April 1978.

[10] W. B. Joyce, "Analytic approximations for the Fermi energy in (AlGa)As," *Appl. Phys. Lett.*, **32**, p. 680, May 1978.

[11] P. K. Tien, "Integrated optics and new wave phenomena in optical waveguides," *Rev. Modern Phys.*, **49**, p. 361, April 1977.

[12] T. Ikegami, "Reflectivity of Mode at Facet and Oscillation Mode in Double-Heterostructure Injection Lasers," *IEEE J. Quantum Electron.*, **QE-8**, p. 470, (1972).

[13] R. W. Davies and J. H. Walpole, "Output Coupling for Closely Confined $Pb_{1-x}Sn_xTe$ Double-Heterostructure Lasers," *IEEE J. Quantum Electron.*, **QE-12**, p. 291, May 1976.

[14] H. Kogelnik, "An Introduction to Integrated Optics," *IEEE Trans. Microwave Theory and Tech.*, **MTT-23**, p. 1, Jan. 1975.

[15] D. D. Cook and F. R. Nash, "Gain induced guiding and astigmatic output beam of GaAs lasers," *J. Appl. Phys.*, **46**, p. 1660, April 1975.

[16] T. L. Paoli, "Waveguiding in a stripe-geometry junction laser," *IEEE J. Quantum Electron.*, **QE-13**, p. 662, Aug. 1977.

[17] F. K. Reinhart, I. Hayashi, and M. B. Panish, "Mode Reflectivity and Waveguide Properties of Double-Heterostructure Injection Lasers," *J. Appl. Phys.*, **42**, p. 4466, Oct. 1971.

[18] H. C. Casey, M. B. Panish, and J. L. Merz, "Beam Divergence of the Emission from Double-Heterostructure Injection Lasers," *J. Appl. Phys.*, **44**, p. 5470, 1973.

[19] B. W. Hakki and T. L. Paoli, "Gain Spectra in GaAs Double-Heterostructure Injection Lasers," *J. Appl. Phys.*, **46**, p. 1299, March 1975.

[20] M. J. Adams, "The Cladded Parabolic-Index Profile Waveguide: Analysis and Application to Stripe-Geometry Lasers," *Opt. and Quantum Electron.*, **10**, p. 17, 1978.

[21] B. W. Hakki and F. R. Nash, "Catastrophic Failure in GaAs Double Heterostructure Injection Lasers," *J. Appl. Phys.*, **45**, p. 3907, Sept. 1974.

[22] P. A. Kirkby and G. H. B. Thompson, "Channeled substrate buried heterostructure GaAs-(AlGa)As injection lasers," *J. Appl. Phys.*, **47**, p. 4578, Oct. 1976.

[23] D. Botez and P. Zory, "Constricted double heterostructure (AlGa)As diode lasers," *Appl. Phys. Lett.*, **32**, p. 261, Feb. 1978.

[24] T. Tsukada, "GaAs-$Ga_{1-x}Al_xAs$ buried heterostructure injection lasers," *J. Appl. Phys.*, **45**, p. 4899, Nov. 1974.

[25] T. Kajimura, K. Saito, N. Shige, and R. Ito," Leaky-mode buried-heterostructure AlGaAs injection lasers," *Appl. Phys. Lett.*, **30**, p. 590, June 1977.

[26] M. Osinski, "Epstein-layer and dielectric-slab electromagnetic models of semiconductor injection lasers," *Optic and Quantum Electron.*, **9**, p. 361, Sept. 1977.

[27] D. Marcuse, "Gaussian approximation of the fundamental modes of graded-index fibers," *J. Opt. Soc. Am.*, **68**, p. 103, Jan. 1978.

[28] P. A. Kirkby and G. H. B. Thompson, "The effect of double heterostructure waveguide parameters on the far-field emission patterns of lasers," *Opto-Electron.*, **4**, p. 323, 1972.

[29] P. J. DeWaard, "Calculation of the far-field halfpower width and mirror reflection coefficients of double-heterostructure lasers," *Electron Lett.*, **11**, p. 11, 1975.

[30] K. Utaka, K. Kishino, and Y. Suematsu, "Twin-Guide Laser with Narrow Radiation Angle," *Jpn. J. Appl. Phys.*, **17**, p. 751, April 1978.

[31] G. A. Hockham, "Radiation from a solid-state laser," *Electron Lett.*, **9**, p. 389, 1973.

[32] L. Lewin, "Obliquity-factor correction to solid-state radiation patterns," *J. Appl. Phys.*, **46**, p. 2323, May 1975.

[33] J. K. Butler and J. Zoorofchi, "Radiation fields of GaAs-(AlGa)As injection lasers," *J. Quantum Electron.*, **QE-10**, p. 809, Oct. 1974.

[34] H. Kogelnik and T. Li, "Laser Beams and Resonators," *Proc. IEEE*, **54**, No. 10, p. 1312, Oct. 1966.

[35] A. Yariv, *Introduction to Optical Electronics*, Holt, Reinhart and Winston, New York, 1971.

[36] H. Kressel and M. Ettenberg, "Low-threshold double-heterojunction AlGaAs/GaAs laser diodes: Theory and experiment," *J. Appl. Phys.*, **47**, p. 3533, Aug. 1976.

[37] J. K. Butler, H. S. Sommers, Jr., and H. Kressel, "High-Order Transverse Cavity Modes in Heterojunction Diode Lasers," *Appl. Phys. Lett.*, **17**, p. 403, Nov. 1970.

[38] H. S. Sommers, Jr., private communication.

[39] W. A. Gambling, D. N. Payne, and H. Matsumura, "Mode Excitation in a Multimode Optical-Fiber Waveguide," *Electron Lett.*, **9**, p. 412, Sept. 1973.

[40] S. Nemoto and G. L. Yip, "Excitation of Self-Focusing Optical Fibre by Gaussian Beam," *Electron Lett.*, **10**, p. 150, May 1974.

[41] L. Lewin, "A Method for the Calculation of the Radiation-Pattern and Mode-Conversion Properties of a Solid-State Heterojunction Laser," *IEEE Trans. Microwave Theory and Tech.*, **MTT-23**, No. 7, p. 576, July 1975.

[42] D. Botez, "Single-Mode CW Operation of 'Double-Dovetail' Constricted DH (AlGa)As Diode Lasers," *Appl. Phys. Lett.*, **33**, p. 872, 15 Nov. 1978.

Natural Frequencies and Mode Shapes of Multi-Degrees of Freedom Systems on a Programmable Calculator

D. B. Wolfe

RCA Government Communications Systems, Camden, N.J. 08102

Abstract—The Holzer tabulation method for determining the natural frequencies of multi-degree of freedom torsional systems is relatively easy to automate on a computer or a programmable calculator. The Holzer method has been extended to translational systems consisting of masses and springs configured so that the model starts with a mass and ends with a mass. For example, the method has been used to determine the natural frequencies of freight trains with an engine in the front and a caboose in the rear. The method presented here extends the basic Holzer theory further to accommodate lumped parameter structural models. A program is developed for a programmable calculator for determining the natural frequencies and mode shapes of multi-degree of freedom systems.

1. Holzer Tabulation Method

The Holzer tabulation method was developed for determining the natural frequencies of torsional multi-degree of freedom systems. Often, mechanical systems are equated to a shaft containing several disks, as shown in Fig. 1. The elasticity of the sytem is represented by an equivalent shaft that has the ability to store potential energy. The disks represent the equivalent mass moment of inertias of the system. If disk 1 in Fig. 1 is displaced through some angle θ while disk 4 is held stationary, energy is stored in the system. When the disks are released, the system will be set into torsional vibration at its set of natural frequencies. If there

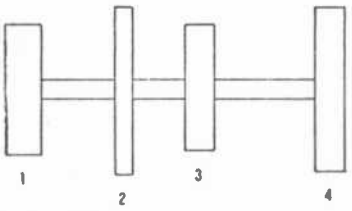

Fig. 1—Holzer Model of Torsional System.

is no damping, the system will continue to oscillate indefinitely without a forcing function.*

The Holzer tabulation method, shown in Table 1, is convenient for determining the natural frequencies (ω_n) and mode shapes. The natural frequencies are determined by assuming $\beta_1 = 1$ radian and trying various values of ω in the table. When the summation of torque is found to be zero for the system (Column 6, row N), a natural frequency is found. If the summation of torque is not zero, it is called residual torque. The residual torque can be plotted against various angular frequencies (ω) as shown in Fig. 2.

The Holzer table is used as follows:

1. Estimate or assume a value for ω
2. Calculate ω^2 from 1, above
3. Fill in Column 2 (I)
4. Fill in Column 7 (k_t)
5. For item 1 (first row)

Table 1—Holzer Tabulation Method (Assume Sample Values of ω and $\beta_1 = 1$ Radian)

1	2	3	4	5	6	7	8
Item	I	$k\omega^2$	β	$k\omega^2\beta$	$\sum_1^i k\omega^2\beta$	k_t	$\frac{1}{k_t}\sum_1^i k\omega^2\beta$
1	I_1		1			k_{t_1}	
2	I_2					k_{t_2}	
3	I_3					k_{t_3}	
:	:					:	
N	I_N						

Column 1 = Disk number
Column 2 = Mass moment of intertia, lb-in-sec^2
Column 3 = ω^2 multiplied by Column 2
Column 4 = β_i, relative angular displacement between disk i and disk 1, radians
Column 5 = Torque resulting from disk i, lb-in
Column 6 = Summation of torque, lb-in
Column 7 = Torsional spring constant k_t, in-lb/rad
Column 8 = The relative angle of twist between disks, radians θ

* For a derivation of the Holzer Method see C. R. Freberg and E. N. Kemler, *Elements of Mechanical Vibrations*, John Wiley & Sons, 1966, pp 72–8.

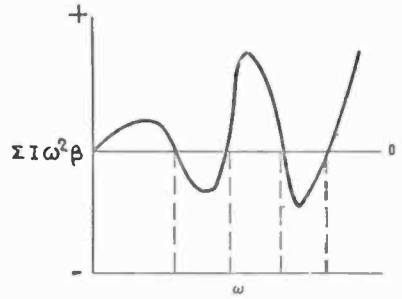

Fig. 2—Residual torque versus ω.

(a) Column 3, $I_1 \times \omega^2$
(b) Column 4, assume $\beta_1 = 1$ radian
(c) Column 5, torque (T) same as Column 3
(d) Column 6, (T) same as Column 5
(e) Column 8, (θ) Column 6_1 divided by Column 7_1

6. For item 2 (second row)
   (a) Column 3, $I_2 \times \omega^2$
   (b) Column 4, ($\beta_2 = \beta_1 - \Sigma T/k_t$) Column 4_1 − Column 8_1
   (c) Column 5, (torque) Column $3_2 \times$ Column 4_2
   (d) Column 6, (ΣT) Column 6_1 + Column 5_2
   (e) Column 8, θ Column 6_2 divided by Column 7_2
7. For item N
   (a) Column 3, $I_N \times \omega^2$
   (b) Column 4, Column 4_{N-1} − Column 8_{N-1}
   (c) Column 5, Column $3_N \times$ Column 4_N
   (d) Column 6, (Residual Torque) Column 6_{N-1} + Column 5_N]

The system frequencies are found at the zero crossings of the residual torque plot. The residual torque curve can be very steep at the zero crossing points and care must be taken to accurately determine these points.

The Holzer tabulation method can be used for translational systems by substituting mass (Wt/g) for the mass moment of inertia I, translational spring constant K in lb/in for the torsional springs constants k_t, and the relative displacement of each mass from the first mass x in inches for β_i (x_1 is assumed to be 1 inch), as shown in Table 2.

A Holzer Structural model requires the last spring to be fixed to a foundation such as the earth, as shown in Fig. 3. To set this model into oscillation, an infinite force would be required. However, since this is only a mathematical model, we will set the entire system into oscillation and then remove the forcing function, so that the entire system vibrates at its set of natural frequencies and the summation of force equals zero.

Table 2—Translational System (W = weight, g = 386 in/sec^2, ω is in Hz, and x_1 assumed to be 1 inch)

1	2	3	4	5	6	7	8
Item	W/g	$W\omega^2/g$	x	$W\omega^2x/g$	$\Sigma W\omega^2x/g$	K	$1/K\,\Sigma W\omega^2x/g$
1	M_1		1			K_1	
2	M_2					K_2	
3	M_3					K_3	
4	M_4					K_4	
⋮	⋮					⋮	
N	M_N						

We will find that if we have not selected the proper value for ω the residual force will be infinite because the force generated by the last mass as shown in Column 5_N is equal to the infinite mass multiplied by $\omega^2 x_N$. Since we are looking for a zero crossing in the residual force versus angular frequency curve, we need only determine the sign of the relative displacement x_N. When x_N is positive, the residual force will be infinite (positive), and when x_N is negative the residual force will be infinite (negative). Therefore, a change in the sign of x_N is the result of a zero crossing and is found at a natural frequency of the system. Since Column 8 is the displacement between adjacent masses, mode shapes can be developed by determining the displacements between masses at the vibration modes.

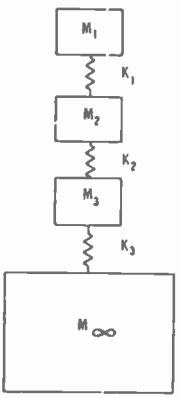

Fig. 3—Holzer structural model.

2. Use of Programmable Calculator

It is obvious that a large number of simple calculations are necessary to determine the natural frequencies and mode shapes of a multi-degree-of-freedom structural model. Since the calculations are repetitive, it is a simple job to program this problem for a computer or programmable calculator.

A program for a TI-58/59 programmable calculator has been developed. The program assumes ω to be 10 radians and runs through the Holzer tabulation calculations looking for a change in the sign of x_N. If x_N changes sign (plus to minus) between 0 and 10 radians, the program subtracts 5 radians from ω for averaging, divides by 2π, rounds the value to the nearest whole number and displays the answer as 1 Hz. If x_N does not change sign in 10 radians, the program will add 10 radians to ω and will repeat the above process. The angular frequency ω will be incremented by 10 radians until x_N changes sign. The calculator will then compute the frequency and display the results in Hz. The displacement between masses resides in the calculator memory and can be extracted for developing mode shapes.

The TI-58 contains enough memory to calculate the natural frequencies and mode shapes of a system containing up to seven masses and seven springs. The following description of the structural Holzer program is presented here to enable the reader to use it without mastering the art of programming calculators or computers. Before the details of the program are delineated, you will have to know a few things about the programmable calculator. The keyboard is shown in Fig. 4.

Besides the normal calculator functions, the following programming functions are required for this program:

LRN—(Learn)—Depressing this key allows the calculator to be programmed. Activating the key a second time will take the calculator out of the learn mode.

LBL A—(Label A)—Defines the start of this program.

STO—(Store)—Stores data in specific memory locations. For example, 10 STO 03 will store the number 10 in memory location 03.

RCL—(Recall)—Recalls the data from memory. For example, RCL 03 would bring the number 10 stored in location 03 to the display register.

SUM—(Sum)—Adds to a memory location. For example, 5 SUM 03 would add 5 to the contents of the memory at location 03.

Nop—(No Operation)—Provides spacing between program parts for later additions. Program execution simply performs no operation when this instruction is encountered. For example, the Nop function can be used to change the sign of a function by inserting a minus sign in place of the Nop. The address of the program step

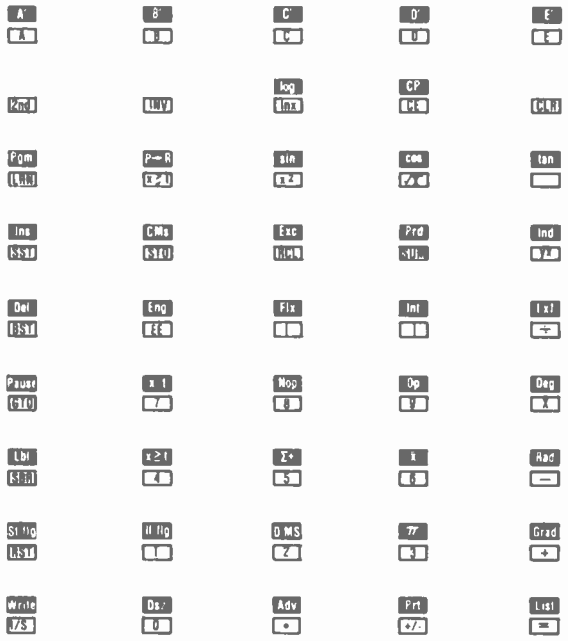

Fig. 4—Keyboard diagram for TI-58. There are two functions for most keys. The basic functions are shown as white keys with black lettering. The second functions, black rectangles with white lettering, are obtained by depressing the (2nd) key and then the key beneath the desired function.

must be remembered so that you can instruct the calculator to go to step XYZ (the address of Nop) and then press the (+/−) key.

GTO—(Go To)—This function is used to instruct the calculator to go to a specific address. It does this by moving its program pointer to the desired address. The program pointer is an internal device used by the calculator to determine which instruction it should perform next when executing a program. In the learn mode, the pointer automatically points to the next unfilled location in the program memory. When in the learn mode, depressing the (GTO) key and (A) key will tell the program pointer to go to the start of the program. If the calculator is not in the learn mode, the following key strokes, GTO, 1, 2, 5, LRN, will bring step 125 to the display register and place the calculator in the learn mode. The program can then be edited, e.g. the function of step 125 can be changed by depressing a different key.

FIX—Fixes the decimal point. For example, the following key strokes; 2nd, π, 2nd, FIX, 0 would result in the following display in this sequence; 0, 3.141592654, 3. Depressing INV, 2nd, FIX will restore 3.141592654 to the display.

INV—(Invert)—Inverts the function. For example, it was used to remove the fixed decimal in the above example.

$x \geq t$—(Test Instruction)—This is used as a conditional transfer. The test register (t) is set to zero in this program. This instruction is used to determine the change of sign of the last spring x_N. If $x_N \geq 0$ a transfer is made to the address specified. In this program, it goes to a program step which adds 10 radians to ω because the sign of x_N did not change. If x_N is less than the test register (0), it is negative and the next step in the program is followed, which is to recall the value of ω and display it in Hz.

R/S—(Run/Stop)—This function will start or stop the program. This instruction will halt the program and display the results of the last instruction.

RST—(Reset)—Resets the program pointer to step 0.

When the calculator is being programmed from the keyboard, the program step numbers are displayed each time a key is depressed. The number displayed is the program step of the next instruction to be entered.

3. Three-Mass, Three-Spring Structural Holzer Program

The details of a three-mass three-spring structural Holzer program for a TI-58/59 are described below. The following memory locations are preassigned to the variable ω, the masses, and springs of Fig. 3:

Memory Location	Contents
01	ω_1, radians/sec
02	M_1, first weight, lbs
03	M_2, second weight, lbs
04	M_3, third weight, lbs
05	K_1, first spring constant, lb/in
06	K_2, second spring constant, lb/in
07	K_3, third spring constant, lb/in

The program for the calculator is as follows.

Key Strokes	Function
LRN	Enter learn mode
2nd Lbl A	Defines start of program
RCL 1	Recalls ω
x^2	Calculate ω^2
STO 8	Stores ω^2 in memory location 08
(RCL 8 × RCL 2 ÷ 386) STO 9	Calculate Force (F) on first spring

	$(\omega^2 x_1 W_1/g)$ where x_1 is assumed to be 1 inch and stores in memory location 09
(1 − (RCL 9 ÷ RCL 5)) STO 10	Calculate x_2 by determining the displacement between M_1 and M_2, which is the force on M_1 divided by K_1 (RCL 9 ÷ RCL 5) and subtracting it from x_1 (one inch). Stores at memory location 10.
(RCL 8 × RCL 3 × RCL 10 ÷ 386) SUM 9	Calculate Σ F by computing the force on the second spring $(\omega^2 W_2 x_2/g)$ caused by M_2 and summing it to the force on the first spring.
(RCL 10 − (RCL 9 ÷ RCL 6)) STO 11	Calculate x_3 by computing the displacement between M_2 and M_3, which is the total force on the second spring divided by K_2, subtracted from x_2. Stored at memory location 11.
(RCL 8 × RCL 4 × RCL 11 ÷ 386) SUM 9	Calculate Σ F by computing the force on the third spring $(\omega^2 W_3 x_3/g)$ caused by M_3 and summing to memory location 9
(RCL 11 − (RCL 9 ÷ RCL 7))	Calculate x_N by computing the displacement between M_3 and $M\infty$ which is the total force on spring 3 divided by K_3, subtracted from x_3. A change in sign of this displacement indicates a zero crossing.
2nd Nop 2nd x ≥ t 175 (see note at end of program)	Conditional transfer if $x_3 \geq 0$, go to 175 (move the program pointer to step 175). If $x_3 \leq 0$ proceed to the next step.
((RCL 1 − 5) ÷ (2 × 2nd π))	Calculate frequency in Hz. Recall ω from memory location 01, subtract 5 radians (for averaging within the 10 radian steps) and divide by 2π.
2nd FIX O R/S	Fixes decimal place to nearest whole number, stops program and displays frequency in Hz.
LRN	Exit learn mode
GTO 175 (see note at end of program)	Moves program pointer to Location 175 (an arbitrary urused memory address)

LRN	Enter learn mode at program step 175
10SUM 1	Adds 10 radians to ω
GTO A	Moves program pointer to the start or program (step 0) to recalculate x_N with a new ω (old ω + 10 radians)
LRN	Exit learn mode, End of Program

Note: The conditional transfer (2nd Nop $x \geq$ t 175) contains a Nop instruction and a transfer address of 175. The transfer address was arbitrarily selected as program step number 175 since the program for the three-mass three-spring system is only 112 steps long not including the 6 additional program steps (1, 0, SUM, 1, GTO, A) beginning at the transfer address 175. When programming the calculator for a six or seven spring/mass system, step 175 would already have been used before getting to the conditional transfer instruction. The transfer address must be greater than the program step number of the Nop instruction. The transfer address can be any step number greater than 212 and less than 234 for the TI-58 for any system containing up to 7 springs and 7 masses. The Nop instruction is inserted in the program prior to the test instruction x ≥ t. This test instruction was used to determine the change in sign (positive to negative) of the relative displacement of the last spring, x_N, which determined the frequency of the first mode of vibration. The second mode will be found when x_N changes sign again.

In determining the frequency of the second mode the blank instruction (Nop) is replaced with (INV) so that the conditional transfer instruction is INV $x \geq t$ 175. The program will now look for x_N to change from negative to positive in determining the frequency of the second mode. The next mode is found by replacing INV with Nop.

The operation of the calculator is as follows. First place the following values in memory:

10 STO 01	start with 10 rads.
M_1 STO 02	Weight No. 1
M_2 STO 03	Weight No. 2
M_3 STO 04	Weight No. 3
k_1 STO 05	Spring No. 1
k_2 STO 06	Spring No. 2
k_3 STO 07	Spring No. 3

Depress A

Calculator will compute the 1st mode in Hz

GTO	2nd MODE
91	(LOCATION of Nop)
LRN	

INV	
LRN	
RST	
A	(SECOND MODE COMPUTED)
GTO	3rd MODE
91	
LRN	
2nd	
Nop	
LRN	
RST	
A	(THIRD MODE COMPUTED)

The mode shapes can be developed by determining the displacements between the masses. The displacement between masses is found in Column 8 of the Holzer table $K^{-1}\,\Sigma W\omega^2 x/g$. Note that $\Sigma W\omega^2 x/g$ is always stored in memory location 9 for each mass and the displacements can be found by dividing it by the springs constant K_i. Looking at the program we find that RCL 10 = (1 − (RCL 9 ÷ RCL 5)) for mass 1 where memory location 9 contained $\Sigma_1^1 W^2 x$ at the time of the calculation and memory location 5 contains K_1. Since the displacement between M_1 and $M_2(\delta_{1-2})$ is equal to $K^{-1}\,\Sigma_1^1 W\omega^2 x$, we obtain RCL 10 = $(1 - \delta_{1-2})$ and $\delta_{1-2} = 1 -$ RCL 10.

The displacements might be very small; therefore, the calculator must be taken out of its fixed decimal place mode. After the calculator displays the frequency of the first mode of vibration, the following keys are depressed:

INV, 2nd, FIX

1 − RCL 10 =

The relative displacement between mass 1 and mass 2 will be displayed on the calculator.

The displacement between masses 2 and 3 can be determined in a similar manner.

RCL 11 = (RCL 10 − (RCL 9 ÷ RCL 6))

δ_{2-3} = RCL 9 ÷ RCL 6

where RCL 9 = $\sum_1^2 W\omega x/g$

RCL 6 = K_2

δ_{2-3} = RCL 10 − RCL 11

The displacement between masses 3 and ∞ is determined by:

$\delta_{3-\infty}$ = RCL 9 ÷ RCL 7

where RCL 9 = $\sum_{1}^{3} W\omega^2 x/g$

RCL 7 = K_3

The displacements between masses at the higher modes are obtained by following the procedure outlined above remembering always to remove the calculator from the fixed decimal mode.

The displacements between masses in each mode are normalized so that the maximum displacement between adjacent masses (δ_{1-2}, δ_{2-3}, $\delta_{3-\infty}$) is a unit deflection. This is accomplished by dividing all displacements by the largest displacement. The displacements may be plotted to delineate the mode shape.

4. Example

Fig. 5 shows a steel rack with three shelves supporting rigid masses. The rack structure is welded so that the shelves and top are fixed to the four columns. The base of the assembly is firmly fixed to a vibration table. The problem is to find the natural frequencies and mode shapes that would be found if the table were to oscillate in the x direction as shown on the figure.

The Holzer lumped parameter structural model was shown earlier in Fig. 3. The spring constants K represent the compliance of the structure between the masses. Values of the masses are shown in Fig. 5. The rack weight apportioned to each mass is 0.24 the column weight plus the shelf weight, or approximately 10 lbs/mass. Therefore, $M_1 = 110$, $M_2 = 160$, and $M_3 = 210$ lbs.

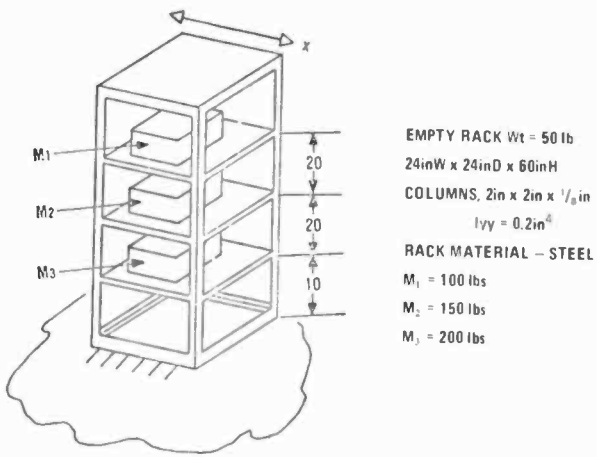

Fig. 5—Rack assembly used for example.

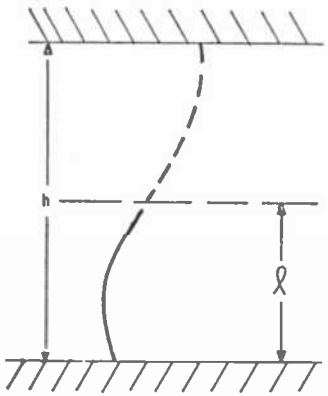

Fig. 6—Deflection curve.

The spring constants K are derived from a static analysis of the structure. If the rack was deflected in the x direction, the columns between the shelves would bend in an "s" shape with the ends perpendicular to the shelves. The deflection curve of the columns looks like two cantilever beams in series, as shown in Fig. 6, where h is the distance between shelves ($h = 2l$). The spring constant of a cantilever beam with length l is

$$K = \frac{3EI}{l^3}$$

$$= \frac{3EI}{(h/2)^3} \text{ per beam.}$$

There are 8 beams per shelf, and springs in series add like capacitors in series:

$$K_{column} = \frac{1}{\frac{1}{K_{beam_1}} + \frac{1}{K_{beam_2}}} = \frac{1}{\frac{1}{24EI/h^3} + \frac{1}{24EI/h^3}} = 12\,EI/h^3$$

$$K_{4c} = 48\,EI/h^3 \text{ (per shelf)}$$

$$K = \frac{48EI}{h^3}$$

$$K_1 = K_2 = \frac{48(30 \times 10^6)(0.2)}{(20)^3} = 36{,}000 \text{ lb/in}$$

$$K_3 = \frac{48(30 \times 10^6)(0.2)}{(10)^3}$$

$$K_3 = 288{,}000 \text{ lb/in} = 288{,}000 \text{ lb/in.}$$

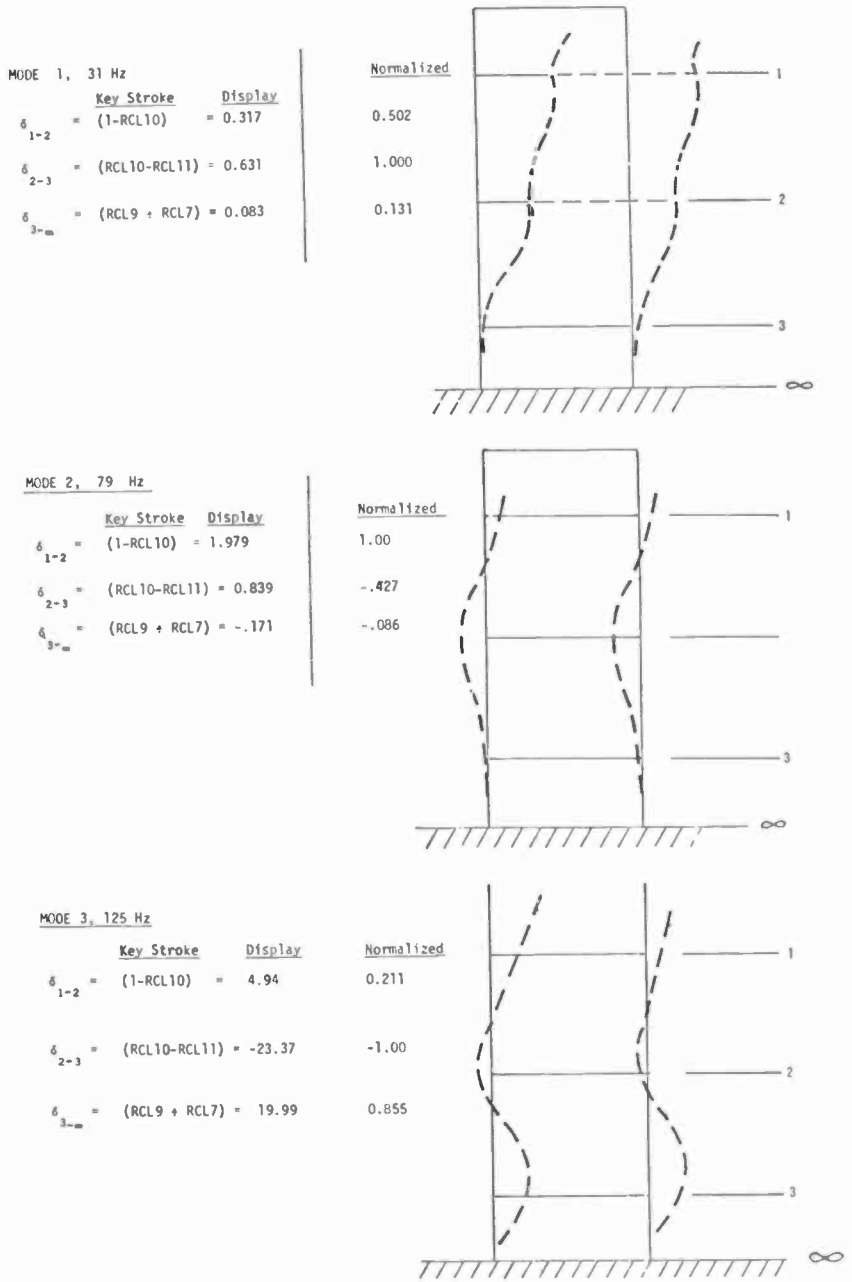

Fig. 7—Deflection curve plotted (a) for mode 1, 31 Hz, (b) for mode 2, 79 Hz, and (c) for mode 3, 125 Hz.

Once the calculator is programmed, the data is loaded as follows:

	Key Strokes	
ω	10	STO 01
M1	110	STO 02
M2	160	STO 03
M3	210	STO 04
K1	36,000	STO 05
K2	36,000	STO 06
K3	288,000	STO 07

The natural frequencies are now computed with the following sequence:

Key Stroke	Display	
A	31Hz	
		1st mode
GTO		
91		
LRN		
INV		
LRN		
RST		
A	79 Hz	2nd mode
GTO		
91		
LRN		
2nd		
Nop		
LRN		
RST		
A	125 Hz	3rd mode

Before the mode shapes are determined, the calculator must be taken out of the whole integer mode with the following key strokes: INV, 2nd, and FIX. The mode shapes are determined by computing the deflections between masses, normalizing to unit deflection, and plotting, as shown in Fig. 7(a–c).

Application of Finite Element Methods

The following papers in this issue of RCA Review were selected from among several presented at a Finite Element Symposium held at RCA Laboratories on March 13–14, 1978. This Symposium featured papers on both theory and application of finite element methods, and the papers presented here illustrate the diverse applicability of the method. Finite element computer methods have been shown to be a powerful tool useful in the solution of complex engineering problems for which closed form, text-book solutions do not exist, either because of a complex shape or because of complex conditions of restraint (i.e. boundary conditions). Some applications of the finite element method investigated at RCA include the stress distribution arising from pressure or thermal loads in consumer products, spacecraft, and semiconductor wafers; natural frequencies of vibration in broadcast towers; heat flow in electronic components; and electric fields in cathode ray tubes. Examples of applications of finite element analyses that have been investigated elsewhere include fluid flow and transport, impact, creep, soil-structure interactions, earthquake simulation, crack analysis, electricity, and magnetism.

In the finite element method, a mathematical model is made by dividing the continuous structure or fluid into 1-, 2-, or 3-dimensional discrete blocks (finite elements) for which mathematical formulas describing their behavior have been derived. The mathematical model for the behavior of the aggregate structure is then the sum of the properties of the individual blocks and their interactions. The individual finite elements are described spacially by the ordering and Cartesian coordinates of their corners. The appropriate boundary conditions, material properties, and loads must also be specified. Here, the loads applied to the finite element model of the structure may be a thermal, pressure, gravity, electric, static, or time-varying force, or a combination of these. The solution is then calculated from the input data for the mathematical description and properties of the structure using either a commercial (ANSYS, MARC, STARDYNE, NASTRAN, etc.) or a proprietary computer software program (such as the RCA Corporation's TV Tower, DYNA Structural Dynamics, or POT3D Electron Optics Program). The

outputs of these programs are both tabular and graphical representations of the resulting solutions.

The power of the finite element method is that it permits the *a priori* prediction of the response of a complex structure to a complex load from a descriptive blueprint of the geometry of the structure and its physical properties. In this way, many design changes can be made and the effect of these design changes evaluated before molds are produced or full scale construction begun.

The series of papers included here discusses finite-element-method theory and solutions of problems dealing with spacecraft, television picture tubes, and high power tubes for fusion energy research using static, dynamic, and thermal analyses.

The paper by Sheffler gives a brief overview of the theory and utilization of the finite element method. For a more complete description of general finite element theory, the texts of Zienkiewicz[1] or Gallagher[2] can be consulted. The application of these methods to the design and analysis of spacecraft is described in the paper by Niederoest. Here the vibrational modes during launch and flight are calculated and graphically presented. It should be pointed out that the finite element representation of a spacecraft sitting atop a launch missile is not a strict geometrical description of this very complex structure, but rather is a "bare-bones" representation. In this case, parts of the structure are lumped together as equivalent masses, thereby reducing considerably both the number of elements required to describe the structure and the attendant computer solution costs.

Professor Pian describes the use of variational methods and hybrid elements to achieve better accuracy in the evaluation of stresses. These procedures are particularly effective where, for example, Poisson's ratio approaches 0.4999, as for an incompressible material, or in the analysis of a crack. A further advantage of these methods is a greatly reduced number of elements needed to describe the crack. But, here a somewhat larger computing effort is required because of a larger number of unknown quantities.

In the paper on the analysis of television picture tubes, three dimensional elements are assembled to form a finite element model that more closely describes the geometry of the actual structure. Here, though, only one-quarter of the tube is modeled to reduce the computer costs. This model is then adjusted or altered slightly to determine the effect of geometrical differences on atmospheric-pressure-induced stresses, the effect of implosion-protection safety bands, and thermal-processing-

[1] O. C. Zienkiewicz, *The Finite Element Method*, 3rd Ed., McGraw-Hill, London (1977).

[2] R. H. Gallagher, *Finite Element Analysis Fundamentals*, Prentice-Hall, Englewood Cliffs, New Jersey (1975).

induced stresses. Further, it is possible with the finite element method to calculate the value of stresses in all locations with a completeness that is difficult to accomplish experimentally.

The final paper, by R. C. Bauder, describes how heat flow and the accompanying thermally-induced stresses in 25-megawatt vacuum-power-tube anodes and neutral beam absorbers have been analyzed to optimize the design of these devices. These items will be an integral part of the fusion energy research facilities of the Princeton Plasma Physics Laboratory. In this approach, the hydrogen plasma must be ignited and maintained at very high temperatures (approximately 100 million degrees Centigrade) for several seconds for a useful reaction to occur. The neutral beam source used to initiate the reaction must be switched at 200 kilovolts and at high current levels using the large vacuum switch tube. The non-neutralized part of the beam is diverted magnetically and must be absorbed in a heat dissipating device. Such large and complex structures would be difficult or virtually impossible to analyze accurately if the finite element method were not employed.

It is a pleasure to acknowledge the close collaboration of W. Metzger and A. Sheffler, R. Bauder and R. Pschunder in the preparations for the symposium at which these papers were delivered.

Ronald E. Enstrom
Symposium Chairman
RCA Laboratories
Princeton, N.J.

An Overview of Finite Element Methods and Their Application to Engineering Problems

A. Sheffler

RCA Astro-Electronics, Princeton, N.J. 08540

Abstract—This paper gives a brief discussion of the fundamental theory of finite element methods, from which the strengths and weaknesses of the method can be seen. The discussion is presented from the point of view of structural analysis, where the method was first developed and is so widely used today. Subsequent papers describe applications of the method in other areas.

Introduction

In recent years, the finite element method has developed into one of the most powerful analytical tools available to the research and design engineer. As such, its applications have grown in direct proportion to the growth of digital computer systems. The matrix equations used in the finite element method take full advantage of the computer's ability to handle large numerical solutions with ease and low cost. The wide range of applications result from the basic simplicity and versatility of the method. Basically, the finite element method can be viewed as a set of building blocks, or elements, that are joined to form a model of the physical system. This paper presents an short overview of this method from the generation of the elements to the assembly of the system and its application to specific problems.

The finite element method is presented here from the point of view of the structural analyst. This is appropriate since the method was primarly developed to aid in structural design and analysis in the aerospace industry. For example, the initial work by Turner et al[1] and by Argyus[2]

was used in the design of complex aircraft wing structures, while Alley and Gerringer[3] developed methods for spacecraft launch vehicle designs. Since this development, the finite element method has been applied to fluid dynamics problems, pollution control studies, and conductive heat transfer. For simplicity and clarity, however, this discussion will be limited to applications in structural mechanics.

Technical Discussion

In the solution of a structural analysis problem, such as the load/deflections case, the analyst has the choice of solving the equilibrium equations by exact analytical solutions or by using various numerical techniques. In general, the numerical techniques can provide more general solutions than the closed-form analytical solutions. With numerical techniques, computer solutions require an organized, systematic way of handling the analysis. This leads to the use of a system of nodes, as in Fig. 1, with nodal numbering systems and a system of meshes to connect these nodes in specific ways. The employment of a numerical mesh, however, does not necessarily imply a finite element solution. The same mesh technique may be used for the direct numerical solution of the differential equations. For example, the finite difference technique with its nodes and meshes is widely used in heat transfer analysis to solve the system equilibrium equations. The distinguishing characteristic of

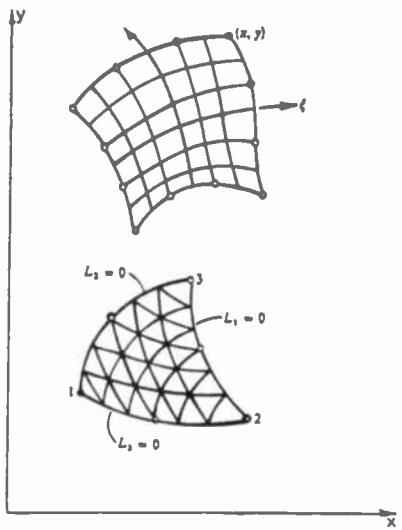

Fig. 1—System of meshes and nodes used in loads/deflections problem.

the finite element method is that is uses an element that is itself in total equilibrium. Thus, you have an element, or even a library of elements, that can be assembled to form a system that is in equilibrium. In this system, the nodal force and displacement are related by $F = k\Delta$, where F is the force, Δ is the displacement, and k is the stiffness. Accordingly, the matrix of simultaneous equations can be solved for either the forces or the displacement.

The finite element method can be separated into two general categories. First there is the force method which has the capability of generating the flexibility matrix of a system. Unfortunately, the force method does not lend itself to easy application using digital computers because the data preparation required is quite extensive. In this method, each problem has to be unique. In particular, if the problem includes a statically indeterminate structure, the analyst needs to be careful when chosing the determinate and indeterminate degrees of freedom. In this situation, it is possible (or probable) that the flexibility matrix generated will be singular. For example, when the force method was initially used in aircraft structural analysis, it was common to have teams of analysts who were specialists in its use. A fuselage or wing structure, which is highly redundant, required careful selection of determinate and indeterminate degrees of freedom in a particular analysis. The entire specialty group was established to define the computer input for the force method.

In contrast to the force method, the displacement method of finite element analysis generates the stiffness matrix of the system. It has been shown[2] that a one-to-one analogy exists between the stiffness method and the force method. And not surprisingly, it has the same types of problems, i.e., it is not necessarily directly programmable for all situations.

A breakthrough in the use of finite element methods came with the development of the direct stiffness method.[1,4] This method has become so powerful that today when we refer to finite element methods, we are generally talking about the direct stiffness method. With this method it is possible to generate a library of elements that can, in turn, be used to generate the stiffness matrix of the entire system without regard to whether it is statically determinate or statically indeterminate. Put another way, it is possible to program the entire structural system by following a regular pattern in assembling the element stiffness matrices. The real advantage of the method is its complete independence of the boundary conditions.

In general, the finite element method (specifically, the direct stiffness method) can be defined as a process or a series of steps used to generate an element or several elements and to combine these elements to form

a system. Numerically, this results in a system of linear equations in matrix form. The unique feature of the finite element method is that each element has a finite number of unknowns. This means the strain energy (or everything that is going on in that element) can be obtained if one knows the deflections at the node points. This finite set of unknowns (the nodal deflections) is what sets the method apart as being a "finite element" system.

As shown in Fig. 2, several types of compatible elements can be combined from the finite element computer libraries available today. You can put together, for example, beam elements, triangular plates, and quad plates, and build up a system that represents the actual structure. No matter how complicated the system, each of the elements follows the simple equation

$$\{p_e\} = \{k_e\}\{u_e\}$$

where $\{p_e\}$ is the nodal forces on the element, $\{k_e\}$ is the element stiffness matrix, and $\{u_e\}$ represents nodal deflection. This equation simply reminds us that the load has to be equal to the spring rate times the deflection. Thus one is always dealing with a simple linear equation in matrix form.

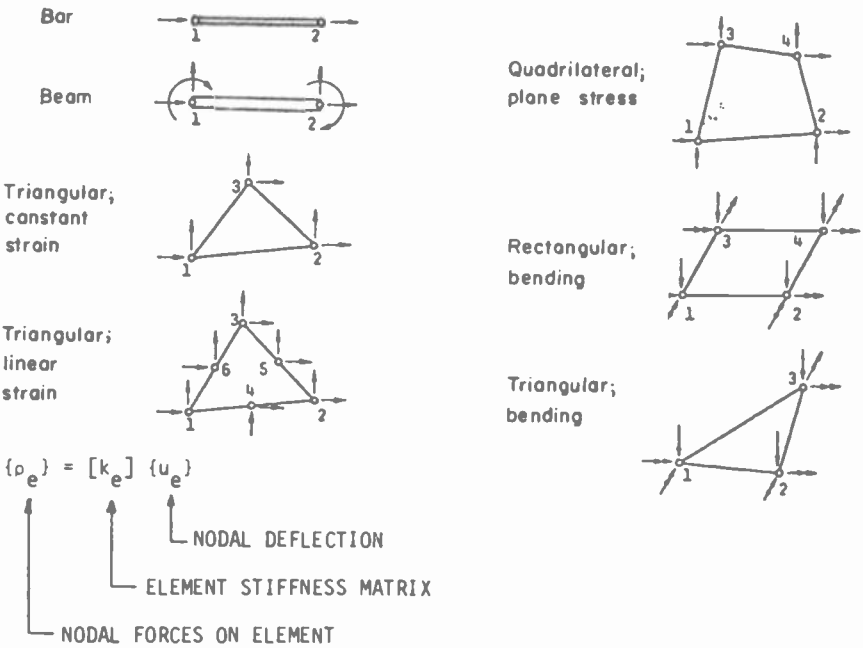

Fig. 2—Compatible elements used in finite element method. These elements are available in standard computer programs.

The Finite Element Process

Fig. 3 summarizes the finite element method as a process, or series of analytical steps. The left side of the figure shows the steps the user has to control, i.e., where engineering judgement is involved. The right side of the figure shows the programmed computer operations. The first step, therefore, is to select the nodes and the elements. The small sketches in Fig. 3 illustrate a typical system in three-dimensional coordinates. The material properties are chosen according to the type of material being used. Isotropic, orthotropic, or anisotropic materials all follow the same pattern, which again illustrates the wide application of this method.

Before proceeding through the analysis, it is best to consider what the end product will be and to compare that result with what we need from the analysis. Unless proper judgement is used in defining a model, costly re-work may result. For example, if known point loads exist, it is desirable to have a locally refined grid spacing and to use the proper types of element. In this case, good judgement and many iterations in this first loop are required. It is extremely costly and time-consuming to have to go back and redefine the model. Failure to spend the time necessary to

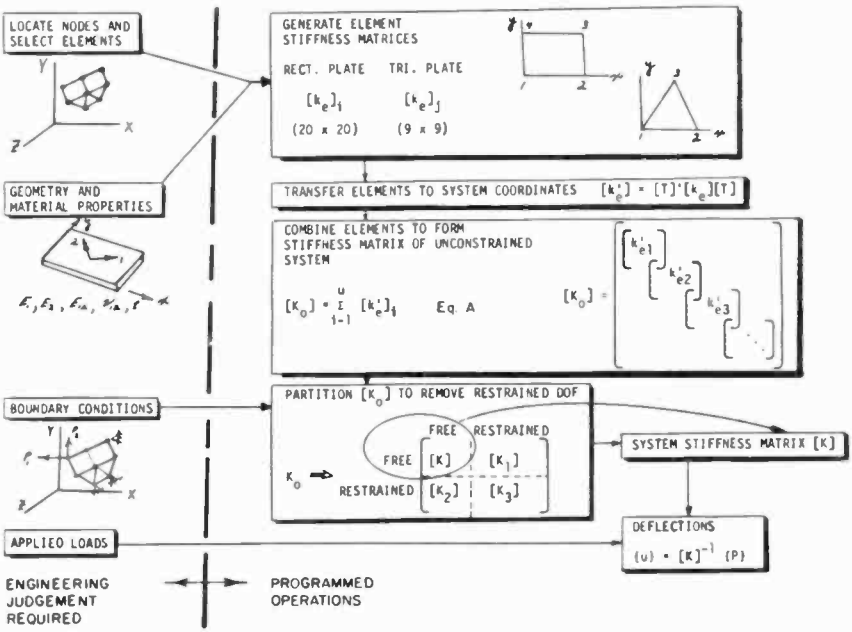

Fig. 3—Finite element analysis sequence. Left side of the figure shows steps the user has to control; right side shows programmed computer operations.

generate an adequate model is an error often made by new users, and its importance cannot be stressed too strongly.

The finite element process begins with the generation of each of the elements, whether they are rectangular or triangular plate elements, as shown in the first step of Fig. 3, or any of the other elements available today. A subtle point to keep in mind, however, is that each of these elements is generated in its own local coordinate system. To be useful, the element stiffness matrix has to be transferred into the system coordinates (Fig. 3, step 2). This requires a coordinate transformation and a nodal renumbering operation on the element. This operation is straight-forward, but is must not be overlooked when interpreting the results. When the element stiffness matrix is transformed into the system coordinates format, the elements are summed to form a system. Eq. [A] in Fig. 3 is an oversimplified example of this operation. As can be seen, the stiffness matrices for each of the elements are summed according to the degrees of freedom of that element. The task is not an easy one because it involves keeping track of all the degrees of freedom of that element in the system coordinates. The illustration shown in Fig. 3 is greatly simplified, as previously stated, but it does show that the summation occurs where the stiffness matrices of each element overlap. As these terms are added, they form a stiffness matrix for the system. Eq. A in Fig. 3 illustrates the stiffness matrix for an unrestrained system.

The final step in the process is the imposition of boundary conditions on the structure. Boundary conditions would be applied if certain points are restrained from having any displacement or rotation. In the direct stiffness method, statically determinate and statically indeterminate structures produce no difference in the analysis. The system stiffness matrix is simply partitioned according to the restrained degrees of freedom and the free degrees of freedom. These free degrees of freedom then form the stiffness matrix for the constrained system. Once this system stiffness matrix has been generated, its inverse can be determined, as illustrated in Fig. 3, and combined with a given set of loads to produce the nodal deflections in the system model.

Commercial Computer Programs Available to Users

There are several analysis programs, such as NASTRAN, STARDYNE, and STRUDL, that follow the type of sequence illustrated in Fig. 3. This sequence involves going from the element stiffness matrices to a system stiffness matrix, and finally to the application of boundary conditions. Typically, these operations are done in the active core of the computer.

Programs such as ANSYS, on the other hand, utilize an approach

called a wavefront solution. The approach is the same as shown in Fig. 3, except that the specified boundary conditions and a Gaussian elimination technique are used to eliminate the restrained degrees of freedom on a one-for-one basis. As the program generates the stiffness matrix for each element, the boundary conditions are applied, and the reduced element is stored in external storage. These programs obviously require different formulations. In NASTRAN or STARDYNE, for example, you would want to have a nodal numbering system that results in a minimum bandwidth on the stiffness matrix, as illustrated in Fig. 3. These types of programs take advantage of the small bandwidth in the matrix inversion techniques. With ANSYS, on the other hand, the user would want to be careful of the element numbering system (rather than the nodal numbering system) so that the Gaussian elimination, or wavefront solution, is minimized. The end product from any of these programs is a single stiffness matrix for the entire system. With this stiffness matrix, the analyst can determine the structural deflections, load distributions, stresses, and even natural frequencies and mode shapes.

The Element Stiffness Matrix

The heart of the finite element method is the generation of the stiffness matrix for a single element. As discussed in the literature,[5,6] there are several ways of generating these element stiffness matrices. Fig. 4 shows the four basic approaches. The unit displacement, Fig. 4(a), is based on defining the loads necessary to produce a single unit degree of freedom. The forces required to produce this unit deflection produce the stiffness

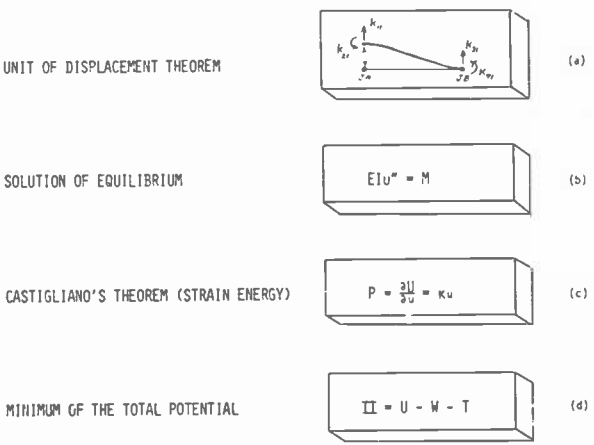

Fig. 4—Approaches for generating the element stiffness matrix.

matrix directly. By proceeding through all the degrees of freedom on the element, the entire element stiffness matrix is generated. The second method, Fig. 4(b), involves the solution of the equilibrium equations and leads to the same direct stiffness approach.

Castagliano's theorem, Fig. 4(c), is a strain energy method that has a broad application to the development of an element stiffness matrix. An even more general approach that is widely used is the Minimum of the Total Potential, Fig. 4(d). Here, the total potential is a function of the strain energy, the work of the external loads, and the kinematic energy. This method is the one most widely used. In general, the user does not generate the elements, but we need to know how they work and their limitations. For clarity, I have chosen in Fig. 5 to consider a static analysis where the total potential is a function of only the strain energy and the external work done by the applied loads. The primary drawback of this method is in accurately determining the strain energy. Just as in the commonly used Raleigh–Ritz method, a deformed shape function must be assumed in order to obtain an expression for the strain energy. Typical shape functions are the polynomials given in Fig. 5. Also, various osculating polynomials, such as Hermitian polynomials, have been used with good results.[7,8] This is an approximation, however, just as in all strain energy work. The finite element techniques based on these methods, therefore, are only as good as the shape functions that are used.

As in basic mechanics, if the shape function matches the actual system perfectly, then the calculated strain energy will be accurate. If there is any mismatch on either side of the true deflection patterns, then some higher strain energy exists in the math model. This higher strain energy implies that you have a stiffer system, which results in smaller deflections for given loads. Finite element techniques will always lead to stiffer

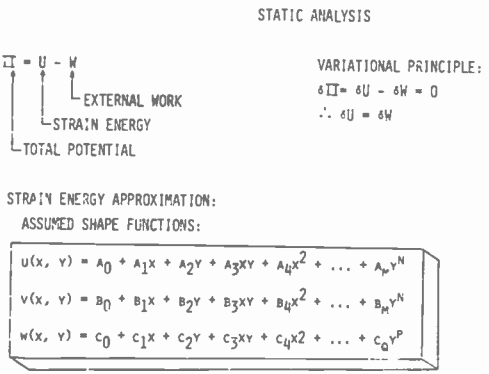

Fig. 5—Generation of element stiffness matrix using minimum of total potential approach (static analysis).

systems if they are based on a strain energy approach. Therefore, since the method approaches the "true" solution from the stiff side, it becomes important to know how good these shape functions are. Fortunately, over the years, these techniques have been developed into a highly reliable method. All of the commercially available programs can be relied upon as being accurate, dependable systems.

Stress Analysis and the Element Shape Function

Let us now recall that the finite element method, as it is used in a static analysis, has as its basic output the calculation of the deflections. If stresses are to be determined, it is necessary to go back to the element stiffness matrix. This depends, once again, on the element shape functions. For example, if it is necessary to determine stresses due to the applied loads in a particular element in the model, the first calculation is of the deflections of the system. Once the distortions of the element are determined, the stresses are calculated using the element stiffness matrix. Thus, the stress analysis is highly dependent on the accuracy of the element shape function. Isoparametric elements are higher order and lead to stresses closer to the actual values. It is best to be conservative at this point. One should place a large number of elements in any area where rapidly changing stress patterns occur and gradually increase the element size as the stress gradient decreases. This procedure requires experience and judgment. Further, choose a high order element where possible. Frequently, a smaller number of isoparametric elements[6] can give a better solution than a larger number of lower order elements.

Dynamic Analysis Based on Finite Element Techniques

In terms of dynamic analysis, the finite element method produces a powerful tool for the modal analysis of a system. Modal analysis produces the frequencies, mode shapes, modal forces, and the generalized mass of the dynamic system. The main part of this eigenvalue process is in determining the frequencies and mode shapes derived from the stiffness and mass matrices. With these modal characteristics, the harmonic, random, acoustic, and transient response analysis can be carried out by a number of normal mode methods. These normal mode methods are built into the commercially available programs, or the modal characteristics can be used in other special purpose dynamic analysis programs. In either case, the finite element model is the primary tool for generating the modal properties. This model produces both the stiffness and mass matrices and must be able to produce accurate mode shapes over a wide frequency range. This is especially true when calculating loads and

stresses where a significant number of modes must be superimposed for accurate results. So, once again, in setting up a dynamic model, good judgement and planning is required to obtain accurate results.

Summary

The broad application of finite element methods in structural mechanics includes the analysis of static deflections, stress distributions, as well as modal and dynamic responses analyses. This full range of analytical tools stems from the development of relatively few analytical building blocks, called finite elements. When assembled to model the actual structure, these elements can readily account for unusual geometry, loading, and boundary conditions. They can provide sufficient accuracy to obtain low cost design verification and test predictions. As a result, the finite element technique has become firmly established as an analytical tool to aid in the design process.

References

[1] M. J. Turner, R. W. Clough, H. C. Martin, and L. J. Topp, "Stiffness and Deflection Analysis of Complex Structures," *J. Aeronautical Science*, 23, No. 9, Sept. 1956.

[2] J. H. Argyus and S. Kelsey, *Energy Theorems and Structural Analysis*, Butterworth and Co., Ltd., London (1960).

[3] V. L. Alley and A. H. Gerringer, "A Matrix Method for the Determination of the Natural Vibrations of Free-Free Unsymmetrical Beams with Application to Launch Vehicles," NASA TN-D-1247, 1962.

[4] R. J. Melash, "Basis for Derivation of Matrices for the Direct Stiffness Method," *AIAA Journal*, 1, No. 7, 1963.

[5] J. S. Przemieniecki, *Theory of Matrix Structural Analysis*, McGraw-Hill Book Co., Inc., New York, (1968).

[6] O. C. Zienkiewicz, *The Finite Element Method in Engineering Science*, McGraw-Hill Publishing Co., Ltd., London (1971).

[7] F. D. Bogner, R. L. Fox, and L. A. Schmit, "The Generation of Inter-Element-Compatible Stiffness and Mass Matrices by the Use of Interpolation Formulas," *Matrix Methods in Structural Mechanics*, Proc. Conf. Wright-Patterson Air Force Base, Ohio, AFFDL-TR-66-80, Nov. 1966.

[8] A. W. Sheffler, *A Finite Element Method for the Analysis of Anisotropic Laminated Plates*, Ph.D. Dissertation, West Virginia University (1973).

Finite Element Methods in Spacecraft Dynamic Analysis

G. Niederoest

RCA Astro-Electronics, Princeton, N.J. 08540

Abstract—A spacecraft dynamic analysis is required for the accurate prediction of the spacecraft dynamic characteristics such as modal frequencies and responses and their effect on the overall launch vehicle. This paper presents the techniques used at the RCA Space Center as applied to the TIROS-N meterorological spacecraft. The technique consists of a loads generating cycle and a loads verification cycle. The loads generating cycle involves the development of an accurate finite element model which is then used to determine the spacecraft responses due to the launch environment loads. The load verification cycle is used to verify that the loads generated for the launch environment and for which the spacecraft structure has been designed are adequate and, therefore, proves structural integrity.

Introduction

Several years ago, a typical spacecraft dynamic analysis consisted of attempting to reduce the stiffness and mass characteristics of a spacecraft into a few-degrees-of-freedom system and solving for the first modal frequencies. Dynamic responses of discrete points on the spacecraft were more difficult to obtain and required the use of a mechanical test model. Since that time, however, a revolution in computer technology has allowed mathematical modeling of multi-degree-of-freedom systems to become a quick and accurate method in solving for modal and dynamic responses of complex structures. Mathematical modeling by the finite element technique has become a required practice in many industries, in particular the aerospace industry, where it is of prime importance in

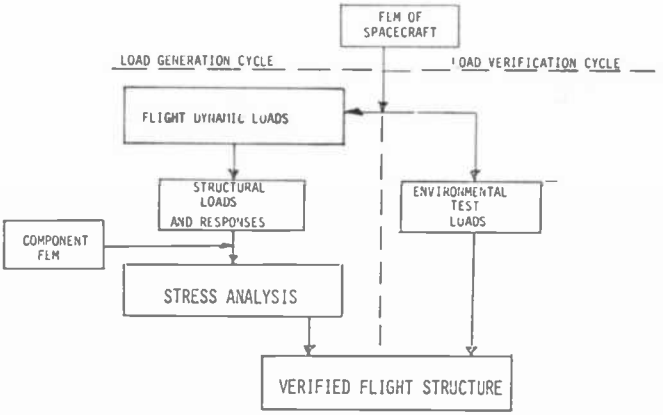

Fig. 1—Spacecraft dynamic analysis.

understanding the dynamic characteristics of a spacecraft and its effect on the overall launch vehicle. It is used to predict the flight level loads in the structure, perform the actual stress analysis of each structural component (i.e., equipment and solar panels), and, in addition, allows the tailoring of environmental test loads so that actual flight occurrences are simulated during the testing phase without overstressing the structure.

The flow diagram in Fig. 1 is that of a typical spacecraft dynamic analysis. The analysis basically consists of two cycles; (1) the loads generating cycle in which the structural loads that are predicted to occur during the space vehicle's lifetime are analyzed and (2) the loads verification cycle which is used to verify structural integrity.

2. Loads Generating Cycle

Fig. 2 shows typical flight dynamic loads that the spacecraft must be designed to withstand. These loads occur very early in the launch sequence, and this, therefore, is the most critical time for the space vehicle. The environmental test loads, also shown in Fig. 2, are used in the loads verification cycle of the spacecraft. The structural loads simulated by the environmental test loads are generally much higher than those that occur during actual flight, though low enough to preclude any structural failure.

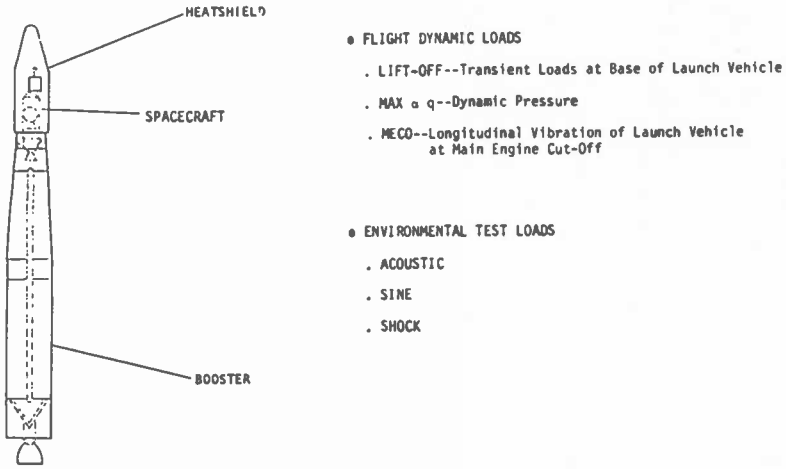

Fig. 2—Dynamic analysis design loads.

2.1 Model Definition

The accuracy of any dynamic analysis is directly related to the quality of the finite element model and is, therefore, the prime factor in obtaining satisfactory results. The three basic considerations in the synthesis of a finite element model are stiffness distribution, mass distribution, and boundary conditions. Neglecting any of these considerations will result in a model that is not dynamically similar to the actual structure. Therefore, a detailed evaluation of all major structural components must be made to determine the degree of sophistication required to accurately model each component. This should include all joints, mass and stiffness eccentricities, indeterminate load paths, and any forseeable nonlinearities that might exist in the structure. In addition, the mass and inertia points that will yield the closest approximation to the actual hardware layout must be determined. This process includes everything from simple point masses to complex mass/spring models to accurately simulate events such as launch-vehicle fuel sloshing.

Cost is also of concern to any analysis. Since computing costs are directly related to the degree of detail of a finite element model, the desire to obtain the ultimate model must be tempered by an equally strong need to reduce the analysis cost by simplification. The trick is to generate a finite element model that is detailed enough to give acceptable results but that is not prohibitively costly to run. Two approaches are possible: (1) use a small number of large-size elements to accurately model the geometry or (2) use equivalent masses and stiffnesses that describe mechanical behavior of the object but that do not necessarily bear a close

physical resemblance to the structure. In the work described here, the second approach was taken to reduce the cost while achieving an accurate solution. Substructuring is an important tool for this purpose. An important benefit of this approach is reduced throughput time so that modeling changes and reruns can be made in a short period of time.

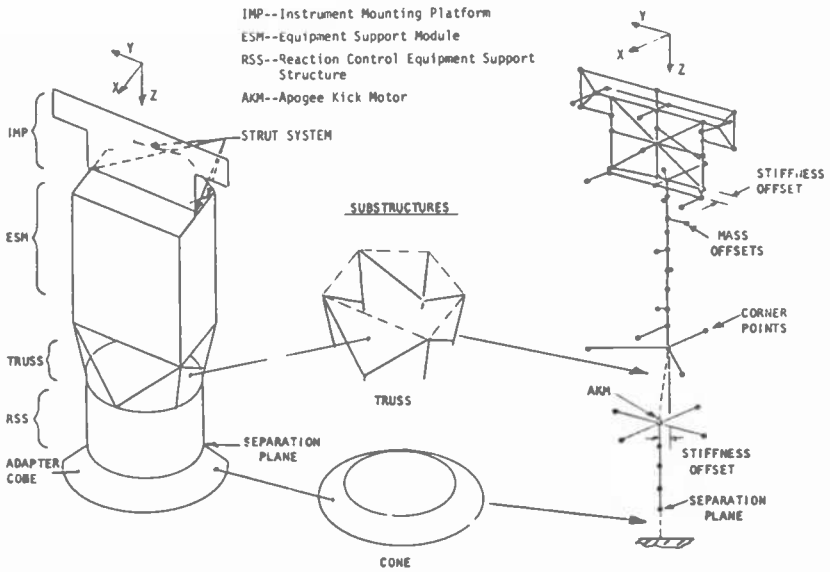

Fig. 3—TIROS-N spacecraft dynamic finite element model.

This type of finite element model is illustrated in Fig. 3. The spacecraft depicted is the NASA funded, RCA built, TIROS-N meteorological spacecraft. The figure shows the prime structrual components of the spacecraft and how each is modeled. The finite element model consists of the Instrument Mounting Platform (IMP), an Equipment Support Module (ESM) made of honeycomb panels attached to a pentagonal shaped frame, a space truss that attaches the ESM to the Reaction Control Equipment Support Structure (RSS), the cylindrical Reaction Control Equipment Support Structure, and, finally, a conical adapter. The cone adapts the spacecraft to the launch vehicle.

The IMP is modeled as a series of beams with equivalent bending and shear properties and mass distribution to accurately model the first two bending modes of the panel (determined by previous analysis). The IMP is attached to the ESM by means of a statically determinant strut system which is represented by beams. The stiffness properties of the ESM and RSS are modeled as beams with offset masses to account for the non-

symmetric mass distribution on these components. Additionally, note that the neutral axes of the RSS and ESM are offset from each other, similar to the actual hardware. This is also the case with the IMP and ESM. Simple beam theory, however, cannot be used to model the complicated deflection characteristics of the truss and conical adapter. Fig. 4 shows what occurs to the cone by the application of a shear and moment

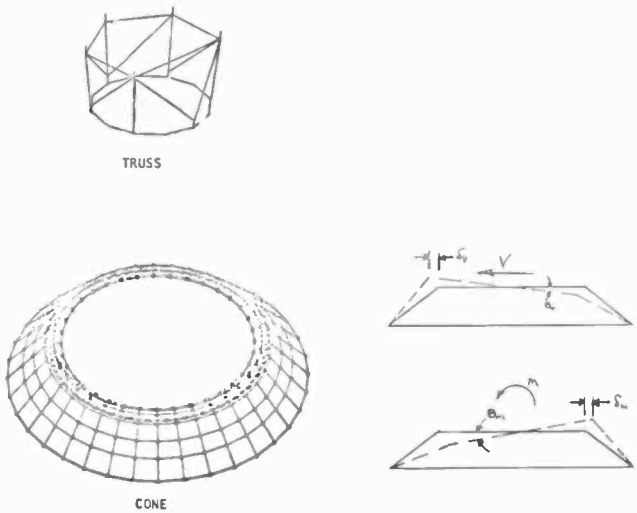

Fig. 4—Truss/cone substructures. These substructures cannot be accurately modeled with a simple beam. As shown for the cone, the rotation due to the shear load and the deflection due to the applied moment are opposite to that predicted by simple beam theory.

load. The rotation due to the shear load and the deflection due to the applied moment are opposite to that predicted by simple beam theory. This phenomenon is more complex for the truss due to its nonsymmetrical stiffness characteristics. Therefore, these items are modeled as substructures with reduced stiffness matrices from a detailed component finite element model for convenient input to the spacecraft model. Joint compliance of riveted, bolted, or Marmon clamp joints are represented by zero length springs. These joints can have a significant effect on the spacecraft dynamics and, therefore, must be considered in order to obtain reasonable results from the finite element mode.

2.2 Modal Analysis

The next step in the dynamic analysis is to determine the modal characteristics of the fixed base spacecraft. This is done by a modal analysis.

The modal analysis actually serves two functions. First and most important, it calculates the spacecraft undamped natural frequencies and their associated modal deflections and loads. This data will be used in the forced response analysis to calculate nodal displacements and accelerations and element loads. The modal analysis additionally serves as a check on the modeling techniques used in the model generation phase. The calculated frequencies and mode shapes are key elements to be used for a feasibility check of the model. Any inconsistencies should be evaluated for their effect on the subsequent response analysis and corrected if necessary. The modal analysis results are used to do a preliminary sizing, based on stiffness requirements, of the primary structure. Generally, this involves several iterative steps until the desired results are obtained. Typically, the spacecraft should have a fundamental frequency high enough to minimize launch vehicle coupling and should exhibit a good frequency separation between the higher modes of the spacecraft and the major structural components. Therefore, the modal analysis phase usually means generating several finite element models in addition to the model shown in Fig. 3 (i.e., equipment, solar panels, etc.) and a separate modal analysis of each.

The modal analysis calculates the system natural frequencies and mode shapes by solving the equations of motion for a multi-degree-of-freedom system. To do this, it must calculate the mass and stiffness matrices of each element from the defined geometry data and formulate the equation of motion as follows*

$$[K] - w_r{}^2[m]\{\phi^{(r)}\} = 0 \qquad [1]$$

where: $[K]$ = system stiffness matrix.
$[m]$ = diagonal mass matrix.
w_r = the rth eigenvalue.
ϕ_r = the rth eigenvector.

Since some of the terms of the diagonal of the mass matrix could be zero, the program sorts and partitions the matrix into dependent and independent coordinates. Eq. [1] becomes

$$\left\{\begin{bmatrix} K_{11} & K_{12} \\ K_{21} & K_{22} \end{bmatrix} - w_r{}^2 \begin{bmatrix} 0 & 0 \\ 0 & M_{22} \end{bmatrix}\right\} \begin{Bmatrix} \phi_1{}^{(r)} \\ \phi_2{}^{(r)} \end{Bmatrix} = 0, \qquad [2]$$

where the subscript 1 is associated with the dependent coordinates (i.e., those terms associated with zero mass elements) and the subscript 2 is associated with the independent coordinates (i.e., those terms as-

* MRI/STARDYNE Theoretical Manual, Control Data Cybernet Services, Revision A.

sociated with non-zero mass elements). Two equations can be generated from Eq. [2]:

$$[K_{11}]\phi_1^{(r)} + [K_{12}]\phi_2^{(r)} = 0 \qquad [3]$$

and

$$[K_{21}]\phi_1^{(r)} + [K_{22}]\phi_2^{(r)} - w_r^2[M_{22}]\phi_2^{(r)} = 0 \qquad [4]$$

If Eq. [3] is rearranged as

$$\phi_1^{(r)} = -[K_{11}]^{-1}[K_{12}]\phi_2^{(r)}$$

and substituted into Eq. [4], we obtain

$$[K_{21}](-[K_{11}]^{-1}[K_{12}]\phi_2^{(r)}) + [K_{22}]\phi_2^{(r)} - w_r^2[M_{22}]\phi_2^{(r)} = 0.$$

Rearranging and collecting like terms of $\phi_2^{(r)}$ gives:

$$([K_{22}] - [K_{21}][K_{11}]^{-1}[K_{12}])\phi_2^{(r)} - w_r^2[M_{22}]\phi_2^{(r)} = 0. \qquad [5]$$

In this equation, let

$$[K_{22}^*] = [K_{22}] - [K_{21}][K_{11}]^{-1}[K_{12}],$$

such that the following result is obtained:

$$([K_{22}^*] - w_r^2[M_{22}])\phi_2^{(r)} = 0. \qquad [6]$$

Eq. [6] contains only the independent coordinates or the dynamic degrees of freedom. These are the degrees of freedom in the finite element model that have mass. Eq. [1] has, therefore, been reduced by elimination of all unnecessary degrees of freedom for the solution of the problem. This improves the quality as well as the efficiency with which the solution itself is performed. The following transformation is performed in order to obtain the necessary form of Eq. [6] for an extraction routine:

$$\phi_2^{(r)} = [M_{22}]^{-1/2}u^{(r)}.$$

Substituting this into Eq. [6] and premultiplying both sides of the equation by $[M_{22}]^{-1/2}$ gives

$$([M_{22}]^{-1/2}[K_{22}^*][M_{22}]^{-1/2} - w_r^2[I])u^{(r)} = 0. \qquad [7]$$

By letting

$$[K'] = [M_{22}]^{-1/2}[K^*][M_{22}]^{-1/2},$$

Eq. [7] can be written as

$$([K'] - w_r^2[I])u^{(r)} = 0. \qquad [8]$$

Eq. [8] is the desired form of the dynamic equation.

Fig. 5 (top) gives the mode shapes and their associated frequencies

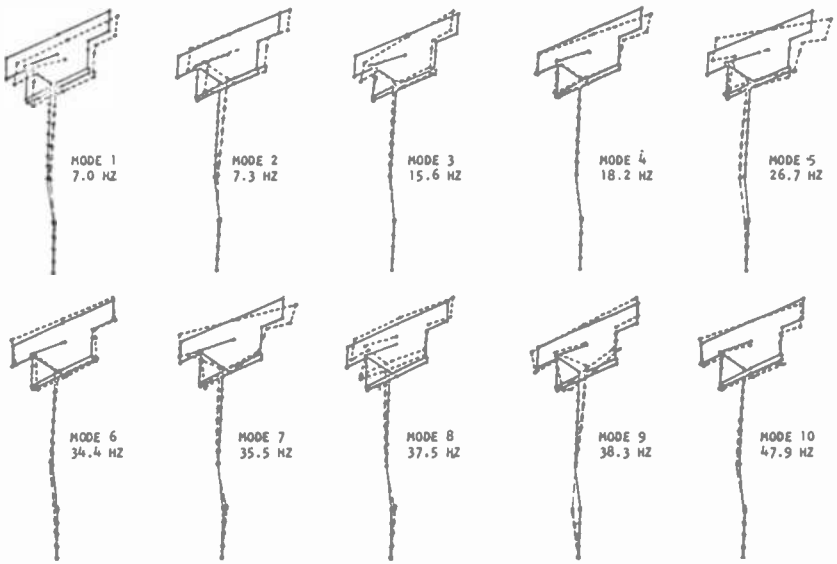

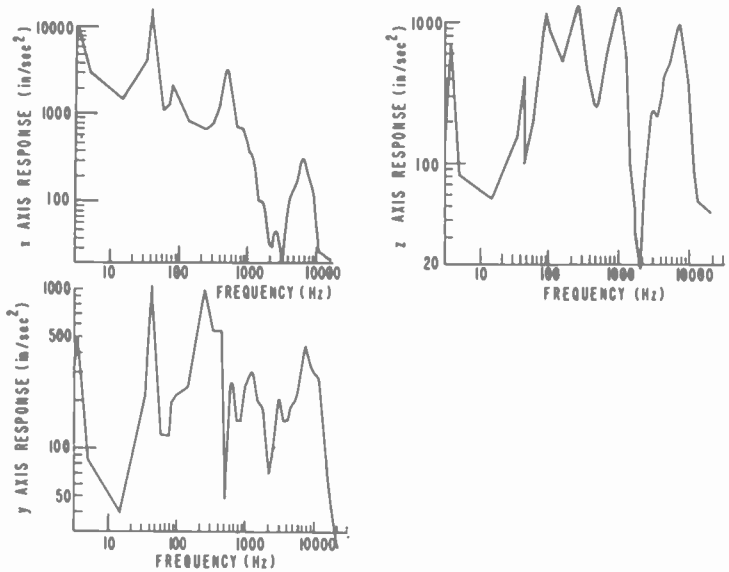

Fig. 5—(Top) Mode shapes and associated frequencies for TIROS-N spacecraft and (bottom) frequency versus acceleration plots used to determine cross coupling between orthogonal axes.

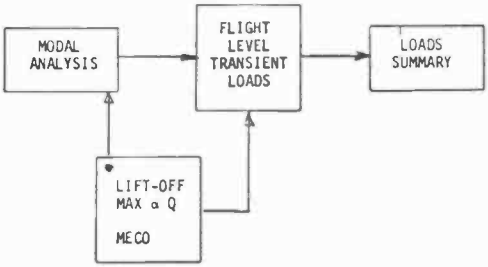

Fig. 6—Launch-vehicle loads analysis. The asterisk indicates that a different mass distribution is required for each flight event.

of the TIROS-N spacecraft. The first two modes are the fundamental bending modes in each lateral direction. Modes 3 and 4 are the IMP bending modes. Modes 5 through 9 are combined bending of the spacecraft and IMP, and finally, mode 10 is the first thrust mode of the spacecraft. A sinusoidal 1g base excitation response analysis is then done, with typical results as shown in Fig. 5 (bottom). These frequency versus acceleration plots are used to determine the amounts of cross coupling between the orthogonal axis for each axis excitation. As shown by the curve in Fig. 5 for X axis excitation, the TIROS-N spacecraft exhibits some degree of cross-coupling between the Y and Z axes; the amount

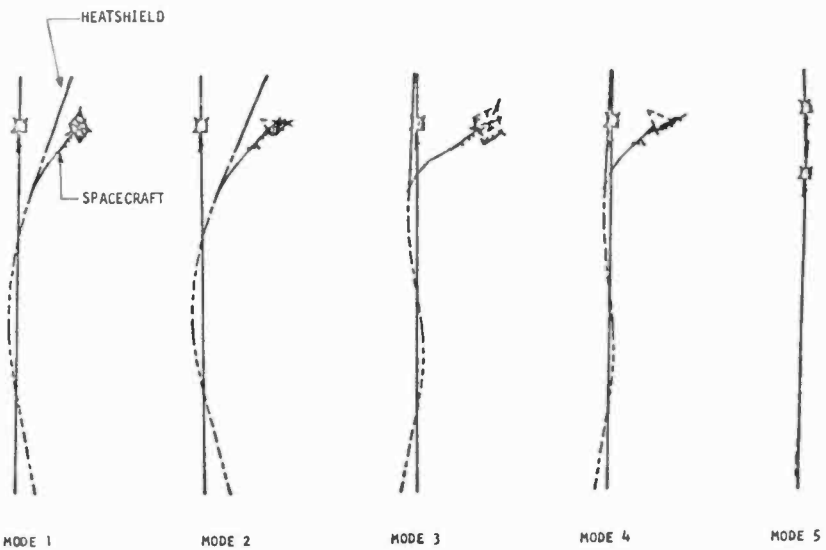

Fig. 7—Launch vehicle mode shapes (free-free) for lift-off mass distribution.

varies at each natural frequency. Generally, it is best to keep the axis cross-coupling to a minimum. However, due to the nonsymmetrical mass and stiffness distribution of a spacecraft such as the TIROS-N, this is not always possible or practical.

2.3 Flight Loads Analysis

Once the results of the spacecraft modal analysis are known, the flight level responses due to the flight dynamic loads shown in Fig. 2 can be calculated. This involves combining the finite element models of the spacecraft with the overall launch vehicle. A typical loads analysis is shown in Fig. 6. Since each flight event occurs at a different time during the launch, the mass distribution of the finite element model will change. Therefore, each event requires a separate modal analysis. The results of the modal analysis are then used to develop the flight level responses for each flight event. Fig. 7 shows the launch-vehicle modes for the lift-off condition. Modes 1 and 2 are the fundamental bending modes of the launch vehicle in each lateral direction. Modes 3 and 4 are the spacecraft lateral bending modes and mode 5 is the launch vehicle thrust mode. The results of the launch loads analysis is a loads summary. This summary

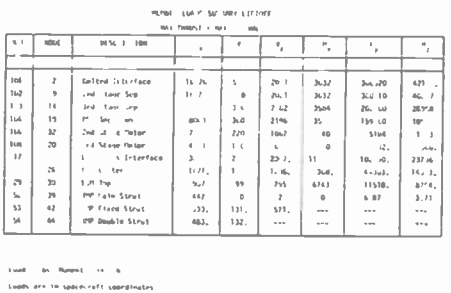

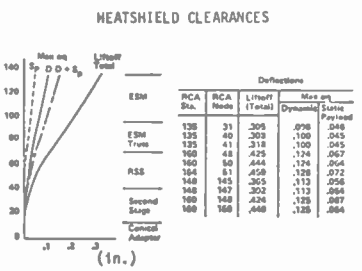

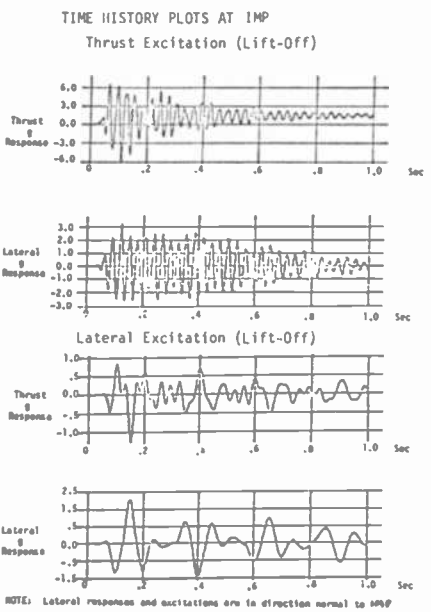

Fig. 8—Flight level responses.

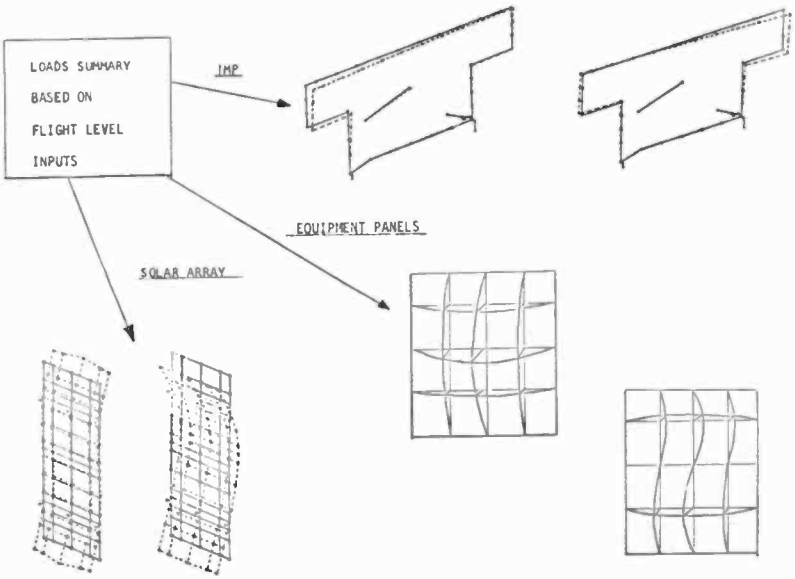

Fig. 9—Component dynamic analysis.

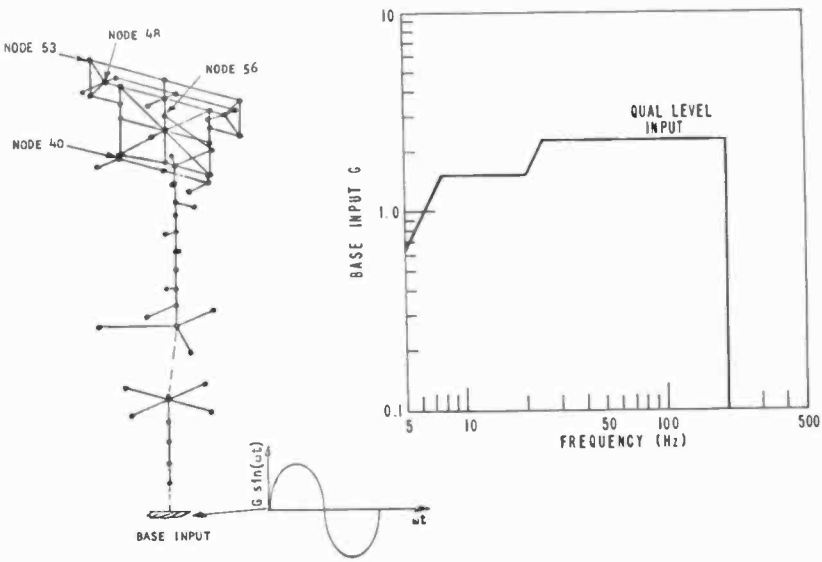

Fig. 10—Spacecraft sinusoidal vibration test specification (qualification level).

includes spacecraft member loads, critical heatshield clearances, and nodal time history plots for each of the flight events. Fig. 8 shows the results of the TIROS-N launch-vehicle loads analysis. Based on these loads, a dynamic analysis is done for each component of the spacecraft, such as the equipment and solar panels as illustrated in Fig. 9. The component dynamic analysis and subsequent stress analysis complete the loads generating cycle.

3. Loads Verification Cycle

In the loads verification cycle, the spacecraft finite element model is used to determine realistic input levels, based on the launch-vehicle loads analysis, for a sinusoidal base excitation test. This test is required to verify that the structure is flight ready. Fig. 10 gives a sinusoidal vibration test specification for the TIROS-N spacecraft. The input level given, however, will greatly overload portions of the structure. Since the structure is designed to withstand flight level responses, with appropriate factors of safety, it should not have to withstand loads that are unrealistically high. Therefore, the test input levels shown in Fig. 10 are allowed to be lowered or notched at critical spacecraft frequencies.

The finite element model is a perfect tool to determine what these notched test levels must be. This is done by calculating the qualification level loads at critical points on the spacecraft and comparing these with

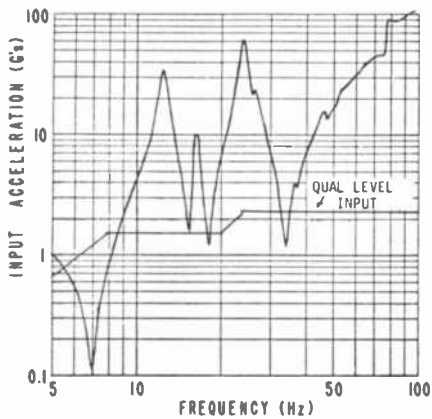

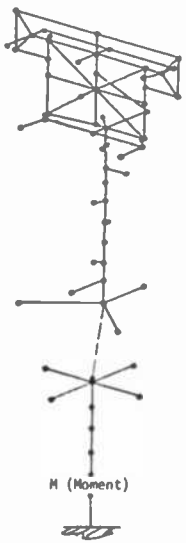

Fig. 11—Base input limit of separation-plane moment.

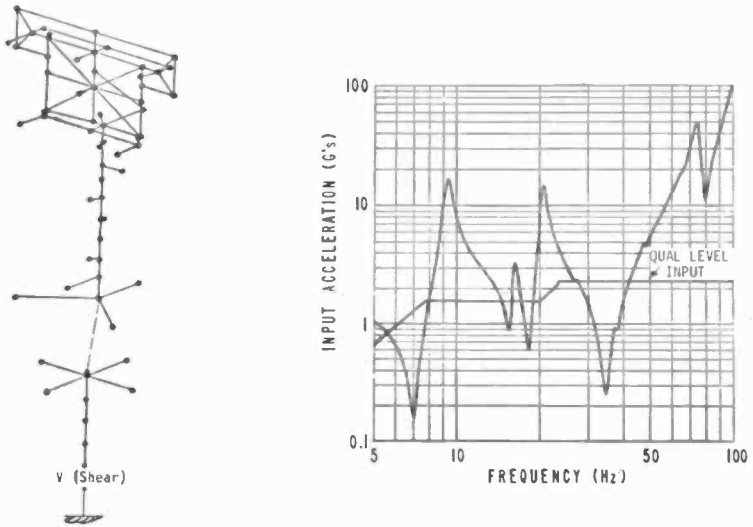

Fig. 12—Base input limit of separation-plane shear.

the loads developed during the loads generating cycles. The critical areas for the TIROS-N spacecraft are the separation plane and IMP struts. Figs. 11 through 14 show the base input *g* limits required at each of these points so that overloading does not occur. The *g* spectrum that is less than the qualification level specification, given in Figure 10, will require notching limits during the test. The results of Figures 11 through 14 are summarized in Fig. 15a. This figure shows at what frequency and to what

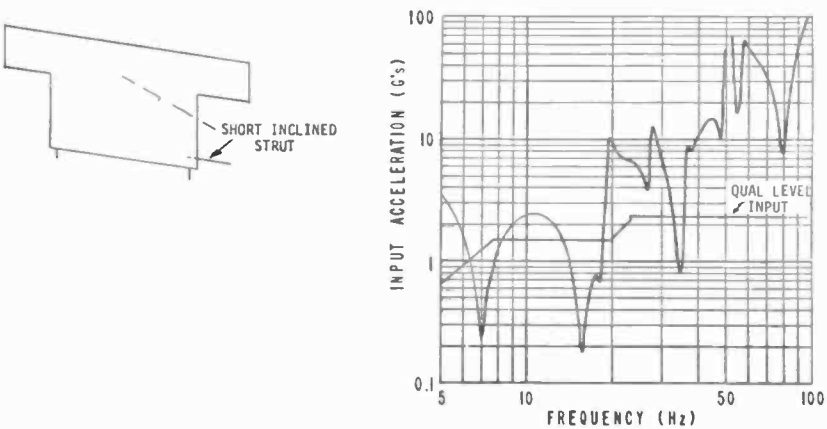

Fig. 13—Base input limit of short inclined strut.

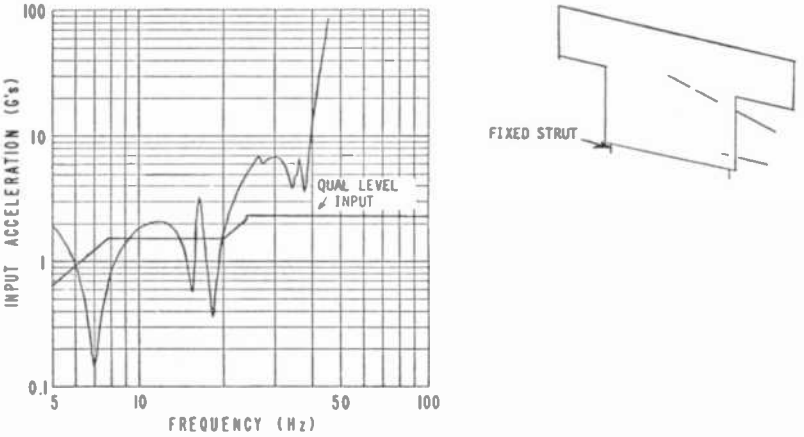

Fig. 14—Base input limit of short vertical (fixed) strut.

degree the qualification specification must be notched to preclude overloading at the critical point on the spacecraft. The 7 Hz notch is required to limit the bending moment at the separation plane. The 15 and 18 Hz notches are required to limit overloading of the IMP strut; and, finally, the 35 Hz notch is required to limit the separation plane shear. It is easy to see from this figure that the first notch occurs at the spacecraft fundamental frequency, since that is when the highest moment will occur at the separation plane. The second two notches occur at the IMP bending modes and the last notch is required at the second lateral bending mode of the spacecraft since that is when the highest

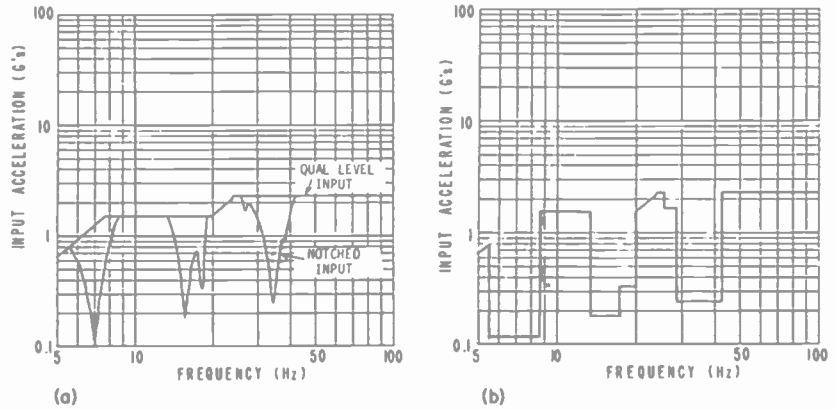

Fig. 15—Predicted qualification level for base input notch limits. The figure on the left summarizes Figs. 11–14 and that on the right shows enveloped results.

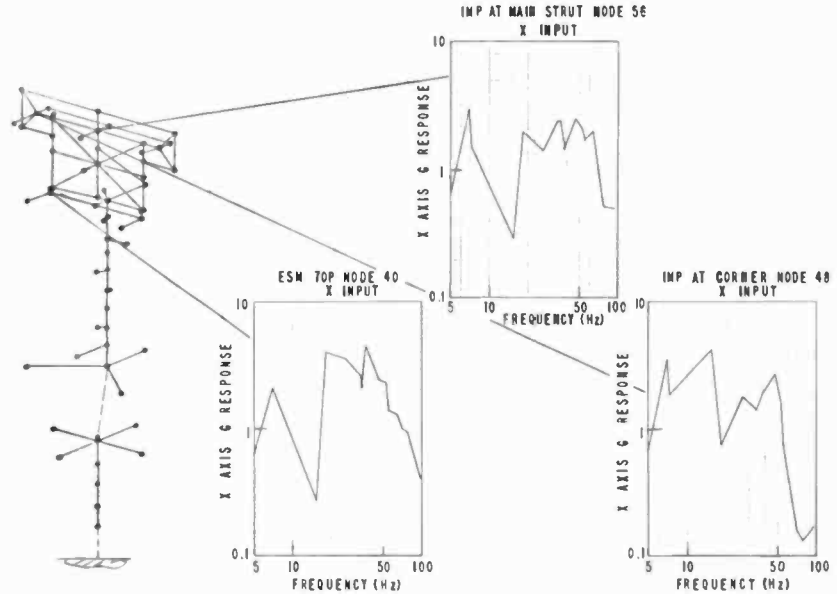

Fig. 16—Predicted qualification level responses for notched base input maximum responses at spacecraft natural frequencies.

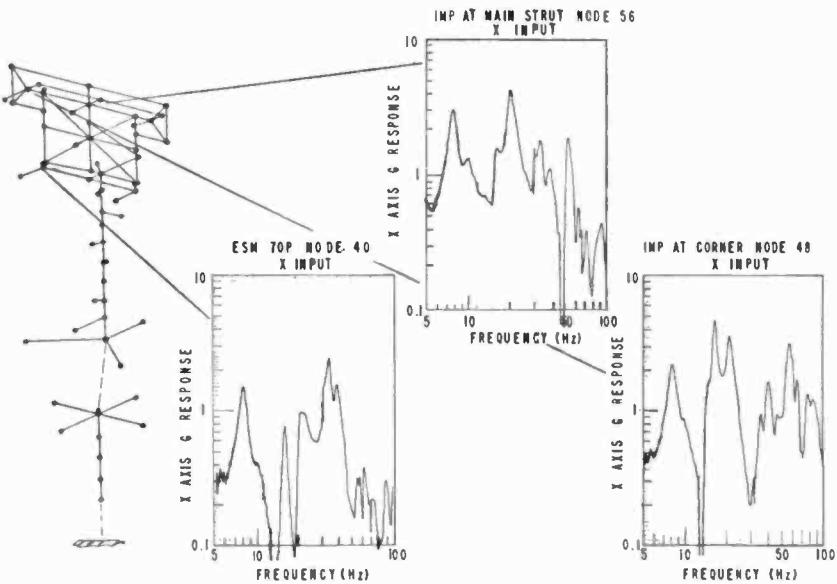

Fig. 17—Actual qualification test level responses.

separation plane shear is produced. These results can easily be verified by comparison with the mode shapes shown in Fig. 5a.

The plots of acceleration versus frequency shown in Fig. 15b are the enveloped results given in Fig. 15a and are used as input for the sinusoidal test in the X axis. A similar procedure results in the other axes test specification. These test levels are then applied to the finite element model in order to determine the predicted response levels of the spacecraft for direct comparison with the test results. Fig. 16 gives the predicted test level responses for the TIROS-N spacecraft and several locations of the structure. Since the actual test of the spacecraft has been completed, the corresponding test response levels can be compared. Fig. 17 gives the actual test level responses at the IMP corner and main strut and at the ESM top. As the figure shows, a good agreement exists between test and analysis results given in Fig. 16. Some differences can be expected due to the structure damping assumptions used for the analysis.

Variational and Finite Element Methods in Structural Analysis*

Theodore H. H. Pian

Professor of Aeronautics and Astronautics, Massachusetts Institute of Technology, Cambridge, Mass. 02139

Abstract—The paper presents a brief survey of the various finite element models derived by the conventional variational principles in structural mechanics and by several modified variational principles which permit the relaxation of condition of displacement continuity or traction reciprocity along the interelement boundaries. The use of the various finite element models is illustrated by their convenience in formulating plate and shell elements, by the reduction of constraints that may appear in limiting cases in assumed displacement methods, and by the construction of special elements for problems with stress singularities. Rationalization in incremental formulation of nonlinear problems can also be obtained by variational approach.

1. Introduction

Nearly a quarter of a century ago, Jon Turner of the Boeing Company presented a paper[1] entitled "Stiffness and Deflection Analysis of Complex Structures." The new method he introduced at that meeting was developed for static and dynamic analysis of aircraft structures. It was an extension of the matrix displacement method traditionally based on stiffness matrices of bars and beams. The method by Turner and his associates was developed to apply to continuous structures that are discretized into a finite number of elements. Professor Argyris[2] at the

* This paper was presented by Professor Pian at an RCA Finite Element Symposium held at RCA Laboratories, Princeton, N.J. on March 13–14, 1978. It has also been published in the *Israel Journal of Technology*, Vol. 16, Nos. 1–2, pp. 23–33, 1978.

same time also published in *Aircraft Engineering* a method for determining element stiffness matrices of panels under membrane stress based on energy principles. These early pioneering works can now be rationally interpreted as a Rayleigh-Ritz method in conjunction with the principle of virtual work or the principle of minimum potential energy. The method is, of course, the well-known finite element method, which has now been extended to all types of structural and solid mechanics and to many other problems in continuum mechanics. In addition to the conventional approach based on assumed displacements and the potential energy principle, alternative approaches and improved methods have been developed. Indeed, large portions of these advancements were motivated by the development in aerospace structural technology. The rapid progress in the development of finite element methods owes much, of course, to the rapid advancement of high-speed automatic digital computers during the last quarter of a century. It is the author's opinion, however, that the advancement in the finite element method is also due largely to its wide mathematical basis. In addition to the formulations by this principle, improved finite element methods can be derived by other variational principles, many of which are modifications of conventional variational principles, by relaxing the continuity requirement along the interelement boundary.[3–5] In this paper, a brief outline will be given of this expanded domain of finite element methods.

It was recognized since the very early days in the development of finite element methods that some difficulties exist in the assumed displacement approach. When problems in plane elasticity were extended to bending of thin plates, it was found difficult to construct shape functions that are compatible for the lateral displacement w as well as its normal slope $w_{,n}$ along the interelement boundaries. Another recognized drawback in the assumed displacement approach is the loss of accuracy in stresses when evaluated by derivatives of displacements. For many limiting cases in solid mechanics, the existence of certain conditions of constraints will require alternative methods of formulation. For example, when the assumed displacement finite element method was first used to analyze solid propellents it became evident that for a nearly incompressible material, for which the dilatation approaches zero, the conventional finite element model may become extremely stiff. Of course, in the case of an incompressible material the condition of zero dilatation must be introduced to modify the principle of minimum potential energy and hence to change the finite element formulations. Finally, it has been proved that for problems involving stress singularities, the use of conventional elements will lead to extremely slow convergence for the solutions.

In the main part of this paper some examples will be given to illustrate how the difficulties listed above can be overcome by finite element formulations based on alternative variational principles. Finally, some brief remarks will be made on the variational formulation of nonlinear structural mechanics problems.

2. Variational Principles for Finite Element Methods

The variational principles for finite element methods can be described by the flow diagram for small deflection theory of elastostatics shown in Fig. 1. The upper part of the figure shows the conventional variational principles. Starting from the principle of virtual work, one can derive the principle of minimum potential energy, with the variational functional π_p, which contains displacement components as the only field variables. The conventional finite element formulation is simply a Rayleigh-Ritz method using piecewise assumed shape functions with

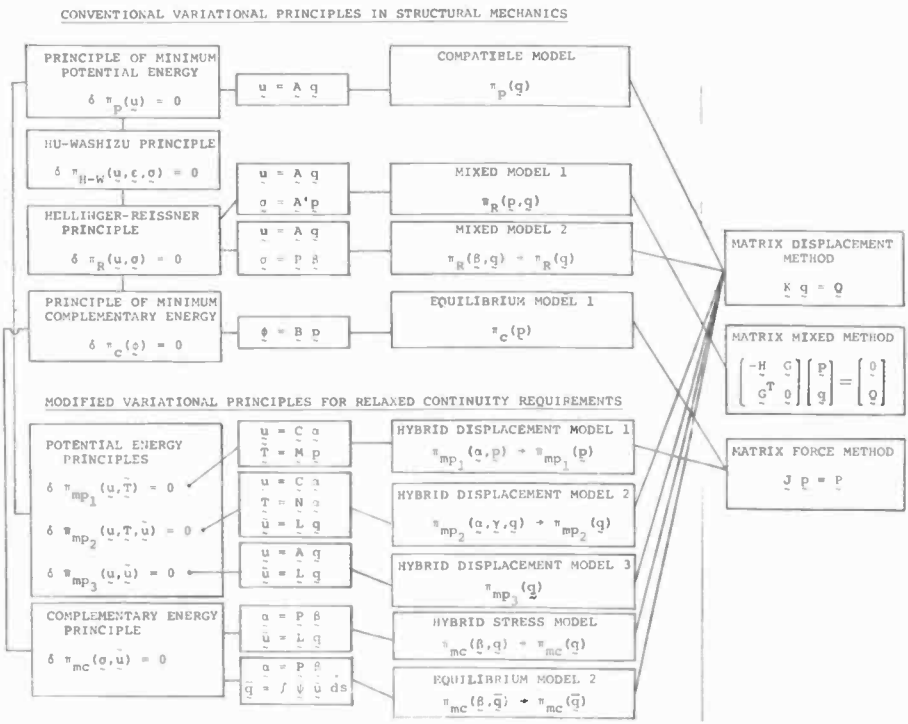

Fig. 1—Flow diagram for variational formulation of finite element methods.

nodal displacements **q** as generalized coordinates. The final equation is of the form

$$\mathbf{K}\,\mathbf{q} = \mathbf{Q} \qquad [1]$$

were **K** is the assembled stiffness matrix of the structure and **Q**, the assembled vector of equivalent nodal forces. This is, of course, a matrix displacement method; when the shape functions are compatible along the interelement boundaries, the corresponding finite element nodal is named the compatible model.

By means of a most general Hu–Washizu Principle with stress, strain, and displacements as field variables, one can derive the well known Hellinger–Reissner Principle based on the variational functional π_R which contains both stress and displacements as field variables. A corresponding finite-element formulation would contain nodal values of stresses **p** and displacements **q** as unknowns. The final equation, which corresponds to the matrix method, is of the form

$$\begin{pmatrix} -\mathbf{H} & \mathbf{G} \\ \mathbf{G}^{\mathrm{T}} & \mathbf{O} \end{pmatrix} \begin{pmatrix} \mathbf{p} \\ \mathbf{q} \end{pmatrix} = \begin{pmatrix} \mathbf{O} \\ \mathbf{Q} \end{pmatrix} \qquad [2]$$

where **H**, **G** and **Q** are again obtained by assembling the corresponding element matrices. The global matrix in Eq. [2] is nondefinite; hence the solution routines for many finite element analysis programs which are based on positive definite stiffness matrices cannot be readily used.

Since in applying the Hellinger–Reissner principle it is not necessary to maintain the continuity of stresses or even the traction reciprocity along the interelement boundary, it is possible to approximate the stresses in terms of stress parameters that are independent from one element to the other. Such parameters can then be expressed in terms of the nodal displacements, and the resulting matrix equations will have only the nodal displacements as unknowns. It has been pointed out, however, by Fraeijs de Veubeke that without restrictive assumptions on the stresses, the last scheme will lead to the same result as the simple assumed displacement method.[6]

When the stresses are equilibrating, the Hellinger-Reissner principle becomes the principle of minimum complementary energy, with the variational functional π_c which contains stress functions as the field variables. The corresponding finite element methods can, of course, be developed with nodal values of stress functions as unknowns. The finite element model is called the equilibrium model.

In applying the various variational principles for a solid continuum that is divided into finite elements, it is realized that certain discontinuity conditions along the interelement boundaries are allowed to the degree that the variational functionals exist. However, an even broader

extension of the variational methods lies on the possibility of further relaxation of the continuity conditions along the interelement boundaries by the introduction of interelement constraint conditions and the corresponding Lagrangian multipliers. The modified variational principles thus contain the Lagrangian multipliers as additional boundary variables. The new approach in finite element method, which involves independent approximations of interior and boundary variables, is generally called the hybrid formulation.[7] Because the parameters representing the field variables for the interior of the elements are now independent from one element to the other, they may be expressed in terms of the parameters in the element boundary by applying the variational principle in the element level.

For example, a modified complementary energy principle based on a functional π_{mc} can be derived by introducing the traction reciprocity conditions as equations of constraint, and the corresponding Lagrange multipliers are the element boundary displacements. This modified principle then becomes a two field principle.[8,9] In the finite element formulation the boundary displacements can be interpolated in terms of nodal displacements $\mathbf{q}$, while the stresses in the element are approximated by stress parameters β. After eliminating β in the element level, the nodal displacements $\mathbf{q}$ become the only unknowns. This method is called the assumed stress hybrid method or simply hybrid stress model. This modified principle, however, can be utilized in a different way. If the traction reciprocity condition are to be maintained while generalized boundary displacements are defined to represent the integrated effects, the resulting finite element method will only have such generalized displacements as unknowns. But it is then an equilibrium model.[6]

The dual modified principle for potential energy based on the functional π_{mp}, is a two-field principle with tractions along the interelement boundaries as Lagrange multipliers.[10] If in the finite element implementation the displacement parameters in one element are independent of those in other elements, they can be eliminated in the element level and the resulting equations will contain only nodal stresses as unknowns. Thus it is a kind of matrix force method.

A second modified potential energy principle based on π_{mp_2} is to treat boundary displacements $\tilde{\mathbf{u}}$ and interior displacement $\mathbf{u}$ as independent, and then to introduce boundary tractions $\mathbf{T}$ as Lagrange multipliers to maintain the compatibility at the element boundary.[11] This becomes now a three-field principle. However, since both $\mathbf{T}$ and $\mathbf{u}$ in one element may be independent of those in other elements, the finite element formulation may lead to final equations that contain only nodal displacements as unknowns. This model which is named hybrid displacement model 2 is thus a matrix displacement method. A simplified version of

this principle based on π_{mp3} is to introduce the relation between stresses and displacements to express T in terms of **u**.[11,12] In the finite element formulation both **u** and $\tilde{\mathbf{u}}$ may be expressed in terms of nodal displacements **q** and the resulting method is, of course, again a matrix displacement method.

Many other possible variational principles can be formulated for the development of finite element methods. Knothe[13] made a systematic classification of such possibilities. Wolf[14] has implemented several generalized assumed stress models for finite element analysis.

3. Plate and Shell Analysis

One of the major difficulties in formulation of plate and shell elements by assumed displacement approach is the construction of shape functions that can maintain not only the compatibility of the lateral displacement w but also its normal slope $w_{,n}$ at the interelement boundary. Indeed, one common objective of the various finite element models described in the previous section was to get around such difficulty.

The assumed stress hybrid model was first demonstrated by a rectangular plane stress element[15] but was immediately extended to thin plate elements.[16–19] Its versatility was illustrated by the fact that plate elements of any number of edges can be derived by essentially the same formulation.[20] The hybrid stress model has also been used for plates with transverse shear effect[8] and for laminated plates for which the transverse shear strains may be different in different layers.[21] One important precaution to be made in the application of assumed stress models (for both hybrid stress model and equilibrium model) is to choose adequate numbers of stress parameters to avoid any kinematic modes in the individual element. A necessary condition for such choice is that the number of stress parameters should be equal to or larger than the number of nodal displacements minus the number of rigid-body degrees of freedom.[22] Unfortunately, these conditions are not sufficient. It has been demonstrated that for certain plate geometry the given limited stress terms will lead to zero work due to certain boundary displacements that do not correspond to a rigid body motion.[15] Such deformation modes are obviously kinematic modes.

The assumed displacement hybrid model based on π_{mp1} was initially illustrated for plate and shell analyses by independent assumption for interior displacements and boundary tractions.[23] A more logical scheme is to interpolate the displacements **u** of the element in terms of nodal displacements $\tilde{\mathbf{q}}$ by shape functions that maintain the compatibility of the displacement w but not of the normal slopes at the interelement

boundary. Lagrange multipliers λ are then introduced to maintain such compatibility.[24,25] The resulting matrix equations are in the form of

$$\begin{pmatrix} \mathbf{K} & \mathbf{J}^{\mathrm{T}} \\ \mathbf{J} & \mathbf{O} \end{pmatrix} \begin{pmatrix} \mathbf{q} \\ \lambda \end{pmatrix} = \begin{pmatrix} \mathbf{Q} \\ \mathbf{O} \end{pmatrix} \qquad [3]$$

This is a mixed method that involves an indefinite matrix. The convergence of π_{mp_1}, however, has been proved.[26] In fact, by recognizing that the present problem is simply a constrained minimization of an original Ritz method, the required programming changes are very simple.[24] The method has also been applied to the analysis of both linear and geometrically nonlinear problems of thin shells.[27,28]

The modified potential energy principle based on π_{mp_2} has been utilized to derive stiffness matrices of a rectangular flat plate element[11] and of a doubly curved quadrilateral element that forms a part of a general shell of revolution.[29] The implementation of the finite element model is somewhat complicated because of the need to approximate three individual sets of field variables, the element displacements, the boundary displacements, and the boundary tractions. It turns out that in several example problems in shells of revolution, the solutions in both displacements and stresses obtained by this assumed displacement hybrid model are identical to that by a compatible displacement model. The latter is, of course, easier to implement than the former.

The simplified hybrid displacement model based on π_{mp_3} is relatively easy to implement and it has been applied successfully to plates and shells of both quadrilateral and triangular shapes.[12] It has also been extended to large deflection analysis of elastic plastic plates and shells.[30] However, it has been demonstrated[26] that a certain triangular plate element derived by this model actually becomes unstable. Thus, caution is required in the application of this finite element model.

The mixed model based on the Hellinger-Reissner principle is attractive for plate and shell elements because of the requirement of only C° continuity for the assumed out-of-plane displacement. It also has the feature of maintaining the continuity of stresses along the interelement boundaries. Hence it will, in general, provide better results in stresses than other finite element models. Most recent developments for this model include laminated composite plates and shells with transverse shear effect.[31–33] Both quadrilateral and triangular elements have been developed for linear and geometrically nonlinear problems. For a given mesh size the number of unknowns by a mixed formulation is always larger than that by the conventional matrix displacement method. Thus, the advantage of better accuracy in stress evaluation is offset by the larger computing effort required. More efficient schemes using a symbolic and algebraic manipulation language such as MACSYMA have

been employed for the evaluation of numerous integrals in the element matrix formulation. Also, the number of numerical coefficients to be calculated can be considerably reduced by the use of the group-theoretic technique. Computing effort and storage required can also be relieved by efficient choice of the submatrix method.[33]

4. Constraints in Conventional Assumed Displacement Methods

In the formulation of the finite element method by assumed displacement approach, when in the limit case some conditions of constraint exist for the strain components, the principle of minimum potential energy is no longer applicable. In practice, even in the nearly limiting case, the conventional assumed displacement finite element may lead to very rigid element stiffness matrices and thus yield very inaccurate solutions.

For example, for an incompressible material, the condition of constraint is the vanishing of the mean strain. Thus in analyzing a problem of nearly incompressible material by the conventional assumed displacement method, the condition of zero dilatation may introduce a number of constraint conditions to the assumed displacements. Hence, the resulting element stiffness matrix may become extremely rigid.

Another example is the derivation of element stiffness matrices for plates and shells taking into account transverse shear effect. The requirement of interelement continuity of normal derivative $w_{,n}$ is replaced by that of boundary rotations which are now independent of w. The scheme would breakdown when the plates and shells are very thin, so that the condition of diminishing shear strain will introduce a severe constraint to the element displacements. A practical technique to reduce such constraints is to use reduced or selective numerical integration in the construction of the element stiffness matrices.[34]

Another possible constraining condition exists for shell analysis. The total strain energy for shells may be separated into the stretching energy and the bending energy. Since shell elements are often formulated in such a manner that the constant strain states and the rigid body modes are not explicitly included in the assumed displacements, errors due to such incomplete representation are magnified in the stretching energy term by a factor proportional to the ratio of the radius of curvature of the shell to the thickness. Therefore for thin shells, the condition of vanishing of the stretching strain introduces further constraints to the assumed displacements.

Effective remedies to these problems are the use of a modified version of the Hellinger–Reissner principle. In many structural mechanics problems the total strain energy can be separated into two parts respectively due to two strain vectors ϵ_1 and ϵ_2, where the latter is the one

that is to be constrained in the limiting case. In a modified variational principle, only the strain energy of the latter is to be reduced to the form of the Hellinger–Reissner functional. The variational functional is thus in the form

$$\pi_{mR} = \int \left(\frac{1}{2} \epsilon_1^T \mathbf{C}_1 \epsilon_1 + \sigma_2^T \epsilon_2 - \frac{1}{2} \sigma_2^T \mathbf{S}_2 \sigma_2 \right) dV + W, \qquad [4]$$

where σ_2 represents the stresses corresponding to ϵ, $\mathbf{C}_1$ and $\mathbf{S}_2$ are the respective elastic constants, and W is potential energy due to applied load. The strains ϵ_1 and ϵ_2 are expressed in terms of displacements and, in the finite element formulation, they are represented by nodal displacements $\mathbf{q}$. For example, in the variational functional proposed by Key[35] for incompressible and nearly incompressible materials, ϵ_1 represents deviatoric strains and ϵ_2 is the mean strain.

In the finite element formulation, if σ_2 are represented by nodal values of stresses, a matrix mixed method results. However, if σ_2 are independent for the different elements, the resulting equation will have only nodal displacements as unknowns. Again, according to the limitation principle of Fraeije de Veubeke, this will be equivalent to the original assumed displacement method. It can be shown, however, that the number of equations of constraint to the displacement functions is equal to the number of stress parameters used to represent σ_2. Indeed, in solving problems of nearly incompressible materials using the functional of Key, it is necessary to use a lower approximation for the spherical strain energy.[36] For plate and shell analysis, it turns out that by proper choice of the stress parameters the mixed formulation yields element stiffness matrices that are identical to that of the assumed displacement method using reduced or selective numerical integration.[37–39] The mixed formulation derived from this version of the Hellinger–Reissner principle thus offers a rational justification of the reduced integration element, and provides a more general scheme for relieving the constraints that may occur in an assumed displacement finite element method. It is well known that a reduced integration scheme may lead to kinematic modes in the assumed displacement method. Thus precaution is also needed in implementing the mixed formulation to avoid the creation of kinematic modes.

The assumed stress hybrid model is also a very effective scheme for reducing the severe constraints that appear in the conventional assumed displacement finite element method. One illustrative example[36] is the solution of problems of nearly incompressible materials. A plane strain problem consists of a square planform with the upper edge clamped, with one side edge restrained horizontally but free to slide vertically and the other side edge completely free. The lower edge is acted on by uniform

Table 1—Solutions for Displacement at the Unsupported Corner of a Square-Shaped Plane Strain Panel ($\delta E/pa$) $\times 10^6$

Element Mesh	Hybrid Stress Model 7 Stress parameters 1 × 1	2 × 2, 4 × 4	Key's Mixed Model Constant mean stress 1 × 1	2 × 2	Displacement Model Bi-linear interpolation 1 × 1	2 × 2
Poisson's Ratio						
0.33	47.8	46.3	50.3	46.5	44.5	45.5
0.40	44.5	43	48.5	43.3	37.5	41
0.45	41	40	47	40	27.8	34.8
0.48	38.3	37.8	45.8	37.5	15.9	26.5
0.4999	36.3	36	45	35.8	0.12	0.47

Asymptotic solution for incompressible material ($\delta E/pa$) = 36×10^{-6}

pressure p. The solutions are based on conventional matrix displacement method using three different four-node rectangular elements: (1) displacement element by assumed bilinear shape function, (2) element derived by the reduced form of Hellinger–Reissner principle of Key using constant mean stress, and (3) assumed stress hybrid element with seven stress parameters. Solutions for the vertical displacement at the unsupported corner were obtained for materials of different Poisson's ratio and by using different mesh sizes. The solutions by the assumed stress hybrid model using both 2 × 2 and 4 × 4 meshes are identical; hence they can be considered as the reference solutions. It can be seen from the solutions listed in Table 1 that the assumed displacement element has already become very rigid for $\nu > 0.45$, while both the elements by the mixed model of Key and by the assumed stress model can be used effectively for nearly incompressible material up to $\nu = 0.4999$. Also, a plate element derived by the assumed stress hybrid model and by taking transverse shear into account has been shown to yield accurate results for plates and shells of a wide range of thickness-size ratios.[40]

5. Fracture Analysis

In fracture mechanics for brittle materials or for elastic plastic materials under small-scale yielding, the governing parameters are the elastic stress intensity factors K_I, K_{II} and K_{III} which specify the intensities of stress singularity in the tearing mode, the inplane shear mode, and the out-of-plane shear mode, respectively. Although the assumed displacement finite element method can be modified to develop "crack" elements for which the stresses vary with $1/\sqrt{r}$, where r is the distance from the crack tip, a more versatile approach is the use of hybrid elements.

There exists three basic finite element hybrid models for the devel-

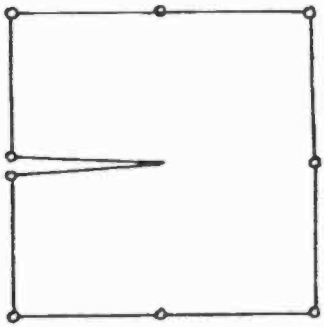

Fig. 2—A "crack" element with embedded crack.

opment of special singular elements for linear fracture mechanics.[41] The three basic schemes for these models are as follows:

(1) A scheme that is based on a complete series expansion of the stresses near the tip of the crack and on independently assumed boundary displacements to match the displacements of the neighboring element.[42] Thus, the assumed stresses include the singular terms and are all equilibrating. They also satisfy the compatibility condition inside the element and the stress free condition along the crack surface. Such a model is based on the hybrid stress model, but it may also be interpreted as a hybrid displacement model. Under this scheme, the crack surface is embedded in the element (Fig. 2); hence all the assumed stress parameters can be eliminated in the element level resulting directly in the stiffness matrix for the element. The magnitude of the singular terms are the stress intensity factors to be evaluated for the fracture analysis.

(2) A scheme that is based on assumed equilibrating stress field and on independently assumed boundary displacements. Here, however, only the singular terms satisfy the compatibility condition, and the other terms may be ordinary polynomial expansion.[43] In the finite element formulation several elements are needed around the crack tip (Fig. 3). Since the stress intensity factors are common to these elements, they cannot be eliminated in the element level. The stress intensity factors, however can be eliminated with a group of crack tip elements; hence the stiffness matrix of a super-element can be obtained. Such a model is a hybrid stress model.

(3) A scheme that is based on assumed displacement field including the singular terms and on independently assumed boundary displacements and boundary traction.[44] Such a model is a hybrid displacement model based on π_{mp_2}. For this model, again, several crack elements must

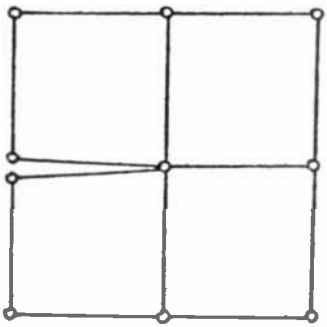

Fig. 3—Four "crack" elements at the crack tip to form a superelement.

be used around the crack tip sharing the same stress intensity factors (Fig. 3). The hybrid displacement model contains three sets of field variables. It is however, more versatile in formulating crack elements with curved crack surfaces.

A square panel with symmetric edge cracks under uniform tension (Fig. 4) has been analyzed by two-dimensional crack elements developed by all the three schemes discussed above. Because of the double symmetry, only one quadrant of panel needs to be modelled. Thus for the last two schemes only two "crack" elements are needed to form a superelement at the crack tip. Table 2 compares the accuracy of the three "crack" elements. The errors were calculated based on an independent analytical solution obtained by Bowie,[45] using the complex stress function and a boundary collocation method. It is clear that the first scheme is superior while the results of the last two are comparable. Similar analyses with conventional assumed displacement elements would re-

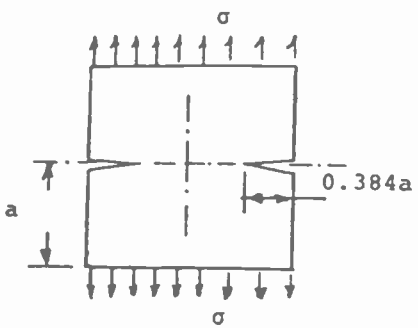

Fig. 4—Square panel with symmetric edge cracks.

Table 2—Comparison of special "crack" elements by hybrid models

Hybrid element scheme	Number of elements in the finite element model	Total dof in model	Error in value of K_I (%)
1 (Hybrid stress/ displacement model)	One 5-node crack element and four 4-node conventional elements	17	0.1
2 (Hybrid stress model)	Two 8-node crack elements and 22 8-node conventional elements	184	0.5
3 (Hybrid displacement model)	Two 8-node crack elements and 22 8-node conventional elements	184	1.0

quire about 1000 degrees of freedom to obtain comparable accuracy.[41] Another advantage of these hybrid formulation is that the stress intensity factors can be evaluated directly when the nodal displacements of the "crack" element are known.

For three-dimensional fracture analysis, however, the first scheme is no longer applicable, because the only available near-field solution is the two-dimensional asymptotic behavior, and the general series solution in three dimensions is not known.

The second scheme has been applied to three-dimensional problems.[46] Here the crack front of the "crack" elements are assumed to be straight line segments and the stress intensity factors are assumed to be constant with each element. The implementation of the assumed displacement hybrid model is comparatively more flexible and 3-D crack elements can be developed with curved crack front and with varying stress intensity factors within each element.[47–49] Hybrid crack elements have also been extended to fracture analysis of anisotropic materials[43,50] and for elastic plastic materials.[49,51]

6. Incremental Analysis for Nonlinear Problems

Geometrically, nonlinear problems and elastic-plastic and creep problems in structural mechanics are almost exclusively solved by incremental methods in finite element solutions. Such methods are often combined with iterative solutions. The nonlinear problems are, thus, reduced to piecewise linear problems and all the finite element models that have been discussed earlier can be extended to nonlinear solutions.[52–54] One important feature of such incremental solution is that at the beginning of a loading or time increment the solution is, in general, not exact, hence it may not satisfy the stress equilibrium conditions and it may also violate the compatibility condition. Hofmeister et al.[55] first

pointed out that by taking the initial equilibrium imbalance at the beginning of the increment into account in formulating the conventional assumed displacement finite element method by the principle of virtual work, the resulting matrix equation will be in the form of

$$\mathbf{K}\,\Delta\mathbf{q} = \Delta\mathbf{q} + \mathbf{R}, \qquad [5]$$

where $\mathbf{R}$ represents equivalent nodal forces to be added to correct the initial stress imbalance. For many other finite element models, in addition to the stress imbalance, there may also be compatibility mismatch at the beginning of the increment that can be corrected by appropriate equivalent nodal forces.[54,56,57] In a recent work on the solution of rubber-like material by a mixed model it was found through a variational formulation that a correction term due to the violation of the condition of incompressibility also appears.[58] It has been found that the inclusion of these correction terms is a very effective means to improve the efficiency of the interative-incremental solutions of nonlinear structural mechanics problems.

7. Concluding Remarks

Although the development of finite element methods has only a very short history of less than a quarter of a century, it already covers a very wide area. The present discussions, thus, have been limited to the variational basis of finite element methods. The advances of finite element methods are obviously the results of the availability of the numerous variational principles in structural mechanics. Another way of looking at it is that the concept of finite element analysis has actually created many new variational principles in structural mechanics. The advantages of using the various finite element models over the conventional assumed displacement models have been identified. But it has also been pointed out that precautions should be used in their implementation.

References:

[1] M. J. Turner, R. W. Clough, H. C. Martin, and L. J. Topp, "Stiffness and Deflection Analysis of Complex Structures," *J. Aero. Sci.*, **23**, p. 805, 854, (1956).

[2] J. H. Argyris, *Energy Theorems and Structural Analysis*, Butterworths Scientific Publications, London (1960).

[3] T. H. H. Pian and P. Tong, "Finite Element Methods in Continuum Mechanics," *Advances in Appl. Mechanics*, **12**, Ed. by C. S. Yih, Academic Press, p. 1–58 (1972).

[4] T. H. H. Pian, "Finite Element Methods by Variational Principles with Relaxed Continuity Requirements," *Variational Methods in Engineering*, Ed. by C. A. Brebbia and H. Tottenham, Southampton Univ. Press, Vol. 1, pp. 3/1–3/24 (1973).

[5] K. Washizu, *Variational Methods in Elasticity and Plasticity*, 2nd Ed., Pergamon Press, Oxford (1975).

[6] B. Fraeijs de Veubeke, "Displacement and Equilibrium Models in the Finite Element Method," *Stress Analysis*, Ed. by O. C. Zienkiewicz and G. S. Holister, John Wiley and Sons, Ltd., London, pp. 145–197 (1965).

[7] T. H. H. Pian, "A Historical Note about 'Hybrid Elements'," *Int. J. Num. Meth. Engng.*, **12**, p. 891 (1978).

[8] T. H. H. Pian and P. Tong, "Rationalization in Deriving Element Stiffness Matrix by Assumed Stress Approach," *Proc. 2nd. Conf. Matrix Methods in Structural Mech.*, AFFDL-TR-68-150, pp. 441–469 (1968).

[9] P. Tong and T. H. H. Pian, "A Variational Principle and the Convergence of a Finite Element Method Based on Assumed Stress Distribution," *Int. J. Solids and Structures*, **5**, p. 463 (1969).

[10] R. E. Jones, "A Generalization of the Direct Stiffness Method of Structural Analysis," *AIAA J.*, **2**, p. 821 (1964).

[11] P. Tong, "New Displacement Hybrid Finite Element Model for Solid Continua," *Int. J. Num. Meth. Engng.*, **2**, p. 78 (1970).

[12] F. Kikuchi and Y. Ando, "A New Variational Functional for the Finite Element Method and Its Application to Plate and Shell Problems," *Nucl. Eng. Des.*, **21**, p. 95 (1972).

[13] K. Knothe, "Variationsprinzipian der Elastostatic mit Gelockerten Stetigkeitsforderunden und ihre Verwendbarkeit im Rahmen der Methode der Finite Elements," Institut für Luft-und Raumfahrt, Technische Univeritat, Berlin (1974).

[14] J. P. Wolf, *Generalized Stress Models for Finite-Element Analysis*, Dissertation No. 5263, E.T.H. Zürich (1974).

[15] T. H. H. Pian, "Derivation of Element Stiffness Matrices by Assumed Stress Distributions," *AIAA J.*, **2**, p. 1333 (1964).

[16] T. H. H. Pian, "Element Stiffness Matrices for Boundary Compatibility and for Prescribed Boundary Stressed," *Proc. Conf. Matrix Methods in Structural Mech.*, AFFDL-TR-66-80, p. 457 (1965).

[17] R. T. Severn and P. R. Taylor, "The Finite Element Method for Flexure of Slabs when Stress Distributions are Assumed," *Proc. Inst. Civil Engng.*, **34**, p. 153 (1966).

[18] J. P. Wolf, "Das Flächentragwerksprogramm von STRIP," *Schweiz. Beuzeitung*, **90**, No. 3, p. 41, Jan. 10, 1972.

[19] W. D. Whetstone, et al, "SPAR Structural Analysis System Reference Manual (System Level 11)," NASA CR 145098-1, Feb. 1977.

[20] R. J. Allwood and G. M. M. Cornes, "A Polygonal Finite Element for Plate Bending Problems Using the Assumed Stress Approach," *Intern. J. Num. Meth. Engng.*, **1**, p. 135 (1969).

[21] S. T. Mau, P. Tong., and T. H. H. Pian, "Finite Element Solutions for Laminated Thick Plates," *J. Composite Material*, **6**, p. 304, (1972).

[22] T. H. H. Pian and S. T. Mau, "Some Recent Study is Assumed Stress Hybrid Model," *Advances in Computational Methods in Structural Analysis and Designs*, Ed. by J. T. Oden et al, UAH Press, Univ. of Alabama, Huntsville, p. 87 (1972).

[23] B. E. Greene, R. E. Jones, R. W. McLay, and D. R. Strome, "Generalized Variational Principles in the Finite Element Method," *AIAA J.*, **7**, p. 1254 (1969).

[24] E. Anderheggen, "A Conforming Triangular Finite Element Plate Bending Solutions," *Int. J. Num. Meth. Engng.*, **2**, p. 259 (1970).

[25] J. Harvey and S. Kelsey, "Triangular Plate Bending Element with Enforced Compatibility," *AIAA J.*, **9**, p. 1023 (1971).

[26] H. A. Mang and R. H. Gallagher, "A Critical Assessment of the Simplified Hybrid Displacement Method," *Int. J. Num. Meth. Engng.*, **11**, p. 145 (1977).

[27] G. R. Thomas and R. H. Gallagher, "A Triangular Thin Shell Finite Element: Linear Analysis," NASA CR-2482, July 1975.

[28] G. R. Thomas and R. H. Gallagher, "A Triangular Thin Shell Finite Element: Nonlinear Analysis," NASA CR-2483, July 1975.

[29] S. Atluri and T. H. H. Pian, "Finite-Element Analysis of Shells of Revolution by Two Doubly Curved Quadrilateral Elements," *J. Structural Mechanics*, **1**, p. 393 (1973).

[30] F. Kikuchi and Y. Ando, "Application of Simplified Hybrid Displacement Method to Large Deflection Analysis of Elastic-Plastic Plates and Shells," *J. Faculty of Eng., Univ. of Tokyo*, **32**, p. 117 (1973).

[31] A. K. Noor and M. D. Mathers, "Shear-Flexible Finite Element Models of Laminated Composite Plates and Shells," NASA TN D8044, Dec. 1975.

[32] A. K. Noor and C. M. Andersen, "Mixed Isoparametric Finite Element Models of Laminated Composite Shells," *Computer Methods in Appl. Mech. and Engng.*, **11**, p. 255 (1970).

[33] A. K. Noor and S. J. Hartley, "Nonlinear Shell Analysis Via Mixed Isoparametric Elements," *Computer*

and Structures, 7, p. 615 (1977).

[34] O. C. Zienkiewicz and E. Hinton, "Reduced Integration, Function Smoothing, and Non Conformity in Finite Element Analysis (With Special Reference to Thick Plates)," *J. Franklin Inst.*, **302**, Nos. 5 and 6, p. 443 (1976).

[35] S. W. Key, "A Variational Principle for Incompressible and Nearly Incompressible Anisotropic Elasticity," *Int. J. Solids and Structures,* 5, p. 951 (1969).

[36] T. H. H. Pian and S. W. Lee, "Notes on Finite Elements for Nearly Incompressible Materials," *AIAA J.*, **14**, p. 824 (1976).

[37] T. J. R. Hughes, M. Cohen, and M. Haroun, "Reduced and Selective Integration Techniques in the Finite Element Analysis of Plates," to be published in *Nuclear Engng. and Design* (1978).

[38] D. S. Malkus and T. J. R. Hughes, "Mixed Finite Element Methods—Reduced and Selective Integration Techniques, a Unification of Concepts," to be published in *Computer Methods in Applied Mech. and Engng.*, (1978).

[39] S. A. Lee and T. H. H. Pian, "Improvement of Plate and Shell Finite Elements by Mixed Formulations," *AIAA J.*, **16**, p. 29 (1978).

[40] S-T. Mau, T. H. H. Pian, and P. Tong, "Vibration Analysis of laminated Plates and Shells by a Hybrid Stress Element," *AIAA J.*, **11**, p. 1450 (1973).

[41] T. H. H. Pian, "Crack Elements," *Proc. World Congress on Finite Element Methods in Structural Mech.*, J. Robinson Assoc., Bournemouth, Dorset, England, pp. F1–F39, Oct. 12–17, 1975.

[42] P. Tong, T. H. H. Pian, and S. J. Lasry, "A Hybrid-Element Approach to Crack Problems in Plane Elasticity," *Int. J Num. Meth. Engng.*, 7, p. 297 (1973).

[43] T. H. H. Pian, P. Tong, and C. H. Luk, "Elastic Crack Analysis by a Finite Element Hybrid Method," *Proc. 3rd Cong. on Matrix Methods in Structural Mech.*, AFFDL-TR-71-160, pp. 661–682 (Dec. 1973).

[44] S. N. Atluri, A. S. Kobayashi, and M. Nakagaki, "An Assumed Displacement Hybrid Finite Element Model for Linear Fracture Mechanics," *Int. J. of Fracture*, **11**, p. 257 (1975).

[45] O. L. Bowie, "Rectangular Tensile Sheet with Symmetric Edge Cracks," *J. Appl. Mech.*, **31**, p. 208 (1964).

[46] T. H. H. Pian and K. Moriya, "Three-Dimensional Fracture Analysis by Assumed Stress Hybrid Elements," *Num. Methods in Fracture Mech.*, Ed. by A. R. Luxmore and D. R. T. Owen, Univ. College of Swansea, pp. 363–373 (1978).

[47] S. N. Atluri and K. Kathiresan, "An Assumed Displacement Hybrid Finite Element Model for Three-Dimensional Linear Fracture Mechanics Analysis," *Proc. 12th Annual Meeting Soc. of Engng. Sci.*, Univ. of Texas, Austin, pp. 77–87, Oct. 1975.

[48] S. N. Atluri and K. Kathiresan, "On a 3-D 'Singularity Element' for Computation of Combined Mode Stress Intensities," *Advances in Engng. Sci.*, Vol. 1 (13th Annual Meeting Soc. Engng. Sci.), NASA CP-2001, pp. 267–274 (1976).

[49] S. N. Atluri, M. Nakagaki, K. Kathiresan, H. C. Rhee, and W. H. Chen, "Hybrid Finite Element Models for Linear and Nonlinear Fracture Analysis," *Num. Methods in Fracture Mechanics,* Ed. by A. R. Luxmore and D. R. T. Owen, Univ. College of Swansea, pp. 52–66 (1978).

[50] P. Tong, "A Hybrid Crack Element for Rectilinear Anisotropic Materlal," *Int. J. Num. Meth. Engng.*, **11**, p. 377 (1977).

[51] S. N. Atluri and M. Nakagaki, "Post-Yield Analysis of a 3-Point Bend Fracture Test Specimen: An Embedded Singularity Finite Element Incremental Method," *Devel. in Theoretical and Applied Mech.*, Vol. 8, Virginia Polytechnic Inst., Blacksburg, Va., pp. 206–224 (1976).

[52] S. N. Atluri, "On the Hybrid Stress Finite Element Model in the Incremental Analysis of Large Deflection Problems," *Int. J. Solid Structures,* 9, p. 1177 (1973).

[53] G. Herrigmoe and P. G. Bergen, "Incremental Variational Principles and Finite Element Models for Nonlinear Problems," *Computer Methods in Appl. Mech. and Engng.*, 7, p. 201 (1976).

[54] T. H. H. Pian, "Variational Principles for Incremental Finite Element Methods," *J. Franklin Inst.*, **302**, Nos. 5 and 6, p. 473 (1976).

[55] L. D. Hofmelster, G. A. Greenbaum, and D. A. Evensen, "Large Strain, Elastic-Plastic Finite Element Analysis," *AIAA J.*, **9**, p. 1248 (1971).

[56] R. L. Spilker, *A Study of Elastic-Plastic Analysis by the Assumed Stress Hybrid Finite Element Model with Application to Thick Shells of Revolution*, M.I.T. Dept. of Aero. and Astro., Ph.D. Thesis (1974).

[57] P. L. Boland and T. H. H. Pian, "Large Deflection Analysis of Thin Elastic Structures by the Assumed Stress Hybrid Finite Element Method," *Computers and Structures*, **7**, p. 1, (1977).

[58] Th. Scharnhorst and T. H. H. Pian, "Finite Element Analysis of Rubber-Like Material by a Mixed Model," *Int. J. Num. Meth. Engng.*, **12**, p. 665 (1978).

Application of Finite Element Methods to the Analysis of Stresses in Television Picture Tubes

R. E. Enstrom, R. S. Stepleman, and J. R. Appert

RCA Laboratories, Princeton, N.J. 08540

Abstract—The finite element method has been used to calculate the stress distribution and deformation behavior in a 25-inch diagonal television bulb for various design parameter changes, tension-band variations, thermal gradients during processing, and missile impact simulation. In cases where experimental results could be compared with the calculated stress distributions, the agreement was excellent. The calculations show that in a television bulb the critical stress location is on the viewing surface at the top and bottom edges of the picture (screen edge at the end of the minor axis). The tensile stress at this location is reduced by 450 psi as the amount of extra glass at the screen edge (wedge) is increased from 0 to 0.100 inch; is reduced by 75 psi as the centerface thickness is increased from 0.485 to 0.500 inch; is reduced by 40 psi and increased by 90 psi for a bulge or a notch, respectively, at the interior screen edge; is increased by 10 psi for a spun (⅓ thinner) rather than a pressed funnel; is unchanged for a broader funnel than panel seal edge; is reduced by up to 235 psi by offsetting the panel from the funnel seal edge (but this increases the frit seal stress by a factor of 4 to 5 times); is reduced by 150 psi for a tension band positioned near the face; is reduced by about 300 psi for two overlayed tension bands; is increased to about 12,000 psi during UL missile impact testing of an unbanded (nonprotected) bulb; and is reduced to 1200 psi *compressive* stress during heat up in the vacuum bake cycle.

1. Introduction

The finite element method is a powerful tool in the analysis of structures for static stress distributions, dynamic response, heat transfer, and fluid flow, and for interactions between these four parameters. In brief, finite element analysis is a means of subdividing a complex solid continuum into discrete blocks (finite elements) for which mathematical formulas

can be derived that describe their behavior. The aggregate structure is the sum of the properties of these individual blocks (elements) and their interactions. Each solid block can have 8 corners (or nodes) and each node can move in any of three directions (x, y, and z). Accordingly, for an assemblage of 300 elements used to describe a television picture tube, there might be on the order of 1600 simultaneous equations used to describe the response of the tube to atmospheric pressure upon evacuation of the interior of the tube. The solution of this large number of equations requires matrix methods and the use of large scale digital computers.

The power of the method is that it permits the *a priori* estimate of a stress distribution, frequency of vibration, etc., from a descriptive blueprint of the geometry of the structure and the elastic properties of the materials constituting the structure. In this way, many design changes can be made, and the effect of these design changes on the stress distribution can be evaluated before any metal is cut for a mold or a large scale structure assembled.

The basic equations used in the finite element method are given below. Here the forces and displacements are calculated for the element corners, called nodes. A force acting on a node causes a displacement. The set of force–displacement equations for one finite element having n-degrees of freedom is[5]

$$\begin{aligned} F_1 &= k_{11}\Delta_1 + k_{12}\Delta_2 + \ldots + k_{1j}\Delta_j + k_{1n}\Delta_n \\ &\vdots \\ F_i &= k_{i1}\Delta_1 + k_{i2}\Delta_2 + \ldots + k_{ij}\Delta_j = k_{in}\Delta_n \\ &\vdots \\ F_n &= k_{nl}\Delta_1 + k_{n2}\Delta_2 + \ldots + k_{nj}\Delta_j + k_{nn}\Delta_n. \end{aligned} \qquad [1]$$

Here k_{ij} is an element stiffness coefficient and Δ_j is the displacement at the jth node. These nodal forces and displacements are summarized in the element stiffness equation

$$\{F\} = [k]\{\Delta\}, \qquad [2]$$

which represents the array of linear algebraic equations given in Eq. [1]. Here, $[k]$ is the element stiffness matrix (consisting of the material-dependent elastic stiffness matrix, the degree-of-freedom-to-strain transformation, and the stress-to-force transformation). $\{F\}$ and $\{\Delta\}$ are the element force and displacement vectors, respectively. The nodal displacements are the unknowns.

The matrices for the individual elements are next combined to form a complete set of equations for all the elements in the full structure (global) taking into account equilibrium, boundary, and continuity of nodal displacement conditions. This is given as the global stiffness equation,

$$\{P\} = [K]\{\Delta\}, \qquad [3]$$

where $[K]$ is the global stiffness coefficient matrix for all the elements, $\{P\}$ is the vector of global nodal forces (due to the summation of applied loads, atmospheric pressure, etc.) and $\{\Delta\}$ is the vector of nodal point displacements, as before. The general solution to Eq. [3] is obtained by a sophisticated technique for solving systems of linear equations. However, we can think of this symbollically as obtaining the displacement by

$$\{\Delta\} = [K]^{-1}\{P\}. \tag{4}$$

The element stresses are obtained from the displacement by[5]

$$\{\sigma^i\} = [S^i]\{\Delta^i\}, \tag{5}$$

where $\{\sigma^i\}$ is a vector giving the stress at specified points in the ith element, $[S^i]$ is the element stress matrix, and $\{\Delta^i\}$ represents the displacements for the ith element. Δ can consist of as many as three components, u_x, u_y, and u_z expressed as a polynomial expansion in terms of the Cartesian coordinates, x, y, and z.

$$\begin{aligned} u_x &= a_1 + a_2 x \\ u_y &= a_3 + a_4 y \\ u_z &= a_5 + a_6 z. \end{aligned} \tag{6}$$

For the particular isoparametric finite element used in the present calculations (see Sec. 2), the polynomials are[6]

$$\begin{aligned} u_x &= \sum_{i=1}^{8} h_i u_{xi} + h_9\alpha_{x1} + h_{10}\alpha_{x2} + h_{11}\alpha_{x3} \\ u_y &= \sum_{i=1}^{8} h_i u_{yi} + h_9\alpha_{y1} + h_{10}\alpha_{y2} + h_{11}\alpha_{y3} \\ u_z &= \sum_{i=1}^{8} h_i u_{zi} + h_9\alpha_{z1} + h_{10}\alpha_{z2} + h_{11}\alpha_{z3}. \end{aligned} \tag{7}$$

Here α_i is the displacement amplitude and is an additional degree of freedom. The coefficients represent the interpolation functions and are given by

$$\begin{aligned} h_1 &= \frac{1}{8}(1+\xi)(1+\eta)(1+\zeta), \quad h_2 = \frac{1}{8}(1-\xi)(1+\eta)(1+\zeta) \\ h_3 &= \frac{1}{8}(1-\xi)(1-\eta)(1+\zeta), \quad h_4 = \frac{1}{8}(1+\xi)(1-\eta)(1+\zeta) \\ h_5 &= \frac{1}{8}(1+\xi)(1+\eta)(1-\zeta), \quad h_6 = \frac{1}{8}(1-\xi)(1+\eta)(1-\zeta) \\ h_7 &= \frac{1}{8}(1-\xi)(1-\eta)(1-\zeta), \quad h_8 = \frac{1}{8}(1+\xi)(1-\eta)(1-\zeta) \end{aligned} \tag{8}$$

$$h_9 = (1 - \xi^2), \quad h_{10} = (1 - \eta^2),$$
$$h_{11} = (1 - \zeta^2).$$

Here ξ, η, and ζ are nondimensional local coordinates in the range -1 to $+1$. The first eight coefficients are the usual compatible interpolation functions. Coefficients 9, 10, and 11 are the *incompatible* interpolation functions that are related to linear shear and normal strains.[6] These incompatible displacement modes are introduced in improved elements (i.e., isoparametric) to enhance the accuracy by permitting the element edges to bend, as compared to lower-order, constant-strain, compatible elements that cannot bend along the element edges, but can only translate.

Compared with constant-strain elements, the isoparametric element shows a significant improvement in the accuracy of the finite element solution. For example, while a constant-strain element might result in a solution for displacement or bending stress of a cantilever within 30% of the exact solution values, the isoparametric element having incompatible modes results in values virtually identical with the exact solution.[6] Further, in three dimensions, elements having incompatible displacement modes, which improve the element bending characteristics and solution accuracy, have been found to be excellent for the analysis of large structures such as dams and thick pipes.[6] In fact, accurate solutions can be achieved using only a single element to describe the thickness, which significantly reduces the computer time required compared to that using multi-elements through the thickness. A single element is used for the thickness in the present kinescope finite element model.

2. Experimental Procedure

The ANSYS[7] finite element computer program (Revision 2) in conjunction with a Control Data Corporation 7600 computer was used for all of the calculations reported here. The finite element model of the 25 V 90° tube was developed from the blueprints of the standard panel and funnel shown in Figs. 1 and 2. A total of 267 isoparametric three-dimensional elements (ANSYS STIF 45) were used to describe the tube structure. This element has eight nodal points, each having translational degrees of freedom in the x, y, and z directions. As shown in Fig. 1, the vacuum side of the viewing area is spherical and the outside is nonspherical. This geometry results in differing glass thickness in the three principal directions along the tube surface, i.e., the major, minor, and diagonal axes. The funnel has been modeled to represent a pressed glass funnel having an approximate wall thickness of 0.25 inches or a spun-glass funnel having a wall thickness of about 0.170 inches. The frit seal

between the panel and the funnel was modeled as an element 0.010 inches thick by 0.35 inches wide by about 1 inch long.

The Cartesian coordinates for the element nodes were calculated from the radii of curvature specified for a 25 V 90° picture tube (Fig. 1) and these are: inside vacuum surface R = 40.7 inches; outside minor axis R = 44.794 inches; outside major axis R = 42.123 inches; and outside diagonal axis R = 41.704 inches. The panel skirt and funnel node points were determined graphically from full-size blue prints.

The materials properties are given in Table 1. With the input data for the materials properties, the element description, and the Cartesian coordinates for the nodal points, the ANSYS software program was used to generate the element surface stresses, element deflections, and graphical representations of the picture-tube deformation resulting from the action of atmospheric pressure on an evacuated tube. The surface

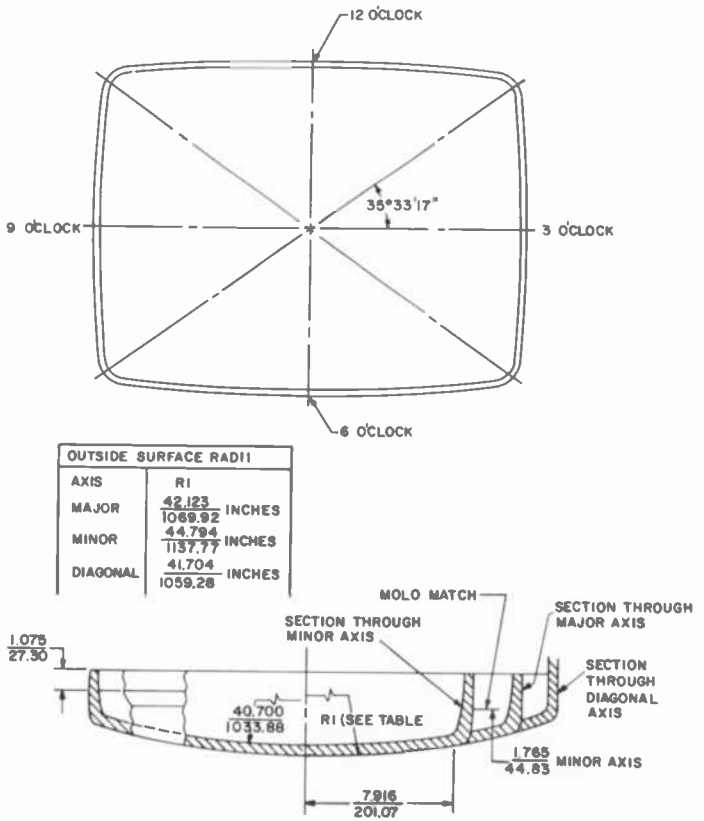

Fig. 1—Top and side views of a standard 25 V 90° panel. Width of seal edge is 0.350 inches. Radii of curvature for inside and outside surfaces are shown.

Table 1—Materials Properties

	Young's Modulus (psi)	Poisson's Ratio	Expansion Coefficient ($°C^{-1}$)	Density (lb. Mass/in^3)
panel & funnel glass	10×10^6	0.223	98.5×10^{-7}	3.03×10^{-3}
frit seal	7×10^6	0.29	97.5×10^{-7}	7.24×10^{-3}

stress printout contains information on the two principal stresses and their directions. In the figures describing the stresses in the various parts of the picture tube, the algebraically largest value of the two principal stresses is reported. *Thus, these figures show the largest compressive or tensile stresses for each element.*

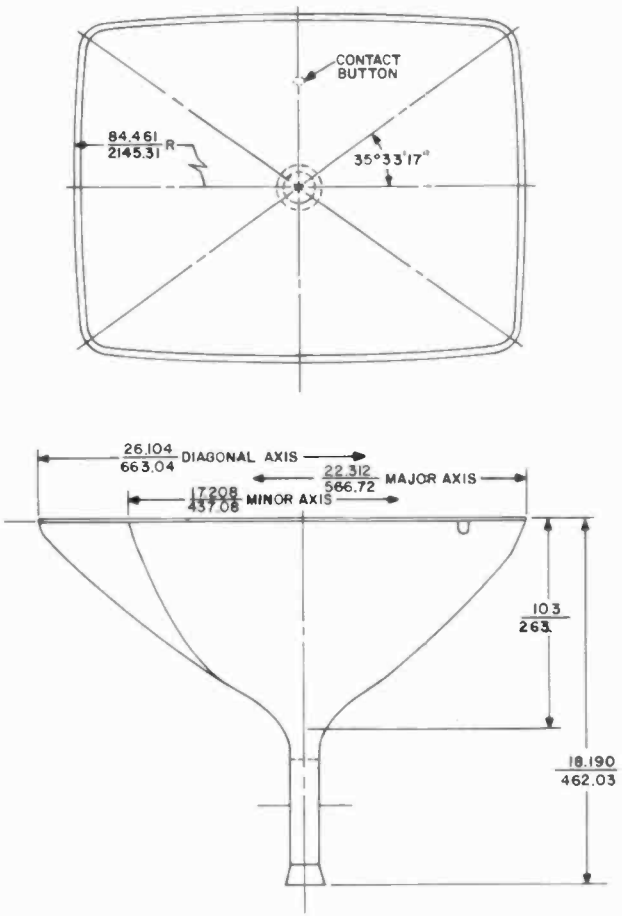

Fig. 2—Top and side views of standard 25 V 90° funnel.

3. Results and Discussion

The stress distribution was calculated for a standard 25 V 90° tube subjected to atmospheric pressure loading. In addition, the effect of other variables on the stress distribution was calculated. These variables included the effect of:

1. varying amounts of glass thickness near the edge of the tube (wedge),
2. altering the center face thickness,
3. altering the blend radius,
4. reducing the funnel thickness,
5. using a broader funnel than panel seal edge,
6. offsetting the panel and funnel seal edges,
7. altering the tension band location,
8. incorporating double tension bands,
9. simulating the Underwriters' Laboratories missile impact test,
10. incorporating thermal gradients (e.g., during tube processing).

These areas are described in detail in the following sections. First, however, the stress distribution calculated for a standard tube is presented.

3.1 Standard 25 V 90° Tube Model

The finite element model for a quarter section of the 25 V 90° panel is shown in Fig. 3. Only a quarter section is needed to describe the panel, since the panel is symmetrical about the major (horizontal) and the minor (vertical) axes as the viewer observes the panel in an operating set. The complete panel can be mathematically simulated by the inclu-

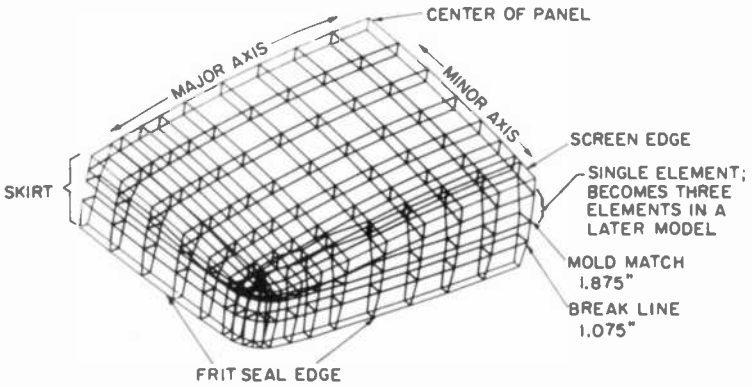

Fig. 3—Finite element model of a one quarter section of a 25 V 90° panel (Run 59B), as viewed from the inside of the tube, showing the element geometry and size.

sion of boundary conditions along the minor and major axes respectively, as $UY = 0$ and $UX = 0$ (which specify no motion in the horizontal and vertical directions). The finite element grid shown in Figs. 3 and 4 is composed of elements of differing sizes. The reason for this is to have a large number of elements in high-stress-gradient locations, and a smaller number in regions where the stress changes only gradually. Such a procedure provides accurate stress calculations at all locations while minimizing the number of elements and, therefore, the computer time/cost of the analysis.

Larger size elements are utilized towards the center of the panel, as shown in Fig. 4. The element size gradually decreases along both the minor and the major axes. At the screen edge, where the viewing surface and the skirt of the panel meet, the element size is about 0.25 inches wide, so that the stress can be accurately calculated in this high-stress-gradient region. The stress gradient along the minor axis will be illustrated in a subsequent figure. Fig. 3 also shows that the panel is a single element thick. It is only by the use of high order *isoparametric* elements (STIF 45 in ANSYS) that accurate stress distributions can be achieved using a single element. Wilson, et al.,[6] have compared plate structures and have shown that results very close to exact solutions can be calculated using a relatively small number of isoparametric elements having incompatible modes. Doubling the number of simpler, constant-strain, elements does not result in comparable accuracy.

It may also be noted in Figs. 3 and 4 that the element shape is close

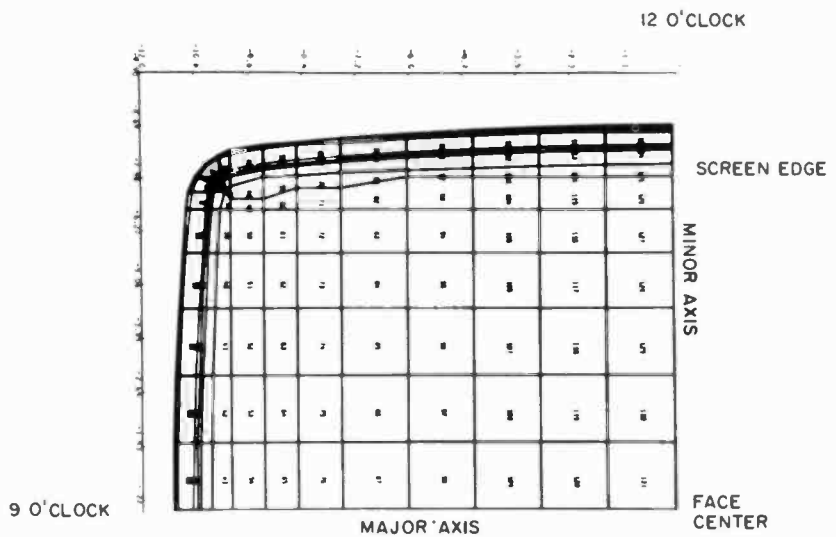

Fig. 4—Top view of a finite element model of a one-quarter section of a 25 V 90° panel.

to rectangular even in the skirt-panel intersection region; this geometry will be shown more clearly in subsequent figures showing sections through the minor axis. To achieve the highest accuracy with these 8-noded solid elements, a well-proportioned aspect ratio should be used. The recently published work of Elst and Wielanger[8] for a 26 V 110° color picture tube showed a similar type of element geometry, which they created independently from our work. Here too, rectangular solids were used in all locations, rather than wedge-shaped sections which might have been used near the screen edge and into the skirt.

Side and end views of the finite element model of the panel and funnel quarter section are shown in Figs. 5 and 6, respectively. The element numbers are shown at the center of each element. The multiplicity of lines outlining the funnel and panel outer periphery results from viewing a curved surface from the side.

In the initial model, the skirt of the panel incorporated three elements, as shown in Fig. 3. However, the one element that described the region between the mold match and the viewing surface, also indicated in Fig. 3, became quite large near the end of the minor axis. Therefore to refine the model of the skirt in this region, the one large element was subdivided into three elements. These three elements, having a notation A, B, C, have principal stresses of 772, 796, and 859 psi tension, respectively, as shown in Fig. 7(a). The arithmetic average for these maximum stresses

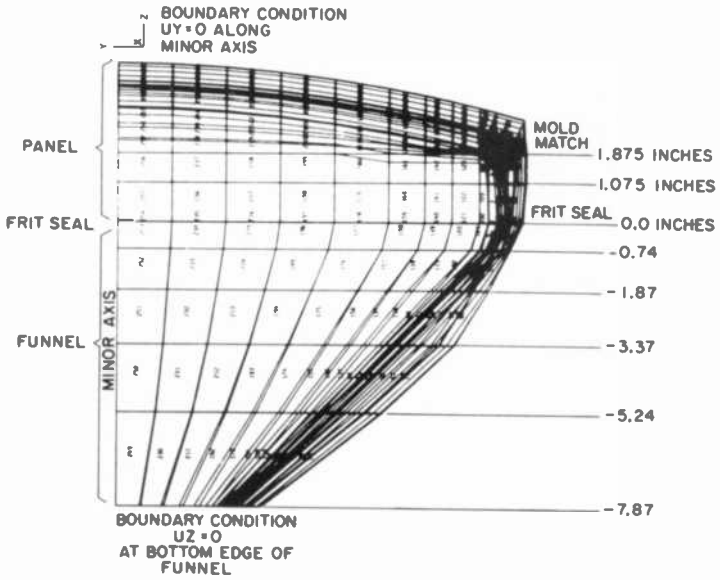

Fig. 5—Side view of a finite element model of a one-quarter section of a 25 V 90° panel and funnel (Run 63C) as viewed parallel to the minor axis.

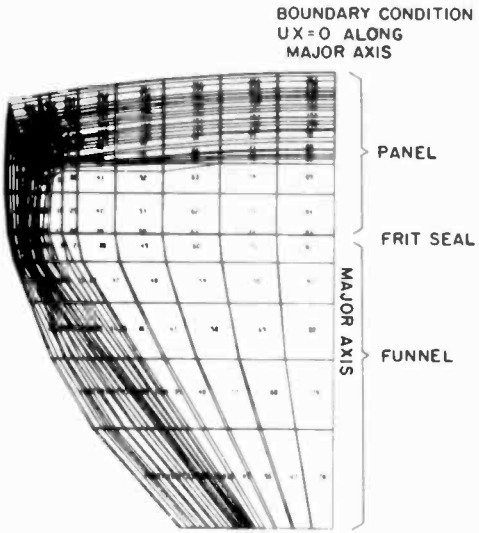

Fig. 6—End view of finite element model of a one-quarter section of a 25 V 90° panel and funnel as viewed parallel to the major axis (Run 63C).

is 809 psi, which compares well with the principal stress of 825 determined for the larger element. This shows that the subdivision better defined the gradient rather than altering it. Everywhere else the stresses are virtually the same in both models.

Next, the lower inner nodes of elements A and B were moved outward by 0.075 and by 0.038 inches, respectively, to reduce the thickness. As shown in Fig. 7(b), the stress is reduced by 25 psi to 1275 psi tension at the screen edge. In elements A, B, and C, the stress is increased somewhat compared to Fig. 7(a). Elsewhere the stresses are virtually unchanged when the skirt model is made thinner (e.g., comparing Figs. 7(a) and (b)).

Fig. 8 shows a comparison between the finite element model cross-section along the minor axis and an actual glass cross-section. Here a good correspondence is seen between the finite element model and the glass structure. Accordingly, we believe that the stresses shown in Fig. 7(b) represent a good approximation to the stress distribution in an actual panel. Because the inside of the panel model does not have a fillet, the calculated stress at the screen edge may be 100 psi higher than for an actual panel having a fillet present.

In Fig. 9, the calculated stress versus distance along the major and minor axes is shown for the atmospheric surface for Run 63C (center face thickness is 0.500 inches). Also plotted are the actual strain-gage-measured stress values,[9] and these are seen to be in excellent agreement with

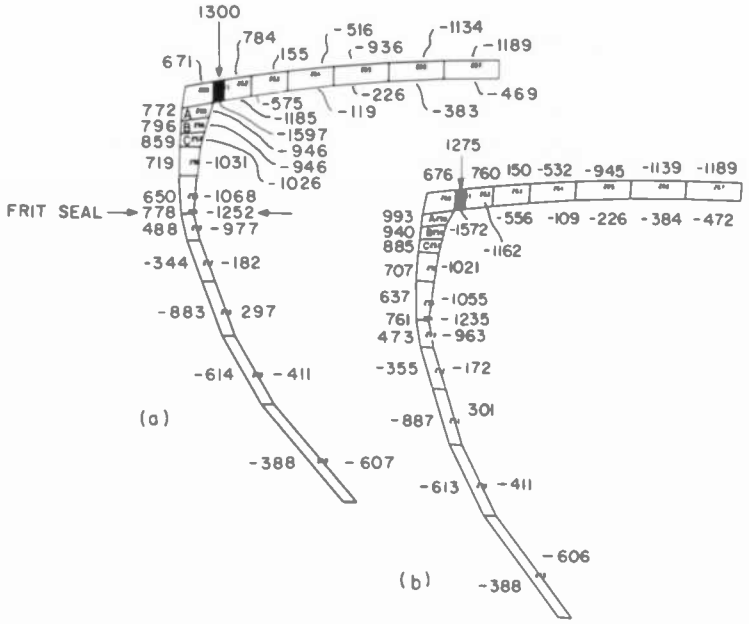

Fig. 7—(a) Cross-section through minor axis of color-tube model having straight inside edges for elements A, B, and C. Negative stresses are compressive and positive stresses are tensile. (b) Cross section through minor axis of color-tube model having a thinner skirt at elements A, B, and C (Deck 63C). Negative stresses are compressive and positive stresses are tensile.

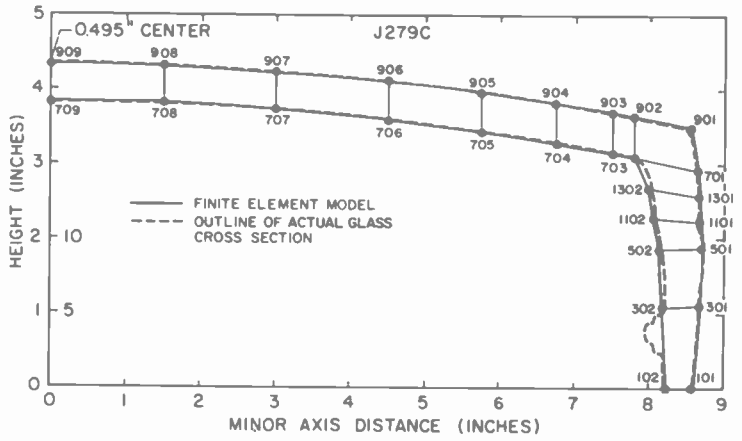

Fig. 8—Comparison of finite element model cross section (Deck 63C) through minor axis with cross section of actual 25 V 90° glass. The finite element nodes are shown and numbered.

the calculated curve. The rapid increase in stress near the screen edge requires that the strain gages be very accurately and reproducibly positioned. A difference in placement of $\frac{1}{8}$ to $\frac{1}{4}$ inch can significantly increase or decrease the observed stress (near the screen edge, $\frac{1}{4}$ inch corresponds to a stress difference of 200 psi).

Both curves in Fig. 9 show the transition from compressive stresses in the center of the panel to tensile stresses toward the edge of the panel. Along the minor axis this occurs at about 6 inches from the face center, while along the major axis the transition occurs about 9 inches from the center of the tube face. A similar type transition occurs for a beam fixed at both ends having an atmospheric pressure load.[10] In both cases, compressive forces are noted near the center portion while tensile stress is present on the top surface near the support point (a wall in the case of the beam and the skirt in the case of the television panel). The more complex panel structure has a stronger dependence of stress on distance than does a simple beam. Comparison of the stress distribution in the two limiting text-book cases of simply supported plates[11] with plates having built-in ends[12] shows that a television panel on a funnel is an in-between condition and, therefore, difficult to calculate using standard text-book type equations. Accordingly, the finite element approach to the calculation of the stress distribution is preferred, because it is not limited to specific boundary conditions. Rather the boundary conditions

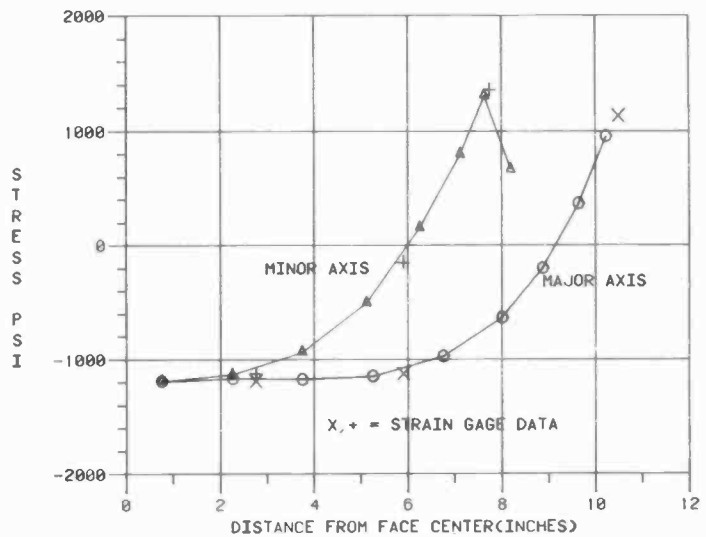

Fig. 9—Comparison of calculated stress with experimentally determined stress along the major and minor axes.

imposed by the geometry and materials properties, as in the real structure, are the ones that are operative.

The ANSYS calculated stresses and experimentally determined values are compared in Fig. 10. Here it may be seen that tensile stresses are present in the panel skirt, the frit seal, and the adjacent region of the funnel. The lower portion of the funnel exhibits only compressive stresses. The frit seal is important because it joins the panel and the funnel parts together to form the complete bulb. It is important that stresses be kept low in this region, since the frit material after firing is not as strong as the parent glass. In later sections the effect of offset between the panel and funnel mating surfaces on the frit seal stresses will be discussed.

The stresses present over the viewing area (in quarter symmetry), resulting from the atmospheric pressure acting on the evacuated bulb, are shown in Fig. 11 for the outside surface and in Fig. 12 for the vacuum side. The stresses shown for the minor axis cross-section in Fig. 7(b) are the same as along the minor axis in Figs. 11 and 12. The high-stress region along the screen edge extends from the minor axis to the corner to the major axis. This high-stress region in a tube is a very critical location and may be a cause of failure of the tube. Accordingly, it is particularly important that this region not be subject to extraordinarily high stresses resulting from the glass fabrication or mounting the tube in the cabinet. While glass is strong in compression, it is very weak in tension. Further

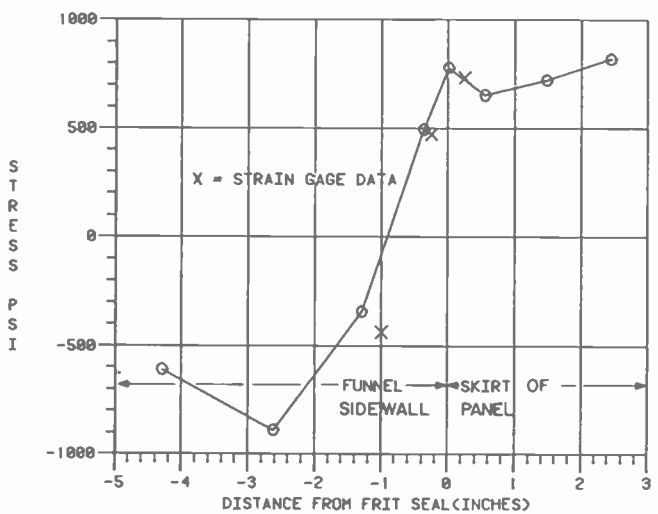

Fig. 10—Comparison of calculated stresses with experimentally determined stresses in the skirt and funnel along the minor axis.

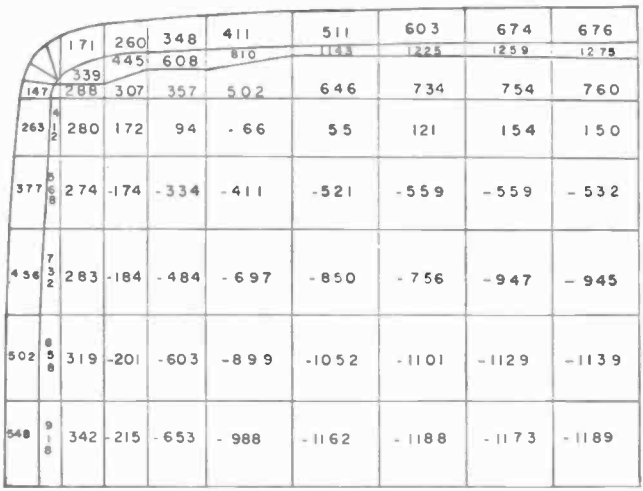

		171	260	348	411	511	603	674	676
			445	608	810	1143	1225	1259	1275
		339							
147		288	307	357	502	646	734	754	760
263	4 1/2	280	172	94	-66	55	121	154	150
377	5 5/8	274	-174	-334	-411	-521	-559	-559	-532
436	7 3/2	283	-184	-484	-697	-850	-756	-947	-945
502	8 5/8	319	-201	-603	-899	-1052	-1101	-1129	-1139
548	9 1/8	342	-215	-653	-988	-1162	-1188	-1173	-1189

Fig. 11—Stresses present on the atmospheric side of the viewing surface resulting from atmospheric pressure (63C). Note the high stress region along the screen edge. Negative stress are compressive and positive stresses are tensile.

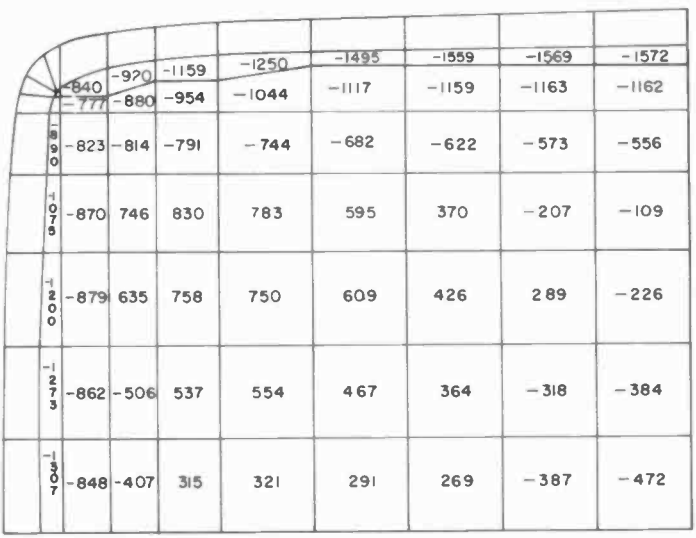

					-1250	-1495	-1559	-1569	-1572
		-840	-920	-1159		-1117	-1159	-1163	-1162
		-777	-880	-954	-1044				
890		-823	-814	-791	-744	-682	-622	-573	-556
1075		-870	746	830	783	595	370	-207	-109
1200		-879	635	758	750	609	426	289	-226
1273		-862	-506	537	554	467	364	-318	-384
1307		-848	-407	315	321	291	269	-387	-472

Fig. 12—Stresses present on the vacuum side of the viewing surface resulting from atmospheric pressure (Deck 63C). Negative stresses are compressive and positive stresses are tensile.

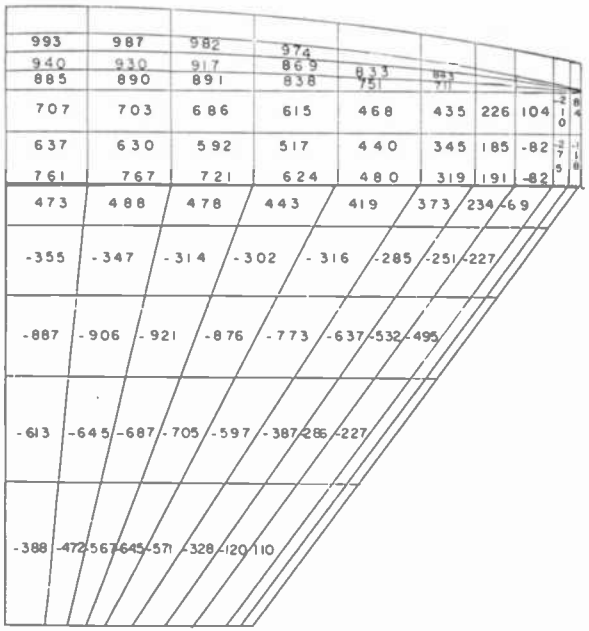

Fig. 13—Stresses present on the atmospheric side of the skirt and funnel as viewed parallel to the minor axis (63C).

it is subject to failure by a stress corrosion mechanism whereby water vapor in the air reacts with the glass at high tensile stress locations to cause premature failure. This failure mechanism is time dependent, so that the actual failure can occur some time after a surface defect has been initiated. Later sections discuss in more detail the effect of geometric changes in the glass thickness near the screen edge on the tensile stress in this location. The stresses at the screen edge on the vacuum side are all compressive and thus of no concern even though the magnitude of the stress can range up to nearly 1600 psi, as seen in Fig. 12.

The stress distribution on the skirt and funnel is shown for the atmospheric surface in Figs. 13 and 14 when viewed parallel to the minor and major axes, respectively. In Fig. 13, the tensile stresses in the skirt are seen to decrease as one proceeds in the direction of the tube corner from the end of the minor axis. Similarly, in Fig. 14, these tensile stresses are highest at the major axis and decrease towards the tube corner. In the funnel, the stresses are mainly compressive and therefore of not too much consequence, except near the frit seal. It should be pointed out that Figs. 13 and 14 refer to a pressed funnel. In a later section, results will be presented for the stress distribution in a thinner, spun-type funnel.

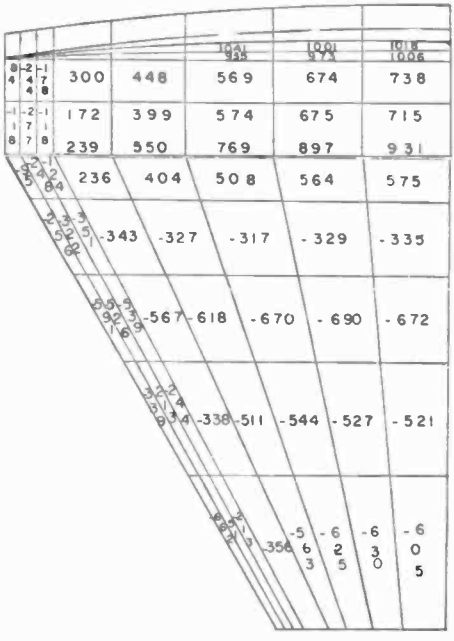

Fig. 14—Stresses present on the atmospheric side of the skirt and funnel as viewed parallel to the major axis (63C).

The stresses on the vacuum surface for the tube are shown in Figs. 15 and 16. Here, the stresses are virtually all compressive on both the skirt and funnel surfaces. These figures illustrate another advantage of the finite element analysis, i.e., that stresses can be calculated for regions, such as the inside of the tube, that are difficult to measure with strain gages.

In addition to stress distributions, the displacement of the structure under the action of the atmospheric pressure load can be calculated. In Fig. 17 the displacement calculated for atmospheric pressure acting on an evacuated bulb is illustrated. Here the center of the tube is calculated to move inward by 0.007 inches. The inward movement of the face in turn counteracts the atmospheric pressure acting on the skirt, with the result that a net outward movement of the skirt is observed. Below the frit-seal region, the action of the atmospheric pressure causes a new inward movement of the funnel, leading to a general compressive state of stress in this region. It should be pointed out here that the deformation and stresses shown in the previous series of figures represent the response of the tube only to atmospheric pressure. The effects of implosion protection bands on the response of the tubes will be illustrated later.

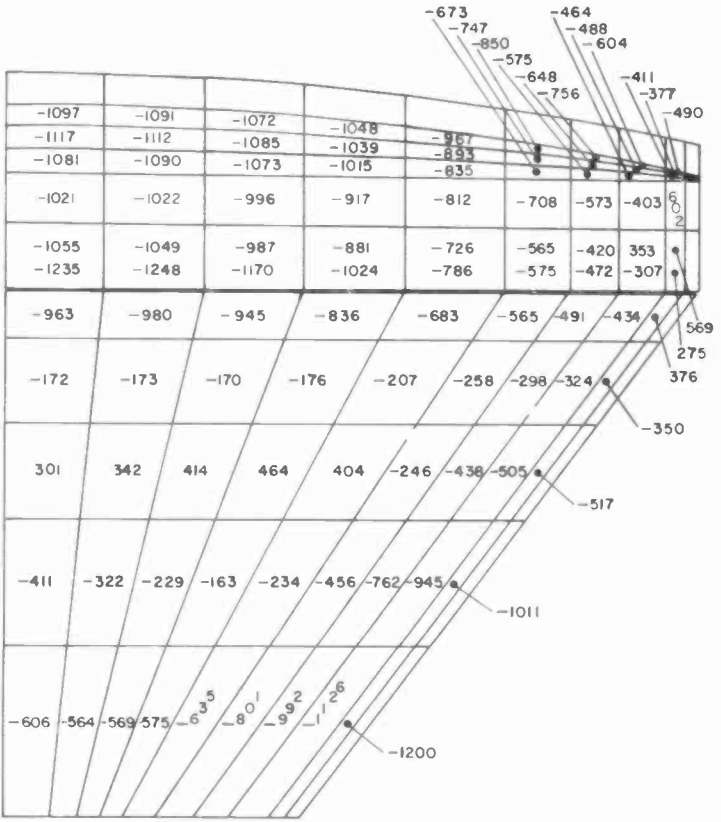

Fig. 15—Stresses present on the vacuum side of the skirt and funnel as viewed parallel to the minor axis (63C).

3.2 Effect of Wedge on Stresses

In the previous section, the wedge at the screen edge was determined by the difference of the inside and outside radii of curvature of the tube face. To try to help understand the effect of wedge (the difference in thickness at the screen edge compared to the thickness at the center of the tube face) at the minor and major axis screen edges, a standard 25 V 90° finite element model was modified to have 0, 0.050 and 0.100 inches of additional glass thickness at the screen edge. This was accomplished by keeping the inside of the viewing surface fixed at a radius of 40.7 inches while using three different *spherical* radii of curvature for the outer surface, as given in Table 2.

Since the outside surface was treated as spherically symmetric, there will be greater wedge at the ends of the major and diagonal axes than is

Table 2—Dimensions for 25V 90° Panels Having Various Amounts of Wedge

Computer Run	Inside Radius of Curvature (inches)	Outside Radius of Curvature (inches)	Wedge at Minor Axis Screen Edge* (inches)
61B	40.7	40.7	0.0
61D	40.7	43.792	0.050
61E	40.7	47.37	0.100
59C	40.7	44.794 Minor 42.123 Major 41.704 Diagonal	0.065 0.044

* 7.57 inches from face center

shown for the minor axis. For comparison, the radii of curvature for the present 25 V 90° panel are given in Table 2; here the outside surface is not spherical, which produces less wedge at the end of the major axis where the stress is lower than at the end of the minor axis. In a second type of industry-standard panel, the inside surface is pressed to a non-spherical shape and the outside viewing surface is polished to a spherical curvature. The thickness at the center of the viewing surface for the

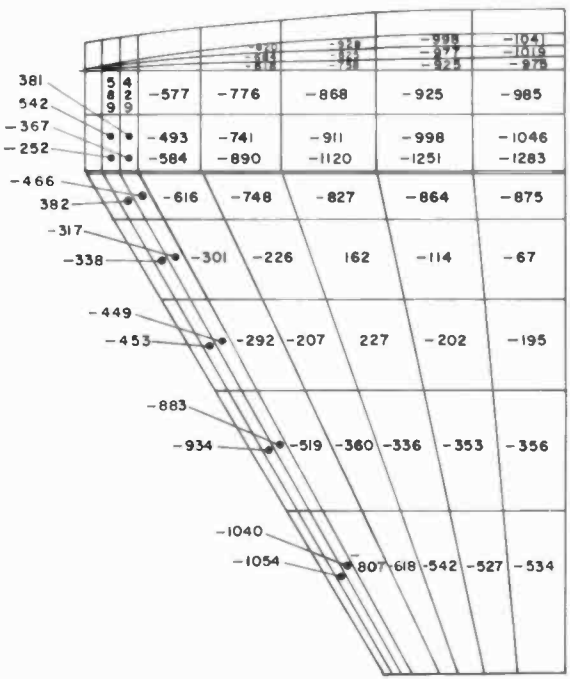

Fig. 16—Stresses present on the vacuum side of the skirt and funnel as viewed parallel to the major axis (63C).

Table 3—Results of ANSYS Computer Calculations for Stress at the Minor Axis Screen Edge

Computer Run	Wedge (inches)	Thickness at Screen Edge (inches)	Stress (psi)	Reduction of Stress (psi)	Stress in Frit Seal (psi)
61B	0.0	0.485	1610	0	734
61D	0.050	0.539	1360	250	770
61E	0.100	0.593	1168	442	793
59C	0.065	0.555	1379		775

above models was taken as 0.485 inches; for the previously shown results on Run 63C the panel thickness is 0.500 inches at face center.

The results of the ANSYS calculations are given in Table 3 for the critical area at the minor axis screen edge. More detailed data are presented in Fig. 18(a)–(c), which shows the stresses existing on both the vacuum side and atmospheric surface along the minor axis for tubes having 0.0, 0.050, and 0.100 inches of wedge, respectively. Comparison of the data in the figure suggests that differing amounts of wedge affect principally the tensile stresses at the screen edge. At this location, the stress decreases from 1610 to 1360 and then to 1168 psi as the wedge is increased from 0.0 to 0.050 and then to 0.100 inches, respectively. The dependence of the decrease in stress with increasing wedge is shown in Fig. 19. Here, the tensile stress at the screen edge is seen to decrease nearly linearly with increasing wedge. Accordingly, if strain gage mea-

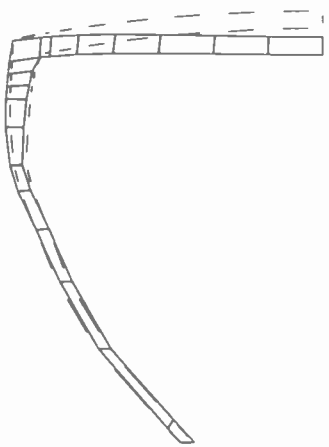

Fig. 17—Section of the color tube model through the minor axis showing the displacement calculated for atmospheric pressure acting on an evacuated bulb. The dotted line indicates the original undeformed structure. The maximum deformation at the center is 0.007 inches.

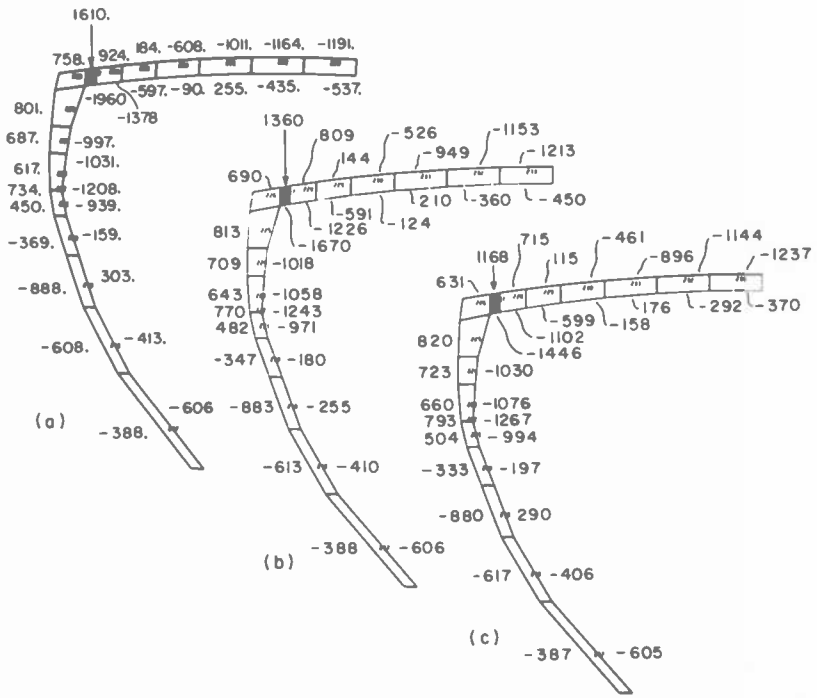

Fig. 18—Cross-section of a 25 V 90° tube (a) having a 0.485 inch center face thickness and no wedge at the minor axis screen edge (61B), (b) having a 0.485 inch center face thickness and 0.050 inches of wedge at the minor axis screen edge (61D), and (c) having a 0.485 inch center face thickness and 0.100 inches of wedge at the minor axis screen edge (61E).

surements showed higher than desired stress at the screen edge on a particular batch of tubes, the stress could be reduced significantly by building in additional wedge during the glass forming operation, or by removing less glass during the face polishing operation.

Finally, it should be noted that decreasing the stress at the screen edge by increasing the wedge makes the panel surface stiffer. This greater stiffness then tends to increase the stress in the skirt and in the frit seal. However, the increase in stress in the frit-seal region from 734 to 793 psi as the wedge increases from 0.0 to 0.1 inches is fortunately much less than the reduction in stress at the screen edge (440 psi).

3.3 Effect of Center Face Thickness on Stress

The results described above were calculations for panels having a center face thickness of 0.485 inches. This value represents the design standard thickness. Indeed, a preferable panel thickness may be 0.500

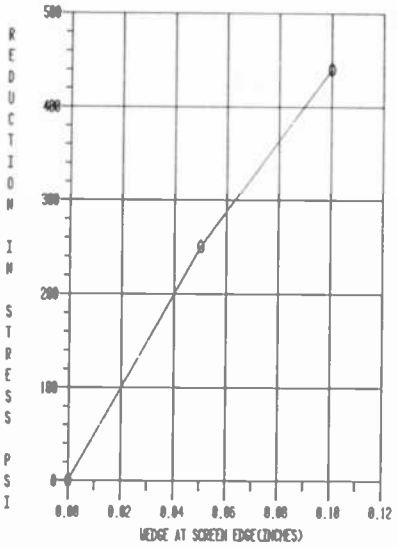

Fig. 19—Reduction in tensile stress at the minor axis screen edge as a function of wedge for a 25 V 90° panel on a pressed funnel. Both the atmospheric and vacuum viewing surfaces of the panel are spherically symmetric.

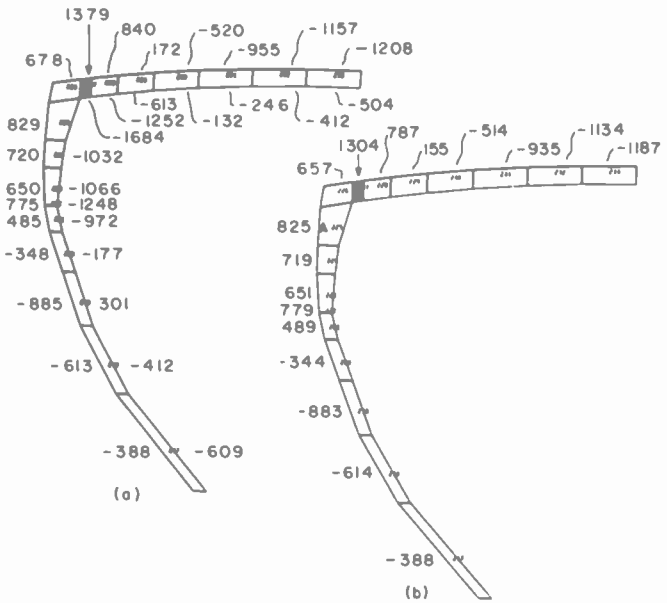

Fig. 20—Minor axis cross-section showing stresses present in tubes having (a) 0.485 inch and (b) 0.500 inch center face thicknesses (59HH).

Table 4—Comparison of Stresses at the Minor Axis Screen Edge for 0.485 and 0.500 Inch Centerface Panels

Computer Run	Centerface Thickness (inches)	Stress (psi)	Increased Thickness (inches)	Reduction in Stress (psi)
59C	0.485	1379	0	0
59HH	0.500	1304	0.015	75

inches. To make the comparison for the effect of center face thickness, the same finite element model was used and only the coordinates for the outer surface were changed. The same internal and external radii of curvature were used. The calculated stresses for the 0.485- and 0.500-inch thick panels are shown in Fig. 20. Here, the stress at the minor axis screen edge is reduced to 1304 psi (0.500 inches) from the value of 1379 psi observed for the 0.485 inch panel. Stresses at other locations on the face are also reduced, but by an increasingly smaller amount proceeding toward the center. The stresses in the funnel and skirt are virtually unchanged as the panel thickness increases (by .015 inches uniformly), in contrast to the greater skirt stresses observed in Figs. 18(a)–(c) when the wedge was increased. These results are summarized in Table 4.

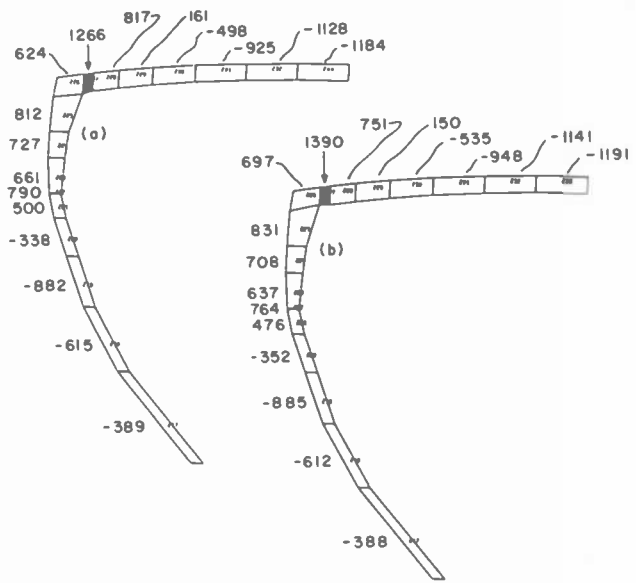

Fig. 21—Minor axis cross-sections showing stresses present in 0.500 inch center face thickness tubes having (a) a bulge or (b) a notch at the screen edge.

Table 5—Comparison of Stresses at the Minor Axis Screen Edge for Panels Having Local Increased or Decreased Thickness at this Location. Both Panels have a 0.500 Inch Centerface Thickness

Computer Run	Screen Edge Thickness (inches)	Stress (psi)	Change in Thickness (inches)	Change in Stress (psi)
62CH	0.520	1390	−0.050	+86
59HH	0.570	1304	0	0
62DH	0.620	1266	+0.050	−38

3.4 Effect of Blend Radius Geometry on Stress

The thickness of glass at the screen edge was varied to determine the effect on the stress of a localized notch or bulge at the transition region between the panel face and the panel skirt. This was done by decreasing (Run 62CH) or increasing (62DH) the Z-component of the Cartesian coordinates of all elements at the screen edge by 0.050 inches. The effects of these changes are shown in Fig. 21 and Table 5. The presence of a notch is seen to increase the stress to 1390 psi, while having additional glass at the transition region reduces the stress to 1266 psi. Calculations for the standard-design are also shown in Table 5.

In Table 5, it may be seen that the effect of having a decreased glass thickness at the screen edge increases the tensile stress by 86 psi. By comparison, increasing the thickness by 0.050 inches reduces the stress by only 38 psi. These results therefore emphasize the deleterious effects on the stress of having a notch in the region of the screen edge, compared to the smoother transition region of the standard panel design shown in Fig. 20.

3.5 Effect of a Reduced Funnel Thickness on Stress

A spun funnel is only about two thirds as thick as a pressed funnel. To determine the effect of a thinner funnel on the stress distribution, the previously-used pressed funnel model was reduced in thickness by $\frac{1}{3}$. The same standard panel was used as on the pressed funnel (Run 63C) described in the initial series of figures. The stress distribution for this bulb is shown in Fig. 22. Comparison with Fig. 7(b) shows that the stress at the screen edge is increased slightly to 1282 psi, compared to 1275 psi for the pressed funnel having the same panel. The stresses in the frit seal are increased to 910 psi, compared to 761 psi for the pressed funnel. The stresses in the thinner funnel are about 200 psi higher than in the pressed funnel.

The calculated stress distribution in the panel is compared with the

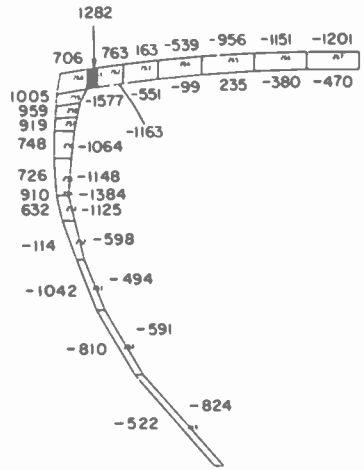

Fig. 22—Minor axis cross-section showing the stresses present in a standard panel on a thinner, spun-type funnel.

Table 6—Comparison of Calculated and Observed Principal Stresses in a Bulb having a thinner, spun-type funnel.

	Location on Panel	Calculated Stress 1 (psi)	Stress 2 (psi)	Distance (Inches)	Observed Stress 1 (psi)	Stress 2 (psi)	Distance (Inches)
1	Face Center (Vacuum Side)	−470	282	0	−478	319	0
2	Minor Axis	−380	301	2.3	−332	352	2.6
3	Major Axis	−378	279	2.3	−280	201	2.6
4	Major Axis	336	−15		388	89	6.8
5	Diagonal Axis	623	−272	6.4	687	−170	6.8
6	Major Axis	529	906	Screen Edge	638	912	Screen Edge
7	Major Axis	209	−1429	Inside Frit Seal	−59	−1212	Inside Seal Edge
8	Diagonal Axis	379	−103	Corner	408	−50	Corner
9	Minor Axis	1282	764	Screen Edge	1158	909	Screen Edge
10	Minor axis	−1384	−262	Inside Frit Seal	−1444	−26	Inside Seal Edge

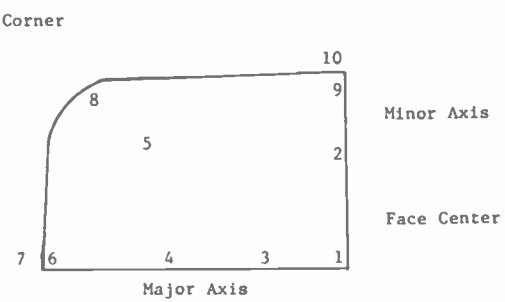

experimentally measured stress distribution in Table 6. In this Table, both principal stresses at each location have been included to indicate the degree of agreement. As can be seen, the values for the ANSYS calculated stresses and the strain-gage-measured stresses are in excellent agreement. This agreement further corroborates the accuracy and usefulness of the finite element method when a good model and a high order isoparametric element are used.

3.6 Effect of a Broad Seal Edge on Stress

In older-design funnels, the seal edge of the funnel was made deliberately wider than the panel seal edge to allow for manufacturing variability. In this way, the panel seal edge would always continuously contact the funnel seal edge even though the difference in interior dimensions may be 0.050 inches or more. The effect of one-sided seal-edge offset is considered in a later section.

The case of a wider-funnel seal edge was modeled by making the funnel 0.45 inches wide at the seal edge and tapering into the standard pressed-funnel model dimensions about 3 inches below the seal edge. The width of the panel seal edge is 0.35 inches. The frit seal material joined the panel and the funnel as shown in the inset to Fig. 23. Comparison of Fig. 23 with the standard bulb in Fig. 7(b) shows that the presence of the wider funnel seal edge does not appreciably alter the

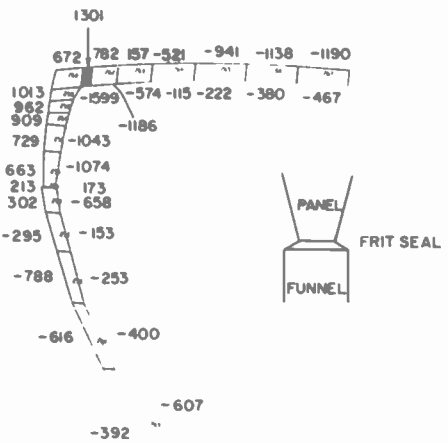

Fig. 23—Minor axis cross-section for a bulb having a 0.45 inch funnel and 0.35 inch panel seal edge. The centerface thickness is 0.500 inches. The inset shows the geometry of the seal edge.

stress distribution (by more than 25 psi) except in the region of the frit seal. The stresses are reduced in the frit seal and in the thickened region of the funnel presumably because of the larger cross-sectional area.

Thus, the principal advantage of the wider-funnel seal edge is the greater dimensional freedom it allows while assuring complete contact of the funnel and panel seal edges. In this way, manufacturability should be increased. Of course, the penalty is slightly increased weight of the funnel.

3.7 Effect of Offset Seal Edges on Stress

The effect of offsetting equally-wide (both are 0.35 inches) panel and funnel seal edges by 0.060 inches, is illustrated in Fig. 24. Here the stress in the frit seal increases to tensile values of 4216 psi for the funnel offset outward from the panel and to 3301 psi for the funnel offset inward from the panel edge. Needless to say, the magnitude is sufficiently high to be of concern. These high stresses could cause fracture of the weaker frit-seal material. Indeed, the frit seal has been observed to fail during the

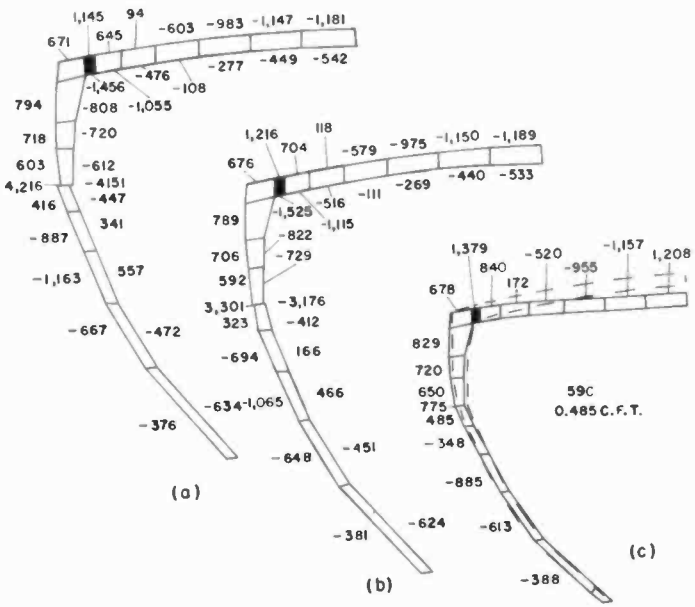

Fig. 24—Minor axis cross-sections of bulbs having a funnel that is displaced (a) outward or (b) inward by 0.060 inches relative to the panel. The standard bulb is shown in (c).

exhaust bake cycle (the bulb is first evacuated here) in some mismatched-seal-edge bulbs, confirming the high stresses calculated for the frit seal. Accordingly, it is of great importance that the seal edges be well matched to avoid failures during processing or at some later date.

As may be seen upon comparing the stress distributions for (a) and (b) in Fig. 24, the effect of a 0.060 inch inward or outward displacement of the funnel relative to the panel also changes the stresses at the screen edge. For comparison, a bulb having matched seal edges is shown in Fig. 24(c). Here the stress is 1379 psi at the screen edge and 775 psi at the frit seal. Thus, the outward displacement of the funnel reduces the screen-edge stress by 235 psi and the inward displacement reduces the stress by 160 psi. This reduction in stress comes about presumably because the funnel through the frit does not exert as great a downward and lateral restraint to the panel skirt as when the seal edges are matched. While the reduction in screen-edge stress is a desirable objective, achieving it by offsetting the seal edges is not an acceptable means, since the frit-seal stress is increased by a factor of 4 to 5 times compared to the matched case.

3.8 Effect of Tension Band Location on Stress

In one form of integral implosion protection, a steel tension band is placed around the skirt of the bulb after evacuation and final processing. Between this tension band and the glass is a steel rim band. During application of the tension band, it is pulled to about 1200 pounds force and then mechanically clamped together. The tension band is $\frac{5}{8}$ inches wide, 0.025 inches thick, made from high tensile strength steel, and is quite stiff. Accordingly, it does not apply a uniform force to the skirt periphery, but rather concentrates the inward-directed force at the corners. Therefore the action of the tension band was modeled by applying all of the force over three elements at the rounded portion of the panel corner. Axially, the location of the band can be adjusted from near the frit seal to near the viewing surface.

The effect of tension band placement on the calculated stress distribution is shown in Fig. 25. The inset on the right in the figure indicates the band position on the panel corner; near the face for band position between 3 and 2, and near the frit seal for band position between 2 and 1. The stresses for a band position near the face, Fig. 25(a) are generally lower than for a band positioned near the frit seal, Fig. 25(b). In particular, at the screen edge the stress is about 150 psi lower for the band placed near the face. This reduction in stress at the screen edge thereby provides an additional margin of safety against failure at the screen edge.

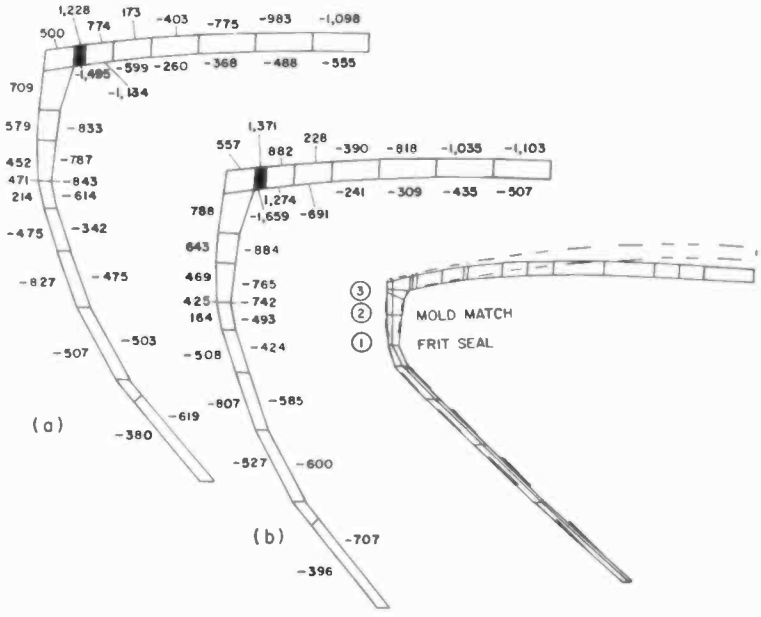

Fig. 25—Minor axis cross-sections of bulbs having (a) tension band between the face and the mold match, i.e., between 3 and 2 on the inset, and (b) tension band between the frit seal and the mold match, i.e., between 1 and 2 on the inset.

The stresses for a comparable unbanded tube were presented in Fig. 24(c). The screen-edge stress for the tube having the band near the frit seal is nearly identical to the unbanded tube. Accordingly, bands placed near the face appear to be preferable. Comparison with the unbanded tube also shows that banding reduces the stresses in the skirt, frit seal, and funnel by 200–300 psi, which is also desirable. But, stresses in the skirt and frit seal at the corner can be higher.

Finally, comparison of the displacement at the face center shows that the face moves inward about 0.002 inches less for the banded tube than for the unbanded one. This calculated difference agrees very well with values observed for actual tubes.[9]

3.9 Effect of Double Tension Bands on Stress

Another form of internal implosion protection utilizes two overlayed tension bands while omitting the rim band. In this version the bands are applied forward of the panel mold match near the viewing surface. Each band is tensioned to 1350 ± 150 pounds force. The cumulative effect of both bands is estimated to be 2250 pounds force (two times 1350 less

relaxation after the bands are clamped). Differences have been found between the implosion characteristics of bulbs having pressed versus the thinner spun funnels protected with double tension bands. In the Underwriters' Laboratory test, the thicker pressed funnel bulb has a satisfactory glass throw for a deliberately induced implosion, while the spun funnel bulb, as it presently is protected, does not meet the glass throw criteria. Accordingly, both a pressed and a spun-type funnel were modeled and compared to determine if the static stress distributions are different and whether this difference might explain the dynamic differences.

The static stress distributions calculated for the pressed and for the spun-type funnel are shown in Fig. 26 (A) and (B), respectively. These results may be compared with the nonbanded bulb in Fig. 7(c). Here we see that the stress at the screen edge is *reduced* by about 300 psi in both cases to about 960 psi. This effect is very beneficial in that by reducing the stress at the screen edge, it minimizes the deleterious effects of water-vapor-related stress corrosion on the safety of the tube.

The difference in the tensile stress distribution between the pressed and the spun funnels is about 30 psi on the face, a relatively small value,

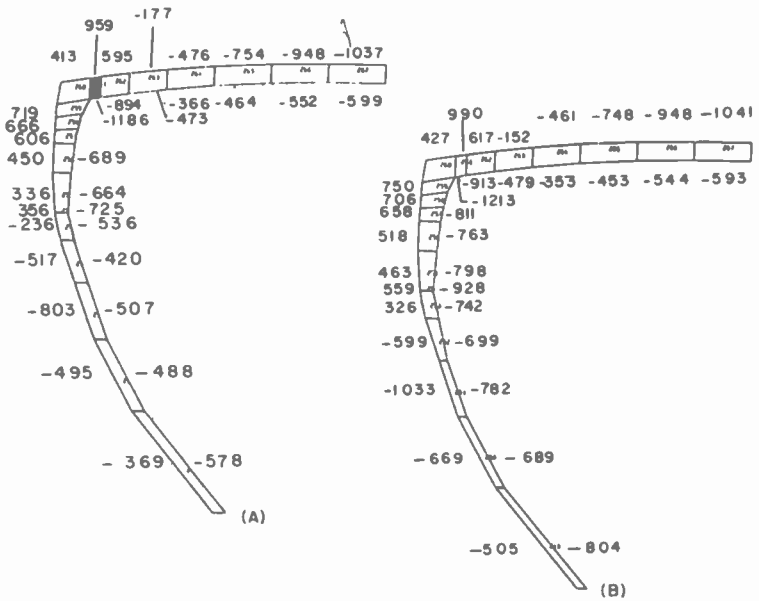

Fig. 26—Minor axis cross-sections for double tension bands on (A) pressed funnel and (B) spun, thinner funnel.

and about 200 psi in the frit seal region. In spite of the higher tensile stresses in the spun-type funnel, the frit seal, funnel, and skirt are not unduly stressed. Accordingly, since it appears that the static stress distribution is the same in both funnel types, differences noted in glass throw must be related to the dynamic behavior of the glass from the spun and pressed funnel bulbs.

3.10 Effect of Impact of the UL Missile on Stresses

In the Underwriters' test for glass throw upon implosion, a missile impacts the face of the screen with 15 foot-pounds of energy. To determine the effect of this impact on the stress distribution prior to rupture of the glass, the dynamic impact was approximated by a 7000 pound static force.[13] To determine the effect of impact on the glass itself, the bulb did not have an implosion protection band, as would ordinarily be present on a commercial tube.

The results of this calculation are shown in Fig. 27. Very high tensile stresses are shown to be present on the vacuum side of the tube near the point of impact (20,719 psi), along the atmospheric surface screen edge

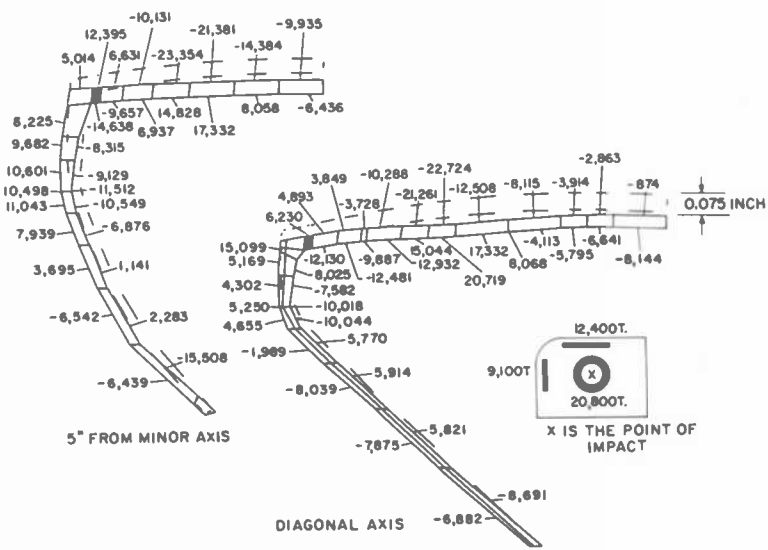

Fig. 27—Cross-sections through the minor axis 5 inches from face center (left) and through the diagonal axis (right) showing the stresses generated from a static force of 7,000 pounds. The inset shows the position of high tensile stresses on the tube face.

(up to 12,400 psi), and on the atmospheric surface of the skirt and frit seal region (up to 11,000 psi).* Thus, the calculation shows that several other high stress areas exist in addition to the point of impact. In turn, fracture during implosion testing is observed to occur at several locations, such as the screen edge, although the main fracture initially is the point of impact. At times, failure occurs in the funnel. The high tensile stresses generated by the impact cause a crack to be formed and this crack readily propagates in the tensile stress region. The atmospheric pressure opens up the crack, and complete failure then occurs.

The elastic deformation at the point of impact is about 0.075 inches as shown on the inset to Fig. 27. Simultaneously the frit-seal region moves outward 0.025 inches at the end of the minor axis and 0.015 inches at the end of the major axis. The deformation at the several locations is indicated by the difference between the original contour without atmospheric force or impact force, shown as a dotted line, and that for the deformed structure responding to the atmospheric and 7000-pound-impact force.

The exact correspondence of a 15 foot-pound impact and its static-force equivalent depends on a number of factors that are not unambiguous. Thus while one calculation gives 7000 pounds,[13] other calculations indicate that the force may be as high as 23,000 pounds.[14] In the latter case, the tensile stress around the point of impact would be very much higher than 20,000 psi and could be as high as 70,000 psi. It should be pointed out that the stresses indicated in Fig. 27 are *not* directly under the point of impact, but are the average value at a distance of about ¾ inch. Stresses at the point of impact would be much higher than the 20,000 or 70,000 psi discussed here. The present calculations are not intended to determine the highest stress at the point of impact, but rather to determine the location of high stress points all over the tube. To determine the value of the stress at the point of impact, a much smaller element size, perhaps as small as 0.050 inches on a side, should be used to resolve the stress in this high gradient region. Such a model has been used for the analysis of stresses in silicon wafers loaded with a point load at the center.[15]

A further refinement of the finite element calculation would be to determine the stress distribution when an implosion protection band is present. In this case, though, a simple approximation of the resultant force from the band acting on the diagonal axis corner could not be used, since the frit-seal region and skirt moves outward very significantly. Rather, a finite element model of the band, its position, and its applied

* Another calculation using stiff boundary conditions $UX = UY = UZ = 0$ to isolate the quarter symmetry section gives similarly high stresses at these locations.

load would have to be developed. The loaded tension band then would interact with the UL impact-simulating load on the face to restrict skirt and face movement. In this way the tensile stress region in the glass would be reduced, and glass fracture would not be be so catastrophic.

3.11 Effect of Thermal Gradients on the Stress Distribution

In the sections treated so far, the action of atmospheric pressure, band forces, and impact forces on tubes having various geometries has been examined. In this section we consider the effect of thermal gradients, such as might be developed during a high-temperature bake of the tube while it is being simultaneously evacuated. For these calculations, experimental values of the temperatures existing on the atmospheric and vacuum surfaces at about 50 locations[16] during the exhaust bake cycle were interpolated using a Lagrangian routine on a Hewlett-Packard 97 calculator for each of the 530 node points. The temperature at the center of the face was 350°C on the atmospheric side and about 312°C on the vacuum side. The gradient on both sides going towards the minor axis

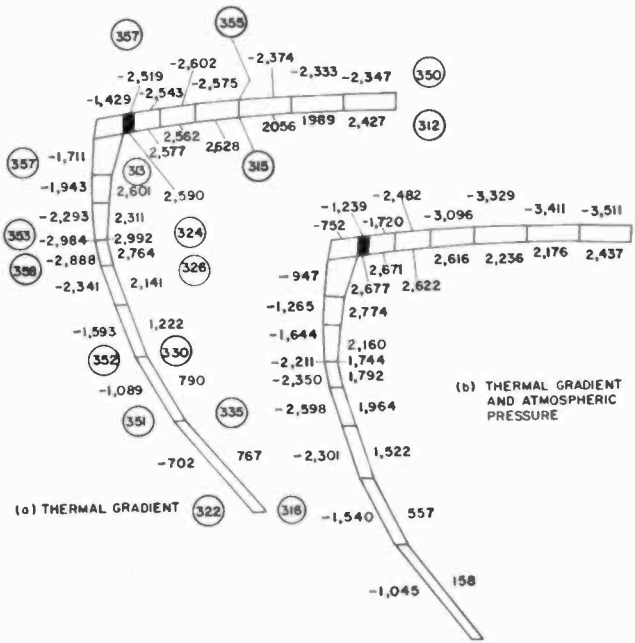

Fig. 28—Stresses induced (a) by thermal gradient and (b) by thermal gradient with atmospheric pressure. The thermocouple temperatures are circled. High tensile stresses exist along the inside surface of the tube for a higher outside than inside temperature distribution.

screen edge was about 7°C. The temperature differential between the inside and outside surfaces was about 44°C at the minor axis mold match, 30°C at the frit seal, and 6 to 20°C in the funnel.

The stress distributions resulting from the thermal gradient alone and in conjunction with the atmospheric pressure load are shown in Fig. 28. The temperature distribution as measured by thermocouples is shown by circled values. Here, a gradient of about 40°C exists between the outside and inside faces through the 0.485-inch-thick panel glass. Through the thinner sections of the funnel, the thermal gradient is much less. The tensile stresses on the vacuum side resulting from the thermal gradient are very high and range up to 2600 psi on the face and skirt and up to 2900 psi at the frit seal. The simultaneous application of atmospheric pressure reduces the tensile stresses in the frit seal by about 1200 psi (2922-1744 psi), which is good because the frit material can be weaker than the parent glass body.

In both (a) and (b) of Fig. 28, the entire outside surface including the screen edge is in compression. The outside surface is in compression principally because the outer surface is hotter and tries to expand. In so doing it puts the inside surface in tension. Fortunately, this high tensile stress is on the inside of the tube, removed from water vapor effects that can cause failure at lower stress levels by stress corrosion effects.

References

[1] R. W. Clough, "The Finite Element in Plane Stress Analysis," *Proc. 2nd A.S.C.E. Conf. on Electronic Computation*, Pittsburgh, Pa., Sept., 1960.

[2] O. C. Zienlewicz, *The Finite Element Method*, 3rd ed., McGraw-Hill, London (1977) pp. 549–554.

[3] W. Visser, "A Finite Element Method for the Determination of Nonstationary Temperature Distribution and Thermal Deformations," *Proc. Conf. on Matrix Methods in Structural Mechanics*, Air Force Inst. Tech. Wright-Patterson A.F. Base, Ohio, 1965.

[4] J. O'Connor and J. Wang, "Finite element modeling of hydrodynamic circulation," in *Numerical Methods in Fluid Mechanics*, eds. C. Brebbia and J. O'Connor, Pentech Press (1974).

[5] R. H. Gallagher, *Finite Element Analysis Fundamentals*, Prentice-Hall, Englewood Cliffs, NJ (1975).

[6] E. L. Wilson, R. L. Taylor, W. P. Doherty, and J. Ghaboussi, *Numerical and Computer Methods in Structural Mechanics*, eds. S. J. Fenves, N. Perrone, A. Robinson and W. C. Schnobrich, Academic Press, N.Y. (1973) pp. 43–57.

[7] The ANSYS finite element software program used for the analysis of static, dynamic and thermal engineering problems was developed by John Swanson of Swanson Analysis Systems, Houston, Pa.

[8] J. H. R. M. Elst and D. K. Wielenga, "The Finite-Element Method and ASKA Program Applied in Stress Calculations for Television Picture Tubes," *Philips Tech. Rev.*, **37**, 56–71 (1977).

[9] G. Eiwen, private communication.

[10] As determined using an HP-97 calculator and program ME1-07A.

[11] R. J. Roark and W. C. Young, *Formulas for Stress and Strain*, 5th Ed., McGraw-Hill, N.Y. (1975), p. 386.

[12] Ibid, p. 392.

[13] S. T. Gulati, private communication.

[14] R. Shahbender, private communication.

[15] R. E. Enstrom and D. A. Doanne, "A Finite Element Solution for Stress and Deflection in a Centrally Loaded Silicon Wafer," to be published in the *Proceedings of the Symposium on Characterization Techniques for Semiconductor Materials and Science*, The Electrochemical Society, Princeton, N.J. (1978).

[16] J. Hale, private communication.

Finite Element Analysis of a Twenty-Five Megawatt Power Tube and a High-Energy Water-Cooled Heat Sink for Fusion Research*

R. C. Bauder

RCA Solid State Division, Lancaster, Pa. 17604

Abstract—In this paper, the finite element method is used to calculate the thermal stress behavior of structures with up to 30 kW/cm^2 of surface energy bombardment. Analysis of structures by this method in the early design stage can be done at relatively low cost and offers a reduction in design and development times. Further, the method permits the analysis of structures with nonlinear properties, such as temperature-dependent thermal conductivity or radiation-induced swelling. In the paper, the method is applied (1) to a power tube anode capable of dissipating two megawatts of power and (2) to a beam dump for use in a Tokamac Fusion Test Reactor with a power density of thirty kW/cm^2.

I. Introduction

A twenty-five-megawatt power tube and an eight-megawatt beam dump, or heatsink, to be used in the Tokamak Fusion Test Reactor (TFTR), now under construction at the Princeton Plasma Physics Laboratory at Princeton, N.J., were designed with the aid of finite element analysis. This method of analysis is very useful in the solution of the transient and steady-state thermal and thermal-stress problems that arise in the handling of large energy densities, especially since any nonlinear material properties or convection coefficients involved can be expressed quite easily as a function of temperature or heat flow across a boundary.

* This work was supported in part by the University of California, Lawrence Livermore Laboratory, under Purchase Order No. 2660502, the Princeton Plasma Physics Laboratory under Contract E(11-1)-3073/269, and the RCA Corporation.

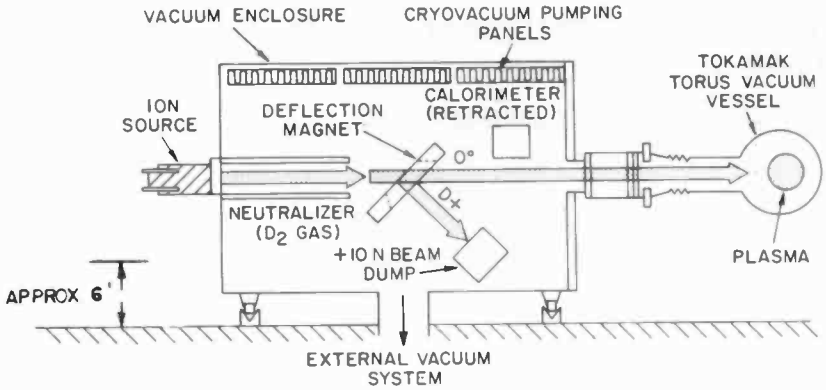

Fig. 1—Neutral-beam-injection system and it's relation to the Tokamak Torus.

The Tokamak Reactor, shown schematically in Fig. 1, is to be used in nuclear fusion experiments. Nuclear fusion, a reaction that makes use of a high-density isotope of hydrogen, is theoretically capable of generating an inexhaustible supply of energy. However, in order for a useful reaction to take place, the hydrogen (tritium) plasma must be ignited and maintained at a very high temperature (approximately 100 million °K) for several seconds. Present research schemes make use of a neutral beam of deuterium as the source of ignition.

The high-voltage grid of the power tube, the anode of which is water cooled, can accommodate two megawatts of plate dissipation while switching twenty-five megawatts. This tube switches the deuterium beam, which is initially in the ionized state. The ionized deuterium beam is then stripped of its charge in a neutralizer, which is approximately 40% effective. The stripped ions are used to ignite the plasma and the remaining ions are deflected to the water-cooled beam dump by means of a deflection magnet, as shown in Fig. 1. This beam dump, or heatsink, must be capable of absorbing 30 kW/cm^2 for a total of eight-megawatts in each of three sections (three neutral beams are necessary to ignite the plasma). The same beam-dump design is also employed in a retractable calorimeter used to measure the energy of the neutralized portion of the beam.

The switching power-tube anode must be capable of absorbing the normal 14 kW/cm^2 of electron-beam power, and the beam dumps must be capable of absorbing 20 to 30 kW/cm^2 of neutralized or ionized deuterium beam power. In both cases, the collecting surfaces have been set at an angle to reduce the incident beam power to a value below 3.0 kW/cm^2. Fig. 2 shows the preliminary design of a three-beam heatsink.

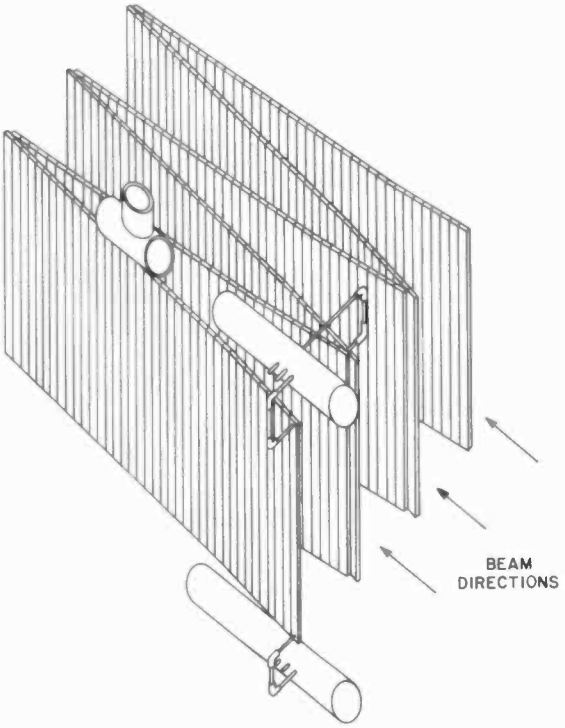

Fig. 2—Preliminary design of a three beam heat sink.

The anode of the power tube, located inside the cathode, consists of 72 identical sections, each with its own cooling channel. The cathode also consists of 72 sections, which are heater sections. These heater sections direct the electron beam radially inward toward the slots between the anode sections, as shown in Fig. 3; the coolant is distributed by a manifold at the end of each anode section.

Two basic approaches to power-tube section design were analyzed:

1. A thin-wall high thermal-conductivity design with a high coolant requirement.
2. A heat-storing energy-integrating design having a low coolant requirement.

The thin-wall device is essentially suited for dc use while the energy-integration device is pulse-length limited. The beam dump, like the power-tube anode, is pulse operated, and several alternative fin designs were also analyzed for it. Thermally-induced stresses had to be considered in both the power-tube anode and the beam dump as a design limitation. This paper describes the analyses, temperature profiles, and thermally-induced stresses for both structures.

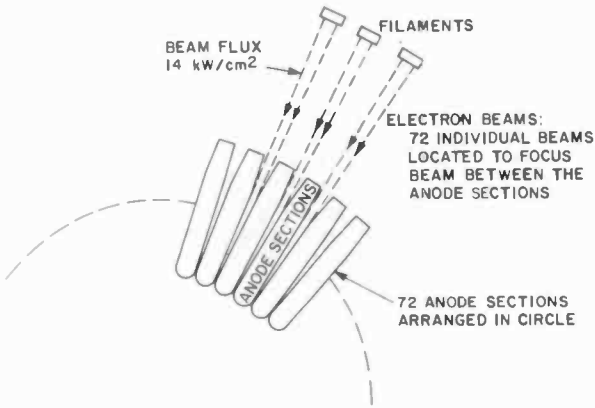

Fig. 3—Typical switch tube anode section.

2. Twenty-Five-Megawatt Power Tube Anode Analysis

There were two alternatives in the power-tube design:

1. A copper low-temperature fast-heat anode section with a low thermal inertia and low lag (Fig. 4a).
2. A high-temperature long-thermal-path high-thermal-inertia energy integrator having a lower coolant requirement (Fig. 5a).

Both alternatives require a large angle of incidence to distribute the beam flux because beam density is far too high for perpendicular impingement.

It was necessary to predict the following for each design:

1. The transient temperature profile of the surface and interior points.
2. The cyclic thermal stress necessary to predict fatigue failure for a pulsed device.
3. The transient heat flow across the coolant boundary. A coolant system can be specified to prevent a critical heat flux (CHF) burnout condition.
4. The effect of material and manufacturing tolerances. The models were built with and without a 0.02-inch beam-to-anode misalignment and with a variation of individual beam flux of 30% as a result of differences in heater–cathode spacing.

The large general-purpose finite element code ANSYS was used in the analysis because of the ease it provides in the handling of transient thermal and thermal stress problems, and because of its ability to express the material properties as a function of temperature and convection coefficients as a function of wall temperature. For the calculations, STIF

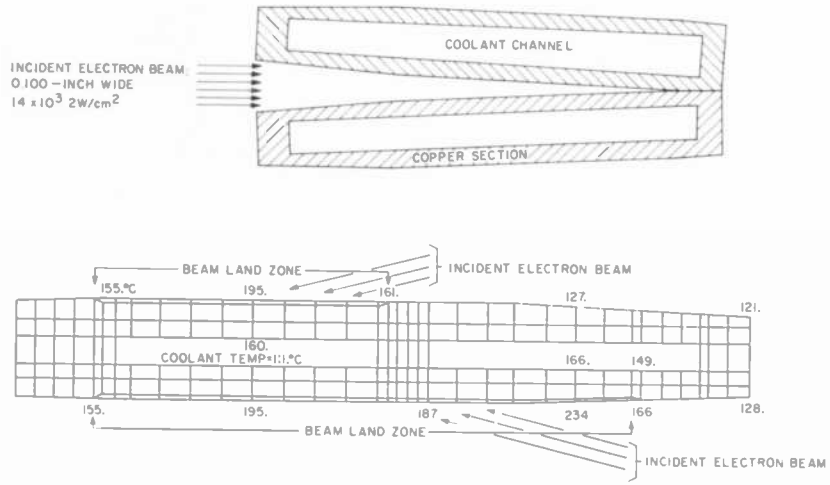

Fig. 4a—Power tube anode sections using a thin wall–high coolant flow concept.

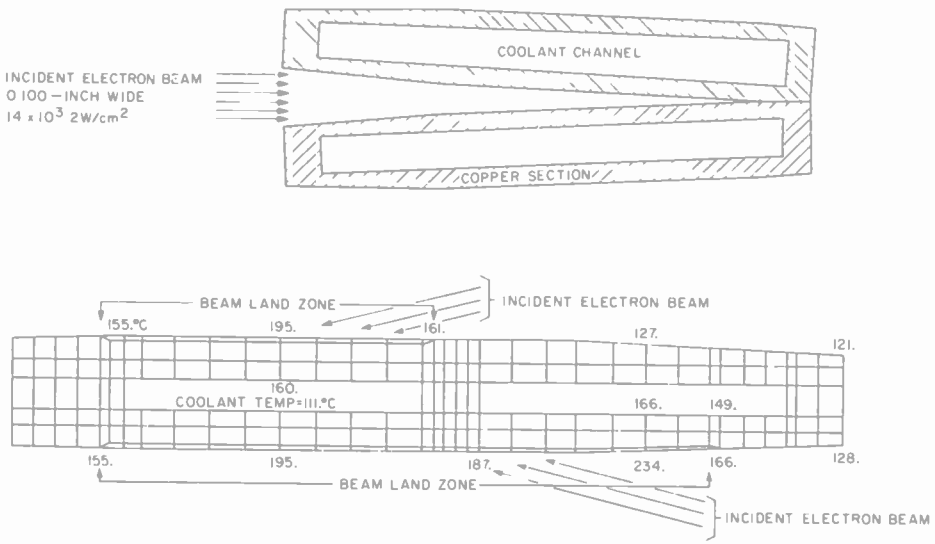

Fig. 4b—Finite element model of a thin wall copper anode section.

55, which is a quadrilateral nonlinear element having conduction and convection capabilities, was used.

The finite element models for two of the 72 identical sections of the two design alternatives are shown in larger scale in Figs. 4(b) and 5(b). Each line intersection is a node at which a transient temperature (one

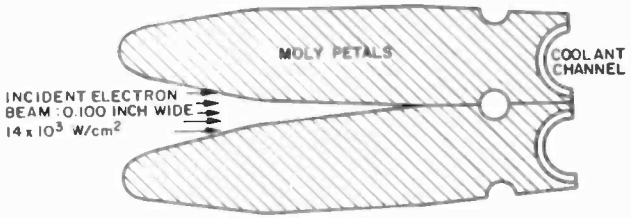

Fig. 5a—Heat integrator concept.

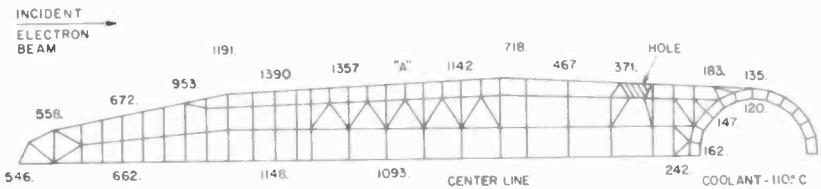

Fig. 5b—Finite element model of a molybdenum petal section (half symetry).

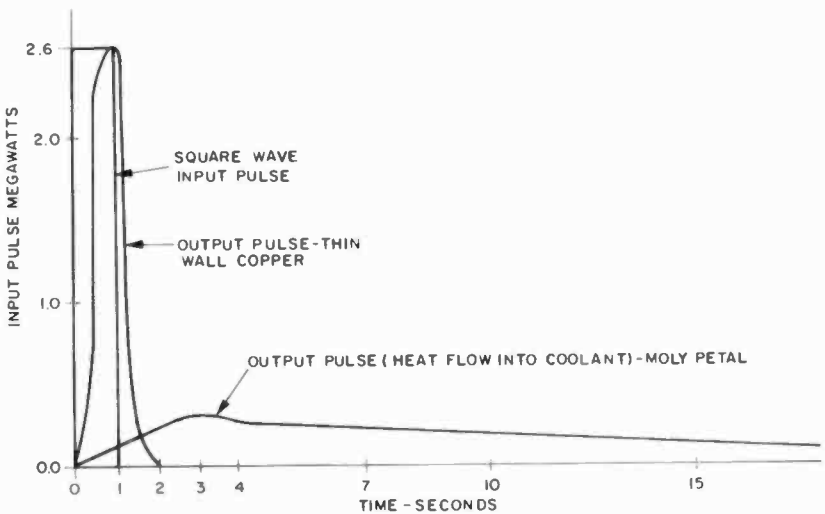

Fig. 6—Heat flow versus time curves for molybdenum petal and thin-wall copper anodes.

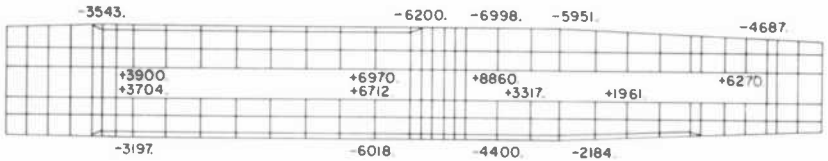

Fig. 7—Calculated thermal stress for the copper anode model shown in Fig. 4b.

for each time step) is obtained for each element. The values at selected nodes are shown and represent temperatures calculated from the heat input, material properties, and thermal coefficients using the ANSYS program and a finite-element model of the structure.

Results of the finite element analysis are shown in Figs. 6 through 8. The thin copper anode (Figs. 4(a) and (b)) reaches steady state in less than 0.4 second, as shown in Fig. 6, indicating that it is pulse-length independent, but nonetheless experiences cyclic thermal-induced stress. The energy-integration design (Fig. 5) is pulse-length dependent, but heat flow into the coolant is integrated over a longer time period, as also shown in Fig. 6. Peak heat flow occurs approximately two seconds after a pulse turn off (i.e., at three seconds in Fig. 6).

The thin-wall copper anode (Fig. 4) reaches a maximum temperature of 234°C. In contrast, the molybdenum petal anode of Fig. 5 is heated to a maximum temperature of 1390°C. These temperatures reflect the differences in thermal properties of the materials as well as the proximity of the coolant water to the incident electron beam.

The calculated thermally induced stresses are shown for the copper anode in Fig. 7 and for the molybdenum energy-integration anode in Fig. 8. The relatively low temperature gradient in the copper anode nonetheless results in tensile stresses at the water interface of up to 8860 psi, which is near the yield strength for oxygen-free, high-conductivity copper at room temperature.[1]

The stress results shown in Fig. 8 were measured at the end of the second pulse, and represent the maximum stress in the body of the petal. In the figure, the stresses range from 10,013 psi tensile at the mid-plane to 19,500 psi compressive at the incident beam surface. However, the

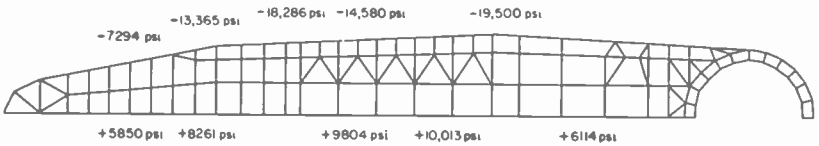

Fig. 8—Calculated surface stresses at time = 31.0 seconds for molybdenum petal.

strength of the molybdenum decreases significantly only above 800°C; at 1093°C the yield stress is 20,000 psi.[1] Peak stresses at the coolant boundary appear sometime later.

3. Beam-Dump Analysis

The beam-dump analysis can be separated into the following sub-analyses:

1. Analysis of models of individual fins to determine fin efficiency, with the convection film coefficient a function of temperature.
2. Analysis of models of test section used in a vacuum-diode test.
3. Analysis of models of a proposed heat dump to be used for heatsinking the neutral beam in the Tokamak Fusion Test Reactor.
4. Analysis of alternative designs incorporating tungsten-clad copper sections.

3.1 Fin Design

The goal in selecting an optimum fin configuration was to minimize local heat flux into the coolant to keep wall temperatures low and thereby reduce the likelihood of them reaching a critical heat flux with a resultant burnout. The point of union of the fin with the main structure is particularly vulnerable; the copper fins project into the coolant channel of the beam-dump section. The several different fin and plate sections considered for analysis are shown in Fig. 9. The reason for the selection of CDA alloy #360 (brass) for the laboratory test specimens was to match the electrical conductivities of the test specimens to the capabilities of the power supply in the joule heating-water cooling experiments.[2] The analysis was done using OFHC copper as the beam-dump material. Since the vacuum diode was a bombarded instead of a joule-heated section, it was made of copper.

The pivotal assumption used in these calculations is the effective convection film coefficient at the coolant/wall interface. The finite element method permits the use of unique material properties and film coefficients for each element, and thus predicts the idealized heat-exchange situation at each surface without consideration of communication with neighboring surfaces. In practice, however, there is direct communication between local surfaces. For example, bubbles streaming from the root area of the fins as a result of nucleate boiling will change the film coefficients of the surfaces along the sides of the fins.

The convection coefficients chosen are taken from work done on round tubes by T. Dormer, Jr. and A. E. Bergles[3] at the Massachusetts Institute of Technology. The particular curve choosen is for a 0.094-inch diameter

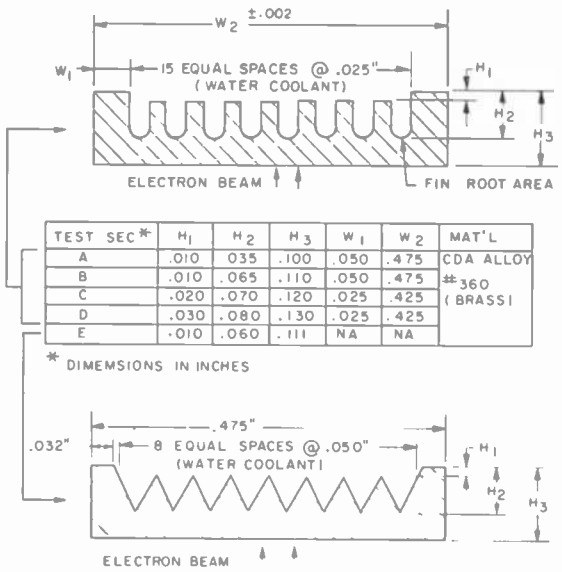

Fig. 9—Critical heat flux test section configurations.

round tube under the following conditions: P_{exit} = 30.0 psia, Velocity = 20 ft/s, and T_{in} = 29.0°C.

The curve from the report by Dormer and Bergles gives Q/A (*heat flux*) as a function of $(T_w - T_{sat})$, where T_w is the wall temperature and T_{sat} is saturation temperature. Further, since $h = (Q/A)/(T_w - T_{sat})$ (where h is the film coefficient), the fixing of T_{sat} at, for example, some

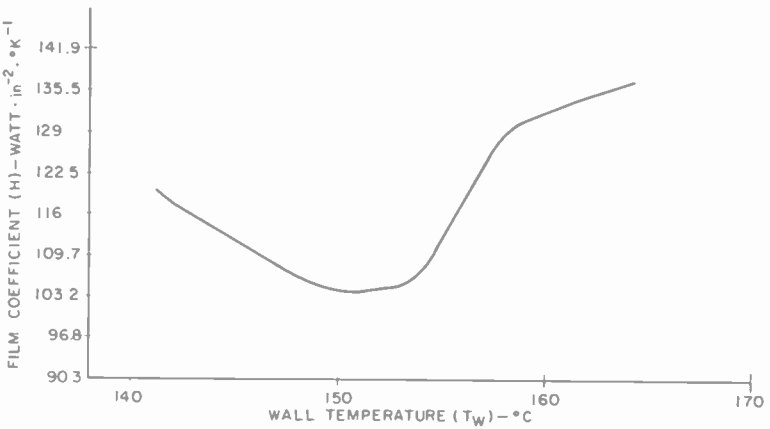

Fig. 10—Film coefficient (h) versus wall temperature (T_w).

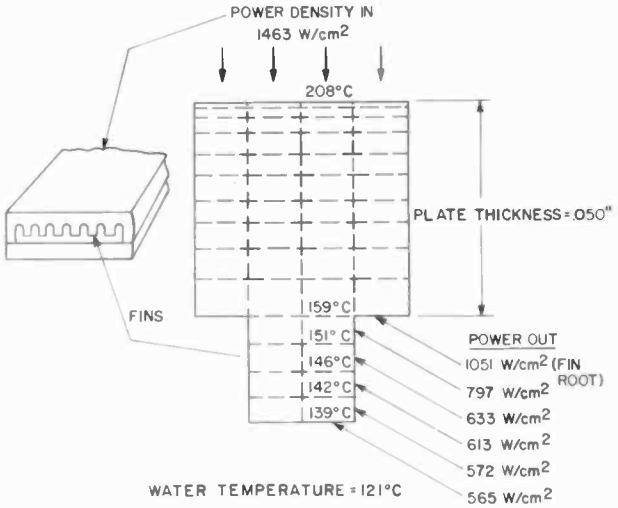

Fig. 11—Finite element temperature and heat flow results for a 0.050-inch thick copper section with a 0.025 × 0.025 inch square fin.

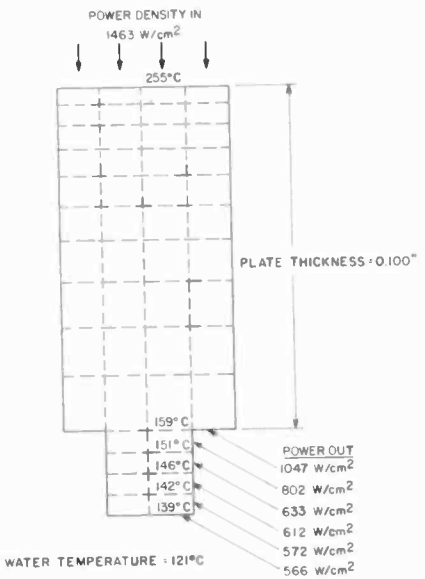

Fig. 12—Finite element temperature and heat flow results for a 0.10-inch thick copper section with a 0.025 × 0.025 inch square fin.

point near the coolant exit will make h a function of T_w. The ANSYS finite element code permits h to be expressed as a function of wall temperature. Fig. 10 is the curve of convection coefficient as a function of wall temperature used in the analysis.

Temperature and pressure conditions will vary along the length of a long, thin coolant channel. Lower pressure near the exit will result in a lower coolant saturation temperature (T_{sat}) which, in turn, results in different convection film coefficients and wall temperatures. The conditions selected for fin analysis represent those near the coolant exit, where failure is most likely to occur.

Transient thermal solutions were run on four fin and body-section types, as shown in Figs. 11 through 14. The solutions were allowed to run to steady state with an input heat flux of 1462 watts/cm^2. Steady state in all cases occurred in less than 0.4 second, meaning that a full thermal-stress cycle will be experienced for each neutral beam pulse.

Fig. 11 shows results obtained when a section of configuration A was bombarded with 1463 watts/cm^2 while the coolant was maintained at 121°C. Fig. 12 shows the results of an analysis of a section of configuration A with a double plate thickness on the bombarded side. The main

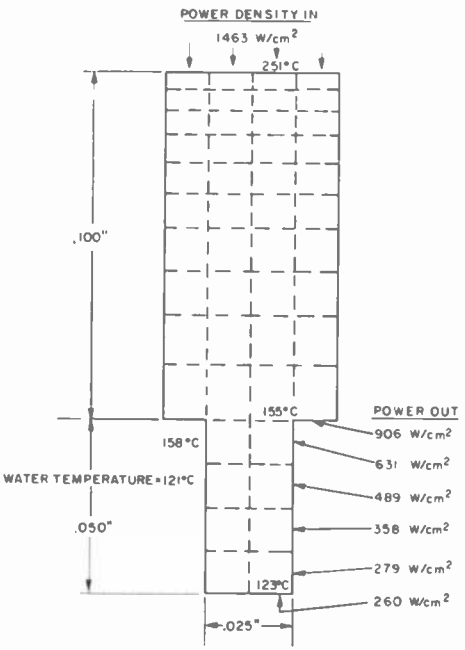

Fig. 13—Finite element temperature and heat flow results for a 0.10-inch thick copper section with a 0.050 × 0.025-inch fin.

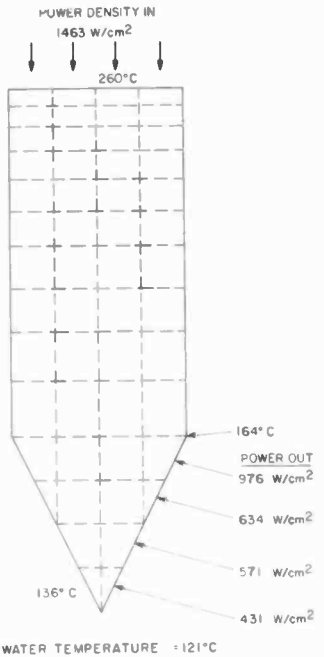

Fig. 14—Finite element temperature and heat flow results for a 0.050-inch wide by 0.050-inch high triangular fin.

difference between Figs. 11 and 12 is that the bombarded surface temperature in Fig. 12 increases to 225°C from the 208°C value obtained for the thinner plate with the same fin. Fig. 13 shows the results for a 0.100-inch-thick plate and 0.050-inch-long fin. This design results in a heat-flux density of 906 watts/cm^2 at the root of the fin, which is a significantly lower value than for the shorter fin shown in Fig. 12. The bombarded-wall temperature in both cases remains about the same.

Fig. 14 shows the results of an analysis of a plate with a triangular fin designed to provide a coolant channel with the same cross-sectional area as the equivalent C configuration shown in Fig. 13. If Fig. 13 is compared with Figs. 11, 12, and 14, it is apparent that configuration C presents the most attractive combination of low temperature for the bombarded wall and low heat flux in the root area of the fin (906 watts/cm^2 for configuration C versus 976 watts/cm^2 for the triangular design). A fin longer than 0.050-inch would provide marginal gains in exchange for a higher coolant-flow rate. For these reasons, combined with other laboratory results,[2] configuration C was chosen for the eight-channel seven-fin construction operated as the plate anode in the vacuum diode test.

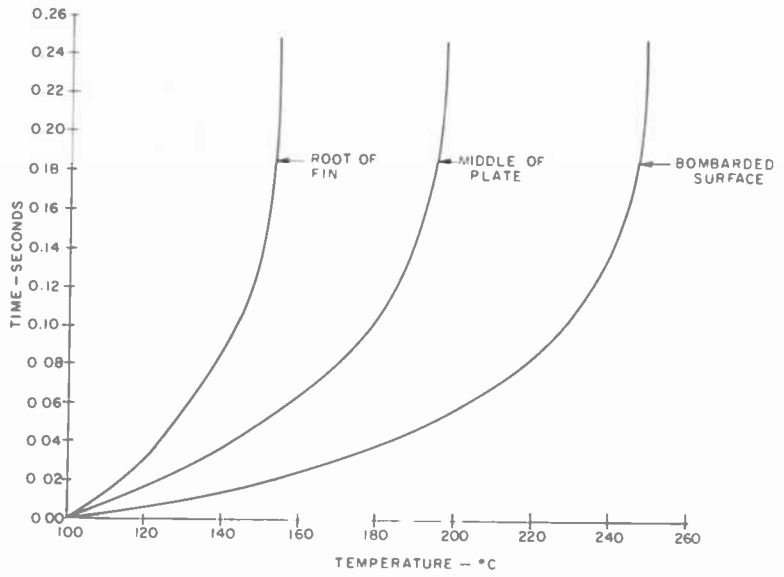

Fig. 15—Transient temperature curves for the section and fin configuration shown in Fig. 13 (a configuration type "C" fin).

Fig. 15 shows the transient temperature at several points in a plate of configuration C. Steady state occurs in approximately 0.3 seconds, indicating that this design is independent of pulse length or repetition rate for pulses longer than 0.3 second. The design is thus capable of operating as an eight megawatt dc heat pump.

3.2 Analysis of a Diode Test Section

Figs. 16, 17, and 18 show the finite element model, the isostress plot, and the displacement plot, respectively, for the 1-cm-wide by 30-cm-long test section that was attached to a stainless-steel backplate (not shown) and bombarded with a 2.0 kW/cm^2 electron beam while loaded with a maximum internal pressure of 435 psi. The analysis was run to study the stress situation at the supports (points A and B, Fig. 16) where the bombarded section is attached to the backplate.

Fig. 16 shows the temperature profile for the diode test section while the section was undergoing a 2.0 kW/cm^2 electron beam bombardment; the coolant temperature was 152°C. The temperature distribution from the bombarded surface through the fin and into the coolant is shown, the root temperature is 207°C, the tip temperature is 168°C. The measurements are similar for the other fins in the structure. Fig. 17 is a computer-plotted isostress diagram of the diode section showing that

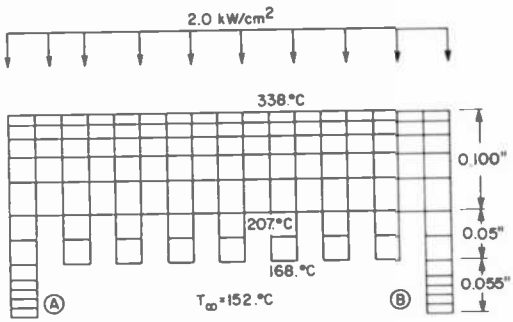

Fig. 16—Finite element model of a 0.100-inch thick by 1.0 cm wide copper beam dump section with configuration "C" fins.

the maximum principal stress of 5289 psi tension occurs in the support, the critical limiting part of the structure. Fig. 18 is a normalized displacement plot for these thermal conditions plus a 435 psi internal pressure load. The figure shows that the maximum displacement occurs in the center, directly between the supports, as expected. Based on these calculations, the supports were lengthened to provide sufficient strain isolation and thereby reduce the stress in this member.

3.3 Analysis of a Proposed Heat Dump

The finite element analysis discussed above, and the experiments, were used to propose a conceptual full-scale model of an eight-megawatt heat dump for the Tokamak Fusion Test Reactor.

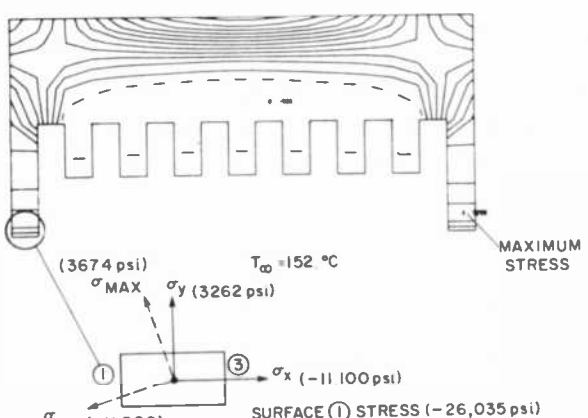

Fig. 17—Maximum principle stress isostress profile of the diode section with pressure and thermal loads.

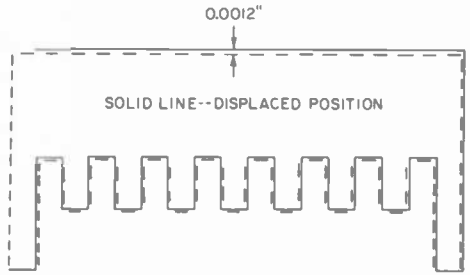

Fig. 18—Thermal displacement profile of the diode test section.

The ideal situation, of course, would be to build the heat dump from six large copper slabs brazed to stainless steel backplates with coolant channels between, as shown in Fig. 2. However, because the copper plate is heated on the outside, bombarded surface only, the assembly behaves as a bimetal strip with comparable thermal stress and deflection. Thermal stress and deflection would be huge for a one-piece assembly; therefore, the width of each section is determined by the allowable stress and out-of-plane deflection of each section. The sections are then assembled, venetian-blind style, as shown in Fig. 2, being careful to prevent edges of individual sections from receiving direct perpendicular bombardment.

It is important to note that the analysis data shown in Figs. 19 through 23 has not been substantiated by experiment. The decision to choose for analysis a section with three divisions, as shown in Fig. 19, was based upon simplified calculations and engineering judgment. Each of the three divisions contains seven fins and eight channels, as did the section of configuration C used in the vacuum diode test described above.

Fig. 19 shows the finite element model of the proposed section. All analysis on this section was done assuming a thermal load of 2.0 kW/cm^2 and an internal pressure load of 250 psi. Fig. 20 shows computer-plotted

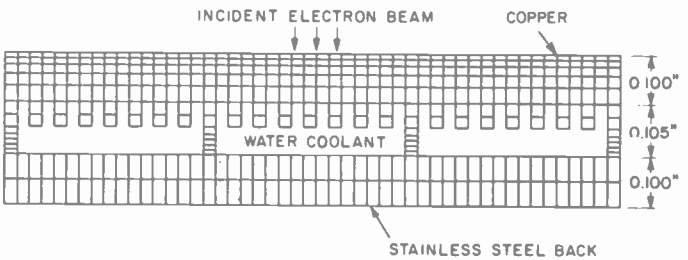

Fig. 19—Finite element model of a proposed beam dump with three sections and four supports.

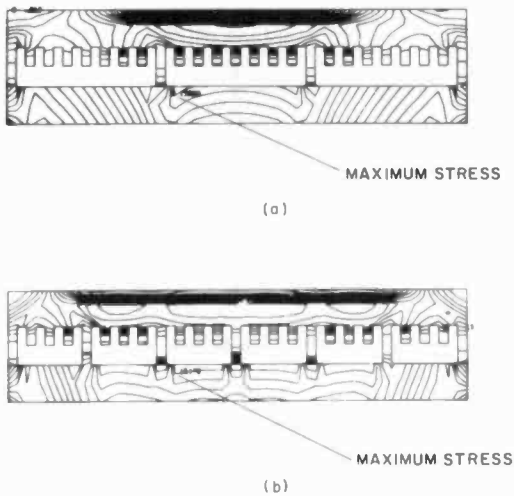

Fig. 20—Stress intensity isostress plots of two models of the proposed beam dump.

stress-intensity isostress plots of two variations of the structure, one with four supports to the stainless steel backplate, and one with seven supports. The maximum stresses occur near the attachment point of the post to the stainless steel plate; the detailed stress distribution is shown in Figs. 21 and 22.

Fig. 21, which is a magnified isostress plot of the four-support model,

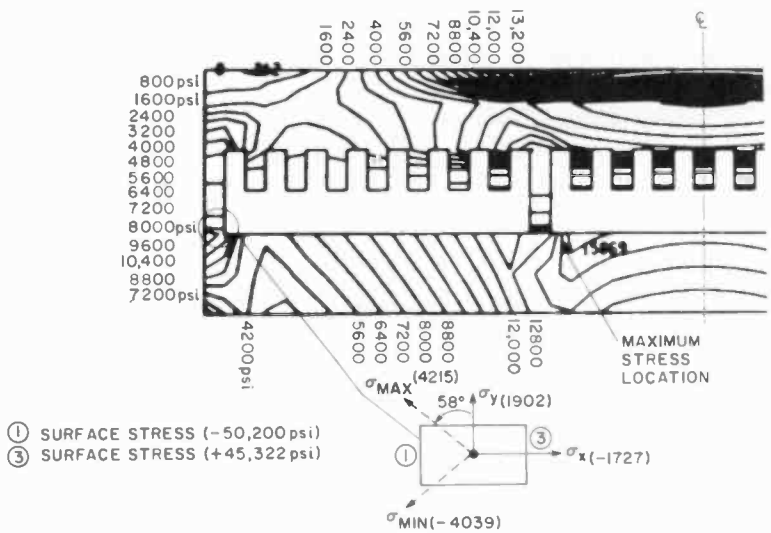

Fig. 21—A magnified isostress plot of model 1, Fig. 20.

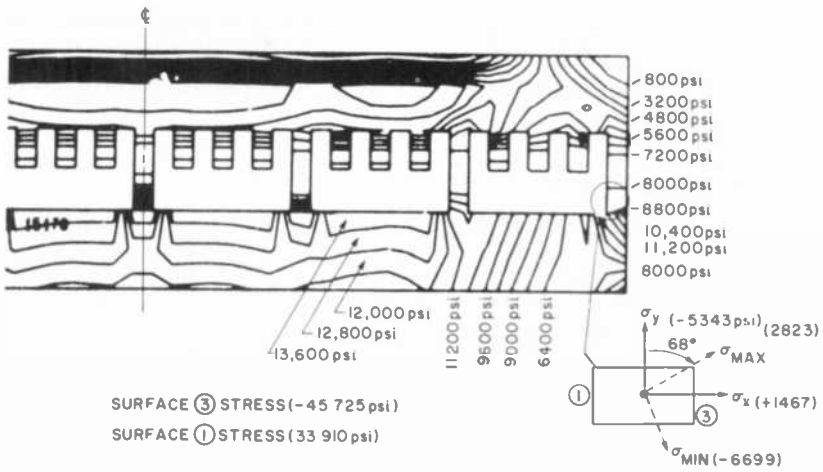

Fig. 22—A magnified isostress plot of model 2, Fig. 20.

shows that the maximum stress is 15,869 psi tension in the stainless steel. Fig. 22 is an identical plot of the seven-support model. An examination of both of these figures shows that the stress is highest where the supports attach to the steel backplate. There are methods for minimizing this stress, such as lengthening the supports, but this step would increase the coolant requirement. A solution to this could be to braze the supports into troughs milled into the backplate.

Fig. 23 shows relative displacement for the four-support model. It is

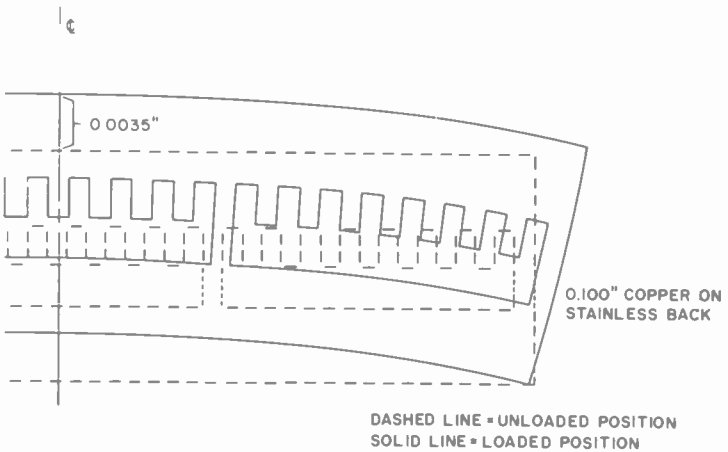

Fig. 23—Displacement plot of the proposed beam dump with 2.0 kW/cm^2 beam bombardment and 250 psi internal pressure (typical of conditions near the coolant entrance).

very important to know the magnitude of the out-of-plane displacement prior to building the full-size array so that the individual sections can be positioned to prevent shading or open cracks. Finally, before a full-size structure is built and tested, the alternative designs will receive a thorough finite-element analysis.

3.4 Analysis of a Tungsten-Clad Copper Design

As mentioned above, the limitation on the width of each section is determined by the allowable stress and out-of-plane deflection. The ideal material would have high thermal conductivity and negligible thermal expansion. Materials such as tungsten and molybdenum appear to present a favorable trade-off between coefficient of thermal expansion (one-fourth that of copper), thermal conductivity, and yield strength when compared with OFHC copper.

Copper is, by far, the most efficient fin material, but it has a low yield strength and a low melting temperature. Therefore, a tungsten-clad copper structure employing different combinations of material thickness was analyzed. The stress results for 0.02-inch of tungsten clad on 0.012-inch of copper are shown in Fig. 24. The results show a high sheer stress between the materials, which could lead to delamination. It should be pointed out that, at present, some power devices being manufactured make use of tungsten strips brazed to a copper plate for handling high electron-beam flux densities. Accordingly, this composite-materials approach would appear to be worth additional analyses.

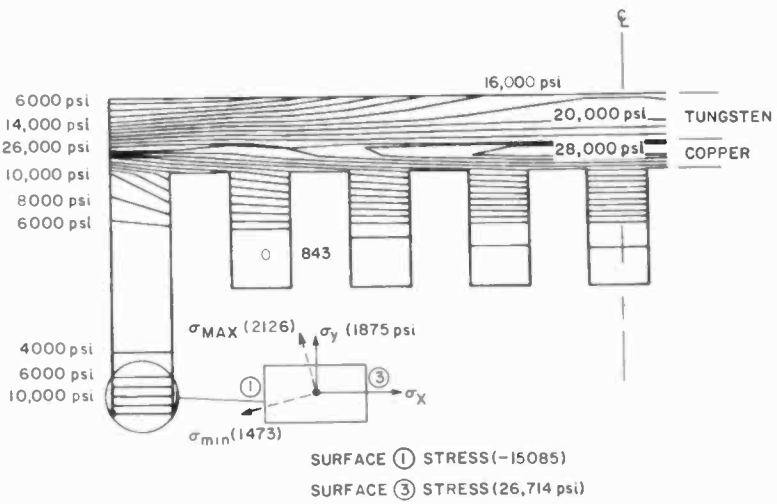

Fig. 24—Isostress plot of a tungsten-clad copper design.

CONCLUSIONS

(1) The finite element models provided a means for studying design alternatives on a theoretical basis prior to a commitment on materials and construction; the result was the elimination of some costly, time-consuming experiments. In addition, the models provided some guidance for the experiments which were run, and vice versa. The switch tube has been successfully built and tested.
(2) A conceptual design for the beam dump has been developed with enough analytical assurance to justify building a full-size structure.
(3) The possibility exists for using a combination of materials, such as a thin tungsten plate with copper-clad fins, in the coolant channel.

References:

[1] Materials Selector Guide 1978, Rheinhold Publishing Co., Stamford, Conn. Inc., pp 107.

[2] W. E. Harbaugh, R. C. Bauder, and W. A. Novajovsky, "Final Report, Water Cooled DC Heat Sink Development," Purchase order No. 266052 for University of California, Lawrence Livermore Laboratory, Livermore, Calif.

[3] T. Dormer, Jr., and A. E. Bergles, Report No. 8767-31, "Pressure Drop With Surface Boiling Using Small Diameter Tubes," Dept. of Mech. Eng., MIT.

[4] W. M. Rohsenow and J. P. Hartnett, *Handbook of Heat Transfer*, McGraw-Hill Book Co., (1973), pp. 13-34 to 13-38, and pp. 14-11 to 14-21.

[5] Industrial Research/Development, July 1978, p 48.

Patents Issued to RCA Inventors Third Quarter 1978

July

Z. M. Andrevski Flat Display Device with Beam Guide (4,101,802)
A. E. Bell, R. A. Bartolini, and A. Bloom Overcoat Structure for Optical VideoDisc (4,101,907)
S. Berkman and D. B. Irish Susceptor for Heating Semiconductor Substrates (4,099,041)
S. Berkman, G. W. Cullen, M. T. Duffy, and K. Kim Apparatus Improvements for Growing Single Crystalline Silicon Sheets (4,099,924)
B. W. Beyers, Jr. Timekeeping Apparatus with Power Line Dropout Provisions (4,099,372)
A. Bloom and H. Sorkin Method to Provide Homogeneous Liquid Crystal Cells Containing a Dyestuff (4,098,301)
T. L. Credelle Flat Display Device with Beam Guide (4,103,204)
T. L. Credelle Flat Display Device with Beam Guide (4,103,205)
G. Denes Memory Cells (4,103,185)
J. J. DiPiazza Nonreflecting Photoresist Process (4,102,683)
R. A. Dischert, A. J. Banks, and R. S. Hopkins, Jr. Television Synchronizing Apparatus (4,101,926)
J. G. Endriz, J. A. Rajchman, and J. A. Van Raalte Parallel Vane Structure for a Flat Display Device (4,099,085)
F. C. Farmer, Jr. Method and Apparatus for Measuring Cathode Emission Slump (4,101,823)
J. S. Fuhrer and E. O. Keizer Method for Forming a Narrowed-Electrode Pickup Stylus for VideoDisc Systems (4,098,030)
R. A. Gange Uniform Filament and Method of Making the Same (4,100,449)
P. E. Haferl Side Pincushion Distortion Correction Circuit (4,101,814)
S. Hagino Turntable Speed Control System (4,100,465)
W. E. Ham Method for Determining Whether Holes in Dielectric Layers are Opened (4,103,228)
J. M. Hammer and C. C. Neil Process for Forming an Optical Waveguide (4,100,313)
L. D. Huff Automatic Disc Wiping Apparatus (4,099,724)
H. Khajezadeh and S. C. Ahrens Monolithic Resistor for Compensating Beta of a Lateral Transistor (4,100,565)
M. A. Leedom VideoDisc Handling System for a VideoDisc Player (4,098,511)
A. L. Limberg Switchable Current Amplifier (4,103,246)
W. D. Masterton Shadow Mask Color Picture Tube Having a Mosaic Color Screen with Improved Tolerances (4,099,187)
A. Miller Optical Coupler (4,102,560)
G. I. Morton Complementary-Symmetry Amplifier (4,103,188)
S. A. Ochs Wafer Mounting Structure for Pickup Tube (4,103,203)
J. Ollendorf Protective Circuit for MOS Devices (4,100,561)
K. D. Peters Guided Beam Flat Display Device with Focusing Guide Assembly Mounting Means (4,099,087)
B. D. Rosenthal and A. G. Dingwall Quasi-Static Inverter Circuit (4,103,183)
W. Rosnowski Method of Fabricating a Semiconductor Device (4,099,997)
S. Shwartzman Method and Apparatus for Detecting Ultrasonic Energy (4,099,417)
J. L. Smith Eccentric Convergence Apparatus for In-Line Beam Cathode Ray Tubes (4,100,518)
J. L. Vossen, Jr., G. F. Nichols, and F. R. Nyman Adherence of Metal Films to Polymeric Materials (4,101,402)
C. F. Wheatley, Jr. Shunt Voltage Regulator (4,103,219)
D. H. Willis Horizontal Deflection Circuit with High Voltage Selection Capability (4,101,815)
J. P. Wittke Semiconductor Laser Having Fundamental Lateral Mode Selectivity (4,100,508)
O. M. Woodward Dual Channel Transmission of Microwave Power Through an Interface of Relative Rotation (4,103,262)

August

J. G. Amery and T. W. Burrus Noise Reduction Apparatus (4,110,784)
W. G. Anderson Quiescent Biasing of R-F Power Transistors for Other Than Class A Operation (4,105,944)
R. L. Baker, J. D. Partilla, C. M. Mahoski, and H. R. Ronan, Jr. Chuck for Use in the Testing of Semiconductor Wafers (4,104,589)

O. H. Bismarck Pulse Staggering Circuit (4,109,209)
A. Bloom and L. K. Hung Liquid Crystalline 4-Cyano-or 4-Nitrobenzylidene-4'-(N,N-Dialkylamino)-1-Aminoazabenzene Dyes (4,105,654)
R. R. Brooks GTO Ignition Circuit (4,109,632)
W. L. Cable, D. S. Binge, and R. F. Korosec Adjustment Device (4,108,407)
J. D. Callaghan Rotator with Remote Indicator and Self-Synchronization (4,109,191)
J. A. Castellano and M. T. McCaffrey Liquid Crystal Cell (4,108,793)
C. A. Catanese, J. G. Endriz, and S. A. Keneman Electron Multiplier with Switchable Beam Confinement Structure (4,109,178)
D. J. Channin Matrix Address System Using Erase Operation (4,109,242)
H. H. Chapman Electronic Mail Box (4,106,060)
C. A. Clark and K. C. Adam Clamping Circuit (4,109,166)
B. R. Clay and D. A. Gore Deflection-Type Modulator of Laser Beam for Communications (4,105,915)
L. S. Cosentino, J. G. Endriz, and G. F. Stockdale Electrical Connection Between Conductors on Spaced Plates (4,109,299)
A. T. Crowley Pulse Wave Phase and Frequency Detector (4,105,947)
A. G. Dingwall Voltage Controlled Oscillator (VCO) Employing Nested Oscillating Loops (4,105,950)
R. A. Dischert and J. M. Walter Clock Generator for Video Signal Processing (4,110,785)
C. A. Elliott and L. D. Huff Package Actuated Record Extracting Mechanism for a VideoDisc Player (4,109,919)
W. W. Evans Lockup Inhibiting Arrangement for a Phase Locked Loop Tuning System (4,110,693)
G. Forster and W. Bohringer Horizontal Deflection Circuit with Auxiliary Power Supply (4,104,569)
M. T. Gale and J. Kane Fabrication of Diffractive Subtractive Filter Embossing Master (4,108,660)
R. A. Geshner and J. Mitchell, Jr. Method for Removing Defects from Chromium and Chromium Oxide Photomasks (4,105,468)
R. H. Godfrey and A. M. Morrell Cathode-Ray Tube Having Apertured Mask (4,109,177)
A. M. Goodman MIS Readout Device with Dielectric Storage Medium (4,106,107)
N. F. Gubitose and R. A. James Machine for Straightening the Wire Leads of a Device (4,106,532)
W. J. Hannan Token and Reader for Vending Machines (4,108,367)
J. G. N. Henderson and W. M. Wine Phase Locked Loop Television Tuning System (4,106,059)
M. D. Holbrook and R. P. Fillmore Voltage Multiplier Circuit (4,106,086)
R. S. Hopkins, Jr., R. A. Dischert, and A. J. Banks Memory Read/Write Organization for a Television Signal Processor (4,109,276)
L. A. Jacobus, Jr. Method of Making an Insulated Gate Field Effect Transistor by Implanted Double Counterdoping (4,108,686)
E. A. James and P. Kuznetzoff Method of Depositing or Repairing a Patterned Metal Layer on a Substrate (4,107,351)
E. Jellinek System for Automatic Vehicle Location (4,107,689)
H. C. Johnson FM-CW Radar Ranging System (4,106,020)
G. S. Kaplan Digitally Processed Radar Speed Sensor (4,107,680)
G. S. Kaplan Clutter Free Communications Radar (4,109,247)
K. Katagi Polar to Rectangular Coordinate Converter (4,106,021)
E. O. Keizer Method for Forming Keel-Tipped Stylus for VideoDisc System (4,104,832)
H. Khajezadeh Integrated Circuit Protection Device Comprising Diode Having Large Contact Area in Shunt with Protected Bipolar Transistor (4,106,048)
C. M. Kudsia, L. A. Keyes, and H. J. Moody Traffic Switching in Communications Satellites (4,109,202)
A. J. Leidich Monostable Circuit (4,105,901)
A. W. Levine, G. Kaganowicz, and P. Datta Electro-Optic Devices (4,105,298)
N. F. Maxemchuk Digital Sampling Rate Conversion of Color TV Signal (4,106,053)
N. F. Maxemchuk Error Detection and Correction (4,110,735)
J. I. Pankove Amorphous Silicon-Amorphous Silicon Carbide Photovoltaic Device (4,109,271)
R. P. Parker Combined Blanking Level and Kinescope Bias Clamp for a Television Signal Processing System (4,110,787)
J. C. Peer and D. W. Luz Television Raster Width Regulation Circuit (4,104,567)
B. M. Pradal Audio Signal Processor (4,110,692)
C. F. Pulse Record (D248,753)
R. M. Rast Frequency Counter for Television Tuning System (4,109,283)
C. W. Reno and D. G. Herzog On-Axis Film Scanner with Reflected Illumination (4,105,926)
G. A. Riley Electronic Wristwatch (4,103,483)
J. J. Risko Method for Making Schottky Barrier Diodes (4,110,488)
A. Rosen and E. Mykietyn Electronically Tunable Microwave Frequency FET Discriminator (4,110,700)

R. C. Shambelan and C. W. Lindsley Machine for Chagging the Spacing of a Plurality of Wafers (4,108,323)
E. K. Sichel Electrochromic Cermet Material and Device Including the Same (4,110,259)
V. Stachejko Amplitude Balanced Diode Phase Shifter (4,105,959)
R. G. Stewart and S. S. Eaton, Jr. Sense Circuit Employing Complementary Field Effect Transistors (4,107,556)
H. J. Wolkstein Frequency Synthesizer with Rapidly Changeable Frequency (4,105,948)

September

A. A. Ahmed Switchable Current Amplifiers (4,117,417)
A. A. Ahmed Ground Fault Detecting Apparatus Including Current-Responsive Threshold Detection Circuitry (4,114,089)
D. E. Carlson and C. R. Wronski Amorphous Silicon Photovoltaic Device Having an Insulating Layer (4,117,506)
C. A. Catanese, J. B. Harrison, Jr., and N. L. Lindburg Electron Multiplier with High Energy Electron Filter (4,115,719)
J. J. Chinery Method of Testing Semiconductor Devices (4,114,096)
B. R. Clay and G. T. Burton Double Modulation Holographic Recording Technique (4,116,526)
W. R. Curtice Triggered Burst Generator (4,114,051)
R. V. D'Aiello Photovoltaic Device Having an Extended PN Junction (4,112,457)
R. J. D'Amato Process of Fabricating a Cathode Ray Tube (4,112,562)
W. Denhollander Transformer Arrangement for Synchronously Switched Vertical Deflection System (4,117,380)
R. DeStephanis Record Support and Alignment Apparatus for a VideoDisc Player (4,113,262)
J. G. Endriz Electron Beam Oscillation Compensation Method (4,115,724)
R. D. Faulkner Electron Discharge Tube Having a Cup-Shaped Secondary Electron Emissive Electrode (4,112,325)
R. D. Faulkner Non-Uniform Dynode Mesh for an Electron Discharge Tube (4,112,326)
E. R. Ganssle, R. J. Williams, and R. R. Scott Mounting Structure (4,116,263)
J. Goel, S. Y. Narayan, and I. Drukier Method of Making a Submicrometer Aperture in a Substrate (4,117,301)
G. B. Herzog Position Encoder Employing Charge Transfer Circuit (4,114,035)
R. Hollingsworth Unbalanced Sense Circuit (4,114,055)
M. V. Hoover Bridge Amplifiers Employing Complementary Transistors (4,117,415)
G. W. Hunka Optical Cursor Tracking Correction System (4,114,034)
M. A. Kalfus Circuit for Single-Line Control of GTO Controlled Rectifier Conduction (4,115,707)
M. A. Kalfus and H. W. Becke Switching Circuit (4,117,350)
M. A. Kalfus and D. M. Baugher Transistor Switching Circuit (4,117,351)
G. Katz Method of Assembling Components on Printed Circuit Boards (4,113,524)
J. D. Levine Device Having Thermionic Cathode Heated by Field-Emitted Electrons (4,115,720)
S. G. Liu Fast-Switching Pulse Modulator (4,115,708)
F. J. Marlowe and C. H. Anderson Modular Type Guided Beam Flat Display Device (4,117,368)
L. Muhlfelder and R. B. Hogen Magnetic Torquing System for Changing the Spin Rate of an Orbiting Satellite (4,114,841)
R. W. Nosker Smooth Groove Formation Method Employing Spin Coating of Negative Replica of Inscribed Disc (4,113,897)
G. H. Olsen, T. J. Zamerowski, and C. J. Bulocchi Vapor Phase Growth Technique of III–V Compounds Utilizing a Preheating Step (4,116,733)
M. Packer Organic Welding Flux Composition (4,115,157)
J. I. Pankove and M. A. Lampert Method of Passivating a Semiconductor Device by Treatment with Atomic Hydrogen (4,113,514)
J. I. Pankove and F. J. Marlowe Solid State Oscilliscope (4,114,095)
S. Ponczak and J. A. Olmstead Method of Forming a Curved Implanted Region in a Semiconductor Body (4,113,516)
O. H. Schade, Jr. Current Mirror Amplifiers with Programmable Current Gains (4,117,416)
J. L. Smith Static Convergence Device Including Magnetic Corrector Apparatus (4,117,433)
D. H. Willis Inrush Current Start-up Circuit for a Television Receiver Including a Start-up Decoupling Circuit (4,112,465)
D. H. Willis High Voltage Protection Circuit Having Predictable Firing Point (4,114,072)

AUTHORS

John R. Appert received his B.S. degree in Chemistry from the University of Scranton in 1957. From 1957 to 1960 he served in the U.S. Army as a member of a Nuclear Research Unit formed by the Surgeon General to study the effect of radio-active fallout on the European population. Upon discharge from the service, he worked from 1960 to 1963 at Republic Aviation Corp., Farmingdale, New York, on the electronic systems of the F-105 aircraft. He was responsible for the functional operation of flight line aircraft. Mr. Appert joined RCA Laboratories in 1964, working on the preparation and growth of vapor-deposited Nb_3Sn and its alloys. More recently, he has worked on the vapor phase synthesis and characterization of GaAs and GaAs-P alloys for high power rectifiers. Currently, he is working on the vapor growth of gallium arsenide, indium phosphide, and all combinations of the preceding group III–V compounds for many different device applications. In addition, he is also working on consumer products related to television.

Mr. Appert is a member of The Electrochemical Society.

Richard C. Bauder received the B.A. degree in physics from Muhlenberg College, Allentown, Pa. in 1961, and M.S. in Engineering Science from Penn State University in 1969. He has been with the RCA Solid State Division in Lancaster, Pa., since 1962. His first assignment with RCA was the design of microwave test equipment for small and medium power tubes, and photomultiplier tubes. From 1965 to 1968 he was involved in the implimentation of the automated phosphor dot screening of color picture tubes, and the recovery of the excess phosphor, including rare earth materials, from waste water. In 1968 he joined the environmental engineering group at Lancaster where he is responsible for the shock and vibration analysis of structures. Since 1972 he has been using finite element methods to study the thermomechanical behavior of a wide variety of RCA products. He has served as an associate instructor for RCA in the Continuing Engineering Education program in Technicians Mathematics, and Modern Physics.

Dan Botez received his B.S. degree with highest honors in Electrical Engineering from the University of California, Berkeley, in 1971 and his M.S. and PhD degrees in Electrical Engineering in 1972 and 1976, respectively, from the same University. As part of his graduate research, he designed, built, and successfully operated a liquid-phase-epitaxy system for the growth of AlGaAs lasers. His doctoral studies were concerned with the characteristics of layers deposited over preferentially etched channels in GaAs, as well as with novel devices made possible by this method. Following graduation, Dr. Botez continued his research in the semiconductor-laser field as a Postdoctoral Fellow at the IBM T. J. Watson Research Center, Yorktown Heights, N.Y. His work resulted in a novel type of mode-stabilized laser, the constricted double-heterostructure (CDH) laser. In 1977, Dr. Botez joined RCA Laboratories, Princeton, N.J., where he developed "thick-window" high-radiance surface-emitting LED's as well as highly stable single-mode cw lasers of the "double-dovetail" CDH type. He is currently involved in the study of LPE growth over channelled substrates and lateral mode stability in injection lasers. Dr. Botez is a member of Phi Beta Kappa.

Ronald E. Enstrom received the S.B., S.M., and Sc.D. degrees in metallurgy from the Massachusetts Institute of Technology, Cambridge, in 1957, 1962, and 1963, respectively. From 1957 to 1960 he worked at Union Carbide and Nuclear Metals, Inc., on materials for high-temperature oxidation resistance and nuclear fuel elements, respectively. At M.I.T., his doctoral thesis focused on the metallurgy and superconductivity of the three compounds in the Nb-Sn system, and at RCA Laboratories he was instrumental in making Nb_3Sn ribbon a practical high field magnet material. Later, he worked on the vapor phase synthesis and characterization of a large number of III-V compounds for high-power rectifier, microwave oscillator and amplifier, laser, LED, transistor, varactor, diode, and infrared-sensitive negative-electron-affinity photocathode applications. In addition to continuing III-V compound growth research, he has recently worked on the mechanical properties of silicon wafers and sapphire fibers, on the solution of stress distributions in new design kinescope tubes using finite element computer analysis methods, on glass technology, and on high conductivity polyacetylene. He received RCA Laboratories Achievement Awards in 1966 and 1972, and a David Sarnoff Outstanding Team Achievement Award in 1967. In 1969, he was appointed a Research Leader in the Semiconductor Materials Research Group. He spent the 1973–1974 academic year at the Eidgenossische Technische Hochschule, Zurich, Switzerland, on a European Study Fellowship.

Dr. Enstrom is a member of Sigma Xi, the American Institute of Mining, Metallurgical, and Petroleum Engineers, the American Physical Society, The Electrochemical Society, the American Association for Crystal Growth, and is a senior member of IEEE.

William E. Ham received the B.S. and M.E. (electrical engineering) degrees from the University of Oklahoma, at Norman, both in 1966, and the Ph.D. degree in electrical engineering from Southern Methodist University, Dallas, Texas, in 1970. Since graduation he has been a Member of the Technical Staff at RCA Laboratories. His primary work has been with electrical characterization and MOS device properties of heteroepitaxial semiconductors for integrated circuit applications. His research has involved the effective use of various types of vehicles, testing, and data presentation for the optimal understanding of integrated circuit processes. Specifically, this involves the study of electrical instabilities and dielectric properties, correlation of physical structure with electrical performance, and spatial distribution of device parameters. Current studies also include dimensional instabilities of wafers and photomasks and analysis of circuit yield distributions.

Dr. Ham is a member of the Electrochemical Society, Sigma Xi, Eta Kappa Nu, Sigma Tau, and Tau Beta Phi.

Chang Soo Kim received a BS degree in Nuclear Engineering from Seoul National University in Korea in 1963. He served two years of active duty in the Korean Army as an instructor in the Ordnance School. In 1968 he received an MS degree in Electrical Engineering from Carnegie Mellon University and, in 1971, a PhD in Electrical Engineering from the University of Florida, Gainesville, Florida. From 1971 to 1972 he was engaged in a Post Doctoral Research Program on Field Ion Microscopy/Atom Probe at Material Science Department of University of Florida. In 1973 he joined Harris Semiconductor, Melborne, Florida, where he was involved in ion-implantation technology in the development of a CMOS process on dielectrically isolated substrates. In 1974 he worked briefly on SOS process development at Inseleck, Princeton, NJ.

He joined RCA in 1975 as a Member of the Technical Staff, and has been involved with SOS process technology. The main area of his work has been on development of an SOS process for SSD commercial SOS products, improvements on SOS manufacturing yield and the area of modeling devices and processes, and on SOS memory diagnostic test technology.

Guido R. Niederoest received a B.Sc. degree in Mechanical Engineering in 1972 from Newark College of Engineering, recently renamed New Jersey Institute of Technology. He joined the engineering staff at RCA Astro Electronics in September 1972. He is presently attending the Rutgers University graduate studies program in mechanical and aerospace engineering for completion of a M.Sc. degree.

At RCA, Mr. Niederoest has worked on many aspects of spacecraft design, development and testing. His primary function involves mechanical analysis and testing of spacecraft structures and their subsystems, which requires a working knowledge of the numerical and finite element analysis techniques. He has applied this knowledge to many of the current communication and meterological spacecraft built at RCA. He was integrally involved in the qualification testing of the NASA funded TIROS N spacecraft and is presently working on the design of an advanced version of the same spacecraft. Other programs on which Mr. Niederoest has worked include studies of structural flexibilities and their effect on the dynamic characteristics of a spacecraft, the enhancement of the computer finite element technique, and the advancement of composite materials technology.

Theodore H. H. Pian, Professor of Aeronautics and Astronautics, holds the degree of S.B. in Aeronautical Engineering from the National Tsing Hua University in China, and the S.M. and Sc.D. in Aeronautical Engineering from the Massachusetts Institute of Technology. He has been project leader and supervisor in the Aeroelastic and Structures Research Laboratory at M.I.T. over a period of twenty-eight years. During this time he has worked in the fields of vibration and transient response of structures, aircraft loads, plasticity, viscoelasticity and creep, high stress fatigue of metals, structural damping of built-up structures, mechanics of fibrous composite materials, and finite element methods for linear and nonlinear structural mechanics and for fracture mechanics. Dr. Pian has served as consultant to aircraft and missile industries such as Lockheed Aircraft Company, Missile Systems Division, Boeing Aircraft Company, Aero/Space Division, and General Electric Company. During 1965–1966, Dr. Pian held an appointment of Visiting Associate in Aeronautics at the California Institute of Technology. He was a visiting professor at the University of Tokyo from September to December 1974, and a visiting professor at the Technical University, Berlin, from February to June 1975. He was a recipient of the Von Karman Memorial Prize for outstanding contribution to aerospace structural-material technology in the past decade in 1974 and of the AIAA Structures, Structural Dynamics, and Materials Award in 1975.

Dr. Pian is an associate fellow of the American Institute of Aeronautics and Astronautics and was a member of the AIAA Technical Committee on Structural Dynamics. He also holds membership in the Society for Engineering Education. He is a registered Professional Engineer in Massachusetts and an associate editor of the AIAA Journal.

Alvin W. Sheffler joined the Mechanical Engineering Staff at RCA Astro-Electronics in 1973. In 1975, he received the RCA Engineering Excellence Award for his contributions as lead engineer in the structural analysis of the RCA Satcom communications satellite. As Manager, Structural Analysis, he is responsible for the structural design, analysis, and testing of the current spacecraft systems, such as RCA Satcom and the DMSP and TIROS-N meteorological satellites. His work includes the analysis of the dynamic and acoustic stresses during launch and the on-orbit flexible body dynamics of large deployable solar arrays. In addition to these program design activities, he is involved in the development of advanced composite materials for spacecraft application. Prior to joining RCA, Dr. Sheffler was on the teaching staff in the Department of Aerospace Engineering at West Virginia University, where he received his Ph.D. He is a member of Sigma Gamma Tau and the AIAA Structures Technical Committee.

Robert S. Stepleman received the B.S. degree in physics and mathematics from the State University of New York at Stony Brook in 1964; and in 1969 he received a Ph.D. in mathematics from the University of Maryland. From 1969 to 1973, Dr. Stepleman taught and carried out research at the University of Virginia, Charlottesville, Va., in the Department of Applied Mathematics and Computer Science. Since August 1973, Dr. Stepleman has been a member of the technical staff of the RCA Laboratories, Princeton, NJ, where his work concerns mathematical analyses and applications.

He is a member of the American Mathematical Society, Association for Computing Machinery, Society for Industrial and Applied Mathematics, Special Interest Group in Numerical Mathematics, and International Association for Mathematics and Computers in Simulation.

D. B. Wolfe is a Staff Engineer in the Digital Communications Section of RCA Government Communications Systems, Camden, N.J. He joined RCA in 1952 after graduation from Tulane University with a B.S. degree in Mechanical Engineering. Since joining RCA he has had major responsibility in the mechanical design and development of military and commercial RF, TV, and digital telecommunications equipments. Mr. Wolfe is a lecturer in the RCA Continuing Engineering Education program where he developed the video tape lecture series on shock and vibration and on Mechanical Modeling. He is a member of the American Society of Mechanical Engineers.

RCA Review

A technical journal published quarterly by RCA Research and Engineering in cooperation with the subsidiaries and divisions of RCA.

Index Volume 39, 1978

March

June

September

December

Index to Authors, Volume 39, 1978